Mechanical Behavior and Microstructural Evolution in Metastable β Ti-Mo Based Alloys with TRIP and TWIP Effects

Jinyong Zhang

THESE DE DOCTORAT DE
L'UNIVERSITE PIERRE ET MARIE CURIE

Ecole doctorale de chimie-physique et chimie analytique de paris-centre
Spécialité : science de matériaux

Présentée par

M. JINYONG ZHANG

Pour obtenir le grade de

DOCTEUR de l'UNIVERSITÉ PIERRE ET MARIE CURIE

Mechanical behavior and microstructural evolution in metastable β Ti-Mo based alloys with TRIP and TWIP effects

Soutenue le 22 septembre 2014

Devant le jury composé de :

M. Yannick Champion	Rapporteur
M. Eric Fleury	Rapporteur
M. Thierry Gloriant	Examinateur
M. Philippe Vermaut	Examinateur
M. Fan Sun	Encadrant
M. Frédéric Prima	Directeur de thèse
M. Yvon Millet	Invité

Table of contents

List of Figures

Figure **page**

List of Tables

Table page

General introduction

Titanium and its alloys have been extensively used in numerous application fields in the last ten years, due to their unique feature of properties such as high strength, low density, excellent biocompatibility and good corrosion resistance. However, both their low ductility (total elongation typically less than 0.20) and their lack of work-hardening when compared with steels or Co-Cr alloys, limit their use in advanced applications where superior combinations of strength and ductility are required. As a consequence, it is necessary to develop new Ti-alloys with combination of high strength, large ductility and a high work-hardening rate. Therefore, inspired from the superior mechanical properties of TRIP/TWIP steels (TRIP for Transformation Induced Plasticity and TWIP for Twinning Induced Plasticity), we proposed a new type of metastable β Ti-alloys showing combined TRIP/TWIP effects. This alloy was designed based on the "d-electron alloy design method" and controlling of electron/atom ratio (e/a).

The preliminary experimental results show that the so-designed alloy at as-quenched state displays high strength, large plasticity and an improved work-hardening rate thanks to simultaneous TRIP and TWIP effects. In order to further investigate the relation between the β stability and TRIP/TWIP effects, two strategies were applied on the binary model alloy. One is thermal-treatment, i.e. Low temperature aging (LTA), which is carried out on the binary model alloy to manipulate β/ω phase transformation. The objective of this strategy is to control the ω phase transformation without excessive modification of β matrix chemical composition, keeping the possibility for combined TRIP and TWIP effects to occur. The other is chemical composition modification, i.e. alloying development of ternary compositions by adding third alloying elements into the binary model alloy, which is proposed to shift the alloying position along the model alloy design route. The objective is to enlarge the titanium TRIP/TWIP family of alloys to ternary metastable

β Ti-alloys. Two sets of ternary alloys were designed. The first one is Ti-9Mo-6W (wt. %) alloy, in which the $\overline{Bo}$ and $\overline{Md}$ of this alloy located in the line with the same stability of designed binary alloy. The second one is Ti-12Mo-xZr (x=1, 3, 5) (wt. %) alloys to investigate the influence of the neutral element Zr on mechanical and microstructural behavior. The mechanical behavior and microstructural evolution were investigated for these ternary alloys.

This dissertation is organized into six chapters.

Chapter 1 provides a general introduction of physical metallurgy of metastable β Ti-alloys. At the beginning of this chapter, alloying elements were classified based on their influence on the β transus temperature (T_β) and martensite start temperature (Ms) in metastable β Ti-alloys. With respect to influence for the β transus (T_β), alloying elements are usually classified into neutral, α-stabilizers, or β-stabilizers. However, the influence of alloying elements on martensite start temperature (Ms) is still of conflict, due to so-called α-stabilizers or neutral elements decreased the martensite start temperature (Ms) and worked as the β-stabilizing elements. Then, an overview is given about different phases and their transformation in metastable β Ti-alloys. There are many phases and phase transformation involved. These phase can be classified into equilibrium phase (α and β phase) and non-equilibrium (i.e. ω) depending on whether enough time has been allowed to reach steady state condition. The corresponding phase transformation, such as β->α, β->ω, ω->α and β->α" (stress-induced martensite), will occur during the thermo-mechanical treatment. Finally, the deformation mechanism occurred in metastable β Ti-alloys, e.g. dislocation slip, mechanical twinning and stress-induced phase transformation, are provided. The activation of such deformation mechanisms completely depends on the stability of the β phase.

In **Chapter 2**, we firstly introduce several alloy design strategies often used in designing the titanium alloys, such as "trial-and-error" method, the empiric Mo

equivalent and the semi-empiric “d-electron alloy design method”. Especially, the “d-electron alloy design method” was in detail given (called the $\overline{\mathrm{Bo}}$–$\overline{\mathrm{Md}}$ map). Based on the $\overline{\mathrm{Bo}}$–$\overline{\mathrm{Md}}$ map, a binary model alloy was designed to be Ti-12Mo (wt. %). The model of binary Ti-12Mo alloy shows high strength, large ductility and high work-hardening rate due to combined TRIP and TWIP effects.In order to further enlarge the titanium TRIP/TWIP family of alloys to ternary metastable β Ti-alloys, the third alloying elements were added into the Ti-12Mo alloy based on the design route of Ti-12Mo alloy. Thus, the ternary Ti-Mo based alloys (Ti-9Mo-6W and Ti-12Mo-xZr (X=1, 3, 5)) were designed, and the designed procedure was also introduced in detail in this chapter.

In **Chapter 3**, we introduce experimental techniques and analytical software used for elaboration, manufacturing, heat-treatment and characterization of the designed alloys. The alloys were melted by vacuum arc melting furnace. Then, the ingots were homogenized at 900°C for 24h under high vacuum of 10^{-6} Pa using our laboratory self-designed device, followed by water quenching. Subsequently, the as-quenched ingots were cold-rolled into sheets with the thickness of 0.5mm. Taking from the sheets, tensile samples were prepared and heat-treated based on different heat-treatment strategies. Finally, several characterized tools, such as conventional X-ray diffraction (XRD), In-situ Synchrotron X-ray diffraction (SXRD), electron backscatter diffraction (EBSD), electrical resistivity measurements (ERM), transmission electron microscopy (TEM) and Automatic crystal orientation measurements (ACOM) TEM, were carried out to investigate the deformation mechanisms, phase transformation and microstructure evolution sequence.

The **Chapter 4** described the mechanical behavior and microstructural evolution of the binary model Ti-12Mo alloy. The tensile experimental results display that the model alloy exhibits excellent mechanical performances: high strength (~1000MPa), large uniform ductility (ε=0.38) and a significant work-hardening effect close to the

theoretical limit. The uniform plastic deformation was separated into three stage based on the evolution of the work-hardening rate. In the early deformation stage, primary strain/stress induced phase transformations (β->ω and β->α'') and primary mechanical twinning ({332}<113> and {112}<111>) are simultaneously activated. Secondary martensitic phase transformation and secondary mechanical twinning are then triggered in the twinned β zones. At the end of the uniform plastic deformation, a complex deformation microstructure was observed, showing highly disturbed matrix induced by a high volume fraction of twins and occurrence of multiples secondary mechanisms. The evolution of the deformation microstructure results in a high work-hardening rate (~2GPa) bringing about high tensile strength (~1GPa) and large uniform elongation (> 0.38).

In **Chapter 5**, Low temperature aging (LTA) treatments were performed on the model Ti-12Mo alloy and the influence of on mechanical performance and microstructure was studied. The aim is to improve the mechanical property by controlling the activation of various deformation mechanisms, i.e. stress-induced phase transformations and mechanical twinning. A set of short-time LTA treatments were applied at 110°C, 160°C, 260°C and 310 °C for 60 and 600s, respectively. At LTA < Tωiso, mechanical performances can be largely enhanced from solution-treated (ST) state. A superior combination of high strength (close to 1200MPa of true stress) and a stable plasticity of ε=0.4 (true strain) was achieved with a significant work-hardening effect. At LTA > Tωiso, the work-hardening effect and uniform plasticity are gradually ceased with increasing of tensile strength. The investigation of deformation mechanisms revealed the key role of deformation induced ω precipitation played in the activation of different deformation modes. Due to the precipitation of isothermal phases induced by LTA, the progressive inhibition of deformation induced ω led to important variations of tensile behaviors.

Chapter 6 presented the mechanical and microstructural behaviors of the ternary Ti-Mo based alloys. The chapter also discussed the effect of the third alloying

element (W or Zr) on the TRIP and TWIP effects. There were two objectives of adding third alloying elements into the model Ti-12Mo: (1) to validate the possibility of theoretical prediction from “d--electron design method” in the ternary composition about practical alloying developments and performance optimization; (2) to investigate the relationships between stress-induced phase transformations and mechanical twinning in the new ternary system.

Finally this work ends with conclusion of the relationship between alloying design method and deformation mechanism, where microstructural evolution in Ti-12Mo alloy, the influence of LTA treatments on evolution of deformation modes and effects of third alloying elements in mechanical and microstructural behaviors are discussed in detail.

Chapter 1

Metallurgical and physical background of metastable β titanium alloys

1.1 Introduction

Titanium and its alloys have been more and more used in numerous application fields in recent several decades. Generally, Ti-alloys are classified into three main categories: α, α+β and β alloys, depending on their composition, thermo-mechanical processing and their final microstructure **[1, 2]**. The change of the Ti-alloys type depending on the β-stabilizer content is shown schematically in Figure 1.1. At the beginning, the β-stabilizer content is negative (α-Stabilizers), only α phase structure occurs. And with β-stabilizer content increasing, an (α + β) structure develops. Then the metastable β phase structure occurs when adding higher β-stabilizer content, located between βc and βs. Here, βc is the minimum critical level of β stabilizer for metastable β alloys to retain β completely upon quenching from β phase field, and βs is the minimum amount of β stabilizer for stable β alloys. The metastable β phase is still within the two-phase region, although it can quench to retain 100% β phase in such alloys. The metastable β-type alloys will precipitate a second phase (usually α phase) upon aging. Finally, only stable β-phase presents when above βs. The metastable β-type Ti-alloys and stable β-type Ti-alloys, both are included in the β-type Ti-alloys **[3]**.

Compared with α+β alloys, β alloys seem be the most versatile class of Ti-alloys due to their increased heat treatability, wide and unique range of strength-to-weight

ratios, deep hardening potential, and improved ductility **[1, 4]**. In addition, they also possess superior fatigue resistance as compared to α+β alloys **[1, 4]**. As shown in Figure 1.1, β-type alloy is defined as a titanium alloy with sufficient β-stabilizer content to suppress the martensitic transformation when quenching to room temperature. This means that 100% β phase is retained. Since the 1950's, the development and application of the β-type alloys has been described in the literature **[1, 5]**. Recently, these alloys can be found in aerospace, sporting goods, automotive, orthopedic implant, and oil well systems **[1, 3, 4]**. For example, Ti-10-2-3, Beta C, Ti-15-3, TIMETAL 21S, and BT22 **[6]** are used for structural components; Ti17 is used for gas turbine engine compressor discs **[6]**; and "Gum metal" alloy is used in implant materials **[7]**.

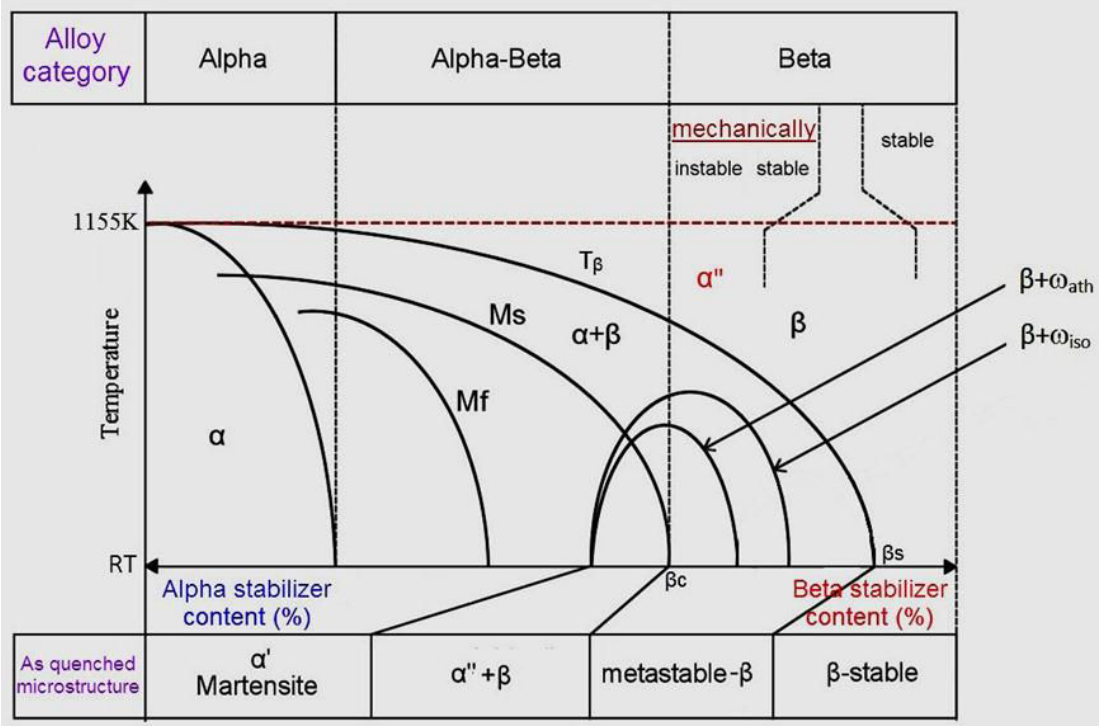

Figure 1.1 Pseudo-binary phase diagram of Ti-alloys with the decomposition products of the β-phase. Here, βc is the critical minimum β stabilizer amount for near β or metastable β alloys to retain β completely on quenching from β phase field and βs is the minimum amount of β stabilizer for stable β alloys; T_β, RT, Ms and Mf refer to the β-transus temperature, room temperature, martensite start and finish temperatures, respectively.

In the β-type alloys, compared to the stable β Ti-alloys, the metastable β

Ti-alloys seem to attract more interest because of their superior properties such as the superelasticity, shape memory effects, low Young's modulus and better formability **[8-10]**. The mechanical properties of metastable β Ti-alloys depend strongly on the presence of several phases (e.g., ω phase and martensitic α" phase) in them. The appearance of these phases could be controlled by either the optimized alloy design **[7, 8]** or the materials processing **[11]**. The phases presented in the alloy are related to the alloying elements and the thermal history of the alloy. Moreover, the activation of deformation modes, such as dislocation slip, mechanical twinning and stress induced martensitic transformation (SIM), depend on the β phase stability **[8]**. Therefore, it is necessary to make a general introduction about the physical metallurgy of the metastable β Ti-alloys before designing new metastable β Ti-alloys showing large ductility and high work-hardening rate.

1.2 The alloying elements and the phases in metastable β Ti-alloys

1.2.1 Alloying elements

As seen in the Figure 1.1, metastable β Ti-alloys lie in the area between βc and βs. In the region, two key parameters are referred: the β transus temperature (T_β) and martensite start temperature (Ms). The T_β is used in determining the Ti-alloys type. The Ms is used to manipulate the deformation behavior of metastable β Ti-alloys. Both of the two parameters are closely related with β-stabilizer content. In these alloys, the controlling of the β-phase stability by alloying elements is crucial to control the activation of deformation mechanisms at room temperature.

Alloying elements have their own attributes in effecting the two parameters. With respect to influence on the β transus (T_β), alloying elements are usually classified into neutral, α-stabilizers, or β-stabilizers. Alloying elements like Al, Ga, B,

Sc, La, Ce, Ge, C, O and N raise the β-transus temperature and hence are called as α stabilizers **[1, 2, 12]**. The element Al is the most commonly used α stabilizer. On the contrary, alloying additions of V, Mo, Nb, Hf, Ta, Mn, Cr, Cu, Ni, Fe, Co, Au, Ag, W, Pt and Pd can lower the β transus temperature and cause a stabilization of phase at lower temperatures, thus are regarded as β stabilizers **[1, 2, 12]**. However, the influential capacity on the T_β is various for different β-stabilizer elements. Generally, an empirical expression, called Mo equivalent, is used to get a quantitative value for the β phase stabilization effect of individual elements **[1]**. The molybdenum equivalent (Mo_{eq}) can be expressed by the following equation **[13]**:

$[Mo]_{eq} = Mo + Nb/3.6 + Ta/4.5 + W/2.27 + Cr/0.63 + Mn/0.65 + V/1.5 + Fe/0.35 + Ni/0.8+Co/0.7-Al$

In addition to the above α and β stabilizers, there exist some elements (i.e. Zr, Hf and Sn) considered as neutral elements since they have (nearly) no influence on the α/β phase boundary **[1]**. These neutral elements can completely dissolve in the α and β phases of titanium.

However, regarding the influence of alloying elements on the martensite start temperature (Ms), some controversies still remain in scientific researches. It has been recognized that the Ms Temperature decreases monotonically with increasing content of the β-stabilizing elements in the metastable β Ti-alloys. For example, Kim et al. **[14]** reported a linear relationship between Ms and Nb content for Ti-Nb binary alloys (Ms decrease by 40 K per 1 at% for Nb element). As for the so-called α-stabilizing elements or neutral elements (i.e., O, Al, Zr and Sn), the elements in beta solid solution have been shown to decrease the martensitic start temperature (Ms) and retard ω phase formation **[15]**. It has very recently been suggested that O enhances the shuffle associated with the martensite transformation, while suppressing the Bain distortion **[20]**. For example, the M_s temperature in a Ti–Nb system decreases by the Al addition **[16]**. Also, the addition of Sn to Ti–V **[17**], Ti–Cr

[18], Ti–Nb **[17]**, and Ti–Ta **[19]** alloys and the addition of O or Zr to Ti–Nb alloys **[10, 20]** give a similar effect for martensite start temperature (Ms). In this sense, O, Al Zr and Sn are no longer the α-stabilizing elements, but work as the β-stabilizing elements in these metastable β-type Ti-alloys. However, oxygen is still an α-stabilizing element in the aged condition, since the amount of the α-phase precipitated during aging increases with the oxygen content in the alloy **[21]**.

Recently, based on the combination of the two parameters (T_β and Ms), our groups and co-workers **[22]** proposed a coefficient of ΔT (T_β-Ms) that can be promoted to evaluate the β phase stability in the metastable β Ti-alloys. We have proved the availability of the ΔT via equiatomic substitution of Nb by Zr in Ti-Nb-Zr alloys system. The results **[23]** show that the more for the coefficient ΔT, the better for superelasticity in Ti-Nb-Zr alloys.

1.2.2 Phases in Metastable β titanium alloys

Metastable β Ti-alloys possessed excellent mechanical properties completely depend on their final microstructure. In the metastable β region, there are several phases and phase transformation involved. These phases can be classified into β, α, α″ and ω (athermal ω, isothermal ω and deformation induced ω). The corresponding phase transformation, such as β->α, β->ω, ω->α and β->α″ (stress-induced martensitic transformation), will occur during the thermo-mechanical treatment. The phase transformation of β->α, β->ω, ω->α will be introduced in section 1.3. And the phase transformation β->α″ (stress-induced martensite transformation) upon deformation will be described in section 1.4.

1.2.2.1 The β and α phase

Similar with α+β alloys, the structures of α and β phase in the β alloys are HCP and BCC structure, respectively. The β phase is stable at high temperature and can be

retained during quenching from above β transus temperature (T_β) to room temperature (RT). The space group of β phase is $Im\bar{3}m$ with two atoms at (0, 0, 0) and (1/2, 1/2, 1/2) coordinates **[1, 2]**. The atomic unit cell of β phase is schematically shown in Figure 1.2(a). The lattice parameter: a=b=c=0.332nm, α=β=γ=π/2, and the most close-pack planes and directions are {110}β and <111>β, respectively.

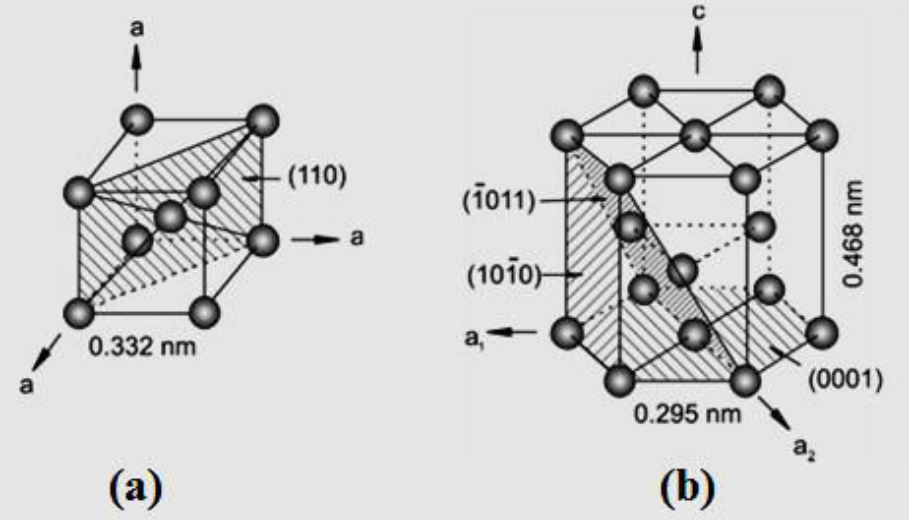

Figure 1.2 The schematic diagram of crystal structure of bcc β and hcp α phase, their lattice parameters and most densely packed planes and directions are also illustrated [1].

The α phase can be precipitated when the alloys are quenched at low cooling rate from temperature above β transus or upon aging at the α precipitation temperature range. Two types of α phase has been reported **[3, 24]**. One obeys the Burger's orientation relation (called Burger's α or type Ⅰ α); the other does not obey that relation, but is instead oriented in a complex and incompletely understood manner (called non-Burger's α, or type Ⅱ α) **[3, 24]**.

The Burger's α (hereafter called α phase) crystallizes at room temperatures in a modified ideally hexagonal close packed structure (HCP). The space group of α phase is $P6_3/mmc$ with two atoms per unit cell at (0, 0, 0) and (1/3, 2/3, 1/2) positions. The hexagonal unit cell of α phase is also shown in Figure 1.2(b). The lattice parameters at the room temperature: a=b=0.295 nm c=0.468 nm, and α=β=π/2,γ=2π/3. The c/a

ratio is about 1.587, smaller than the ideal ratio of 1.633 for the hexagonal close-packed crystal structure. As indicated in Figure 1.2(b), there are three most densely packed types of lattice planes. One is the {0001} plane, also called basal plane; another one is the $\{\bar{1}010\}$ planes, also called prismatic planes; and the last one is the $\{10\bar{1}1\}$ planes, also called pyramidal planes. The three a1, a2, and a3 axes are the close-packed directions with the indices <1120 >.

1.2.2.2 The martensite phase (α″)

Martensitic transformations are diffusionless, shear (displacive) solid state structural transformations. The transformation is most commonly driven by mechanical deformation or by a change in temperature **[25].** Thus, the martensite phase can be classified into athermal martensite phase and stress-induced martensite phase α″ (SIM) based on their formation condition. As for athermal martensite phase, their transformations from β phase were close related to the martensite start temperature (Ms) depending on the β stability **[25]**. The athermal α″ transformation is hard to occur in the metastable β Ti-alloys due to the martensite start temperature (Ms) far lower than room temperature. However, the SIM α″ often occurs in the metastable β Ti-alloys upon deformation, bringing about such peculiar properties as superelasticity and shape memory effects. Thus, the SIM α″ phase often was investigated in the metastable β Ti-alloys. The detailed information about SIM α″ transformation was listed in in section 1.4.

The SIM α″ phase has an orthorhombic structure with the same structure of athermal α″ **[14]**. The additional shuffling of atoms in alternate (110)β planes results in a C-centred orthorhombic crystal structure with a Cmcm space group **[26]**. The atoms located at (0, 0, 0) (1/2, 1/2, 0), (0, 1-2y, 1/2) and (1/2, 1/2-2y, 1/2) positions, for example, the value of y≈0.2 in Ti-Nb alloys **[27]**. Thus, α" may be viewed as a

transitional phase between the α hexagonal structure and the β BCC structure. Indeed, altering the values of b/a, c/a and y, all three structures, α, α" and β, will be produced alternative.

1.2.2.3 The ω phase

The metastable ω phase is the important feature of metastable β alloys. The formation of the ω phase can affect mechanical properties of β phase Ti-alloys [28]. Several overviews **[28-30]** about ω phase have been reported. Here, the structure, classification and morphology of the ω phase are briefly introduced.

The occurrence of the ω phase was first reported in 1954 by Frost et al. **[31]** on Ti-Cr alloys. Since then, the metastable ω phase has been found in the other Group IV transition metals (such as zirconium and hafnium). The ω structure has been determined to be either hexagonal (belonging to the space group (P6/mmm)) or trigonal (belonging to the space group (P3m1)) depending on the extent of transformation. Upon the complete transformation, the ω phase has a hexagonal symmetry, while the incomplete transformation, the structure is a trigonal system. Both structures contain 3-atoms/unit cell and can be derived from the parent bcc structure by simple atom movement. The equivalent positions are: 0,0,0; 2/3,1/3,1/2; 1/3,2/3,1/2 for ideal hexagonal, and 0,0,0; 2/3,1/3,1/2+z; 1/3,2/3,1/2−z(0<z<0.167) for rumpled structure. Here, when z=0, ω structure is an idea structure with hexagonal symmetry, and when z=1/6, ω structure is a cubic symmetry.

The size of ω phase is very small in metastable β Ti-alloys. It is reported that its size varied from less than 6nm in the as-quenched condition to about 300nm just before its transformation to α **[29, 32]**. Thus, the transmission electron microscope (TEM) technique was often applied to observe its size, morphology and distribution. The β-ω phase mixture exhibits special diffraction patterns, which enable it to be

easily identified. In general, the ω phase can be identified from the superlattice diffraction spots excited at various 1/3<112>β and 1/3<112>β positions on the <011>β and <113>β zone patterns of β phase as illustrated in Figure 1.3.

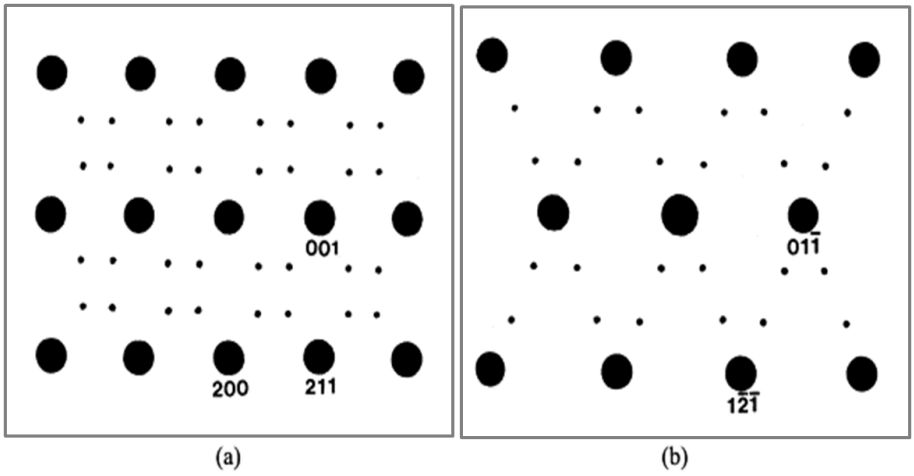

Figure 1.3 The schematic diagram of ω phase diffraction spot on the (a) <110>β and (b) <113>β zone.

Generally, the ω phase in the β matrix can be classified into three types based on their formation condition, i.e. athermal ω phase (ω_{ath}), isothermal ω phase (ω_{iso}) and deformation induced ω phase upon strain.

Athermal ω: usually precipitates during water quenching from the high temperature β range. When the β-stabilizer content is over a limited range of solute content that is close to the lower limit for the retention of β phase, a metastable phase called athermal ω phase occurs from β phase. The ω_{ath} precipitation is a diffusionless transformation. The formation rate of ω_{ath} phase is too extremely rapid to be suppressed. Bagaryatskiy and Nosova et al. **[33]** showed that in a Ti-6(wt. %) Cr alloy the ω_{ath} formation was not suppressed even at cooling rates as high as 11000 °C/sec.

Isothermal ω: generally precipitates during aging at a temperature below about 773K **[30]**, controlled by combination of displacive and diffusion process **[34, 35]**. When the alloys are at higher alloying content, the isothermal ω phase forms during

aging in a temperature range of 100 to 500°C. The nature of this isothermal ω phase depends on the holding time and the quenching rate. More precisely, the volume fraction of isothermal ω increases with increasing holding time and decreasing quenching rate until phase precipitation reaches to saturation. It is now recognized that isothermal ω phase is a continuation of the athermal ω transformation **[34, 35]**.

Deformation-induced ω: forms in the β-stabilized alloys upon shock loading. Some studies **[36-40]** have showed that the deformation-induced ω phase has been found in metastable Ti-alloys upon deformation at room temperature. Banerjee et al. **[28]** proposed that the deformation-induced ω phase is almost same to the athermal ω phase. They thought that the formation condition of deformation-induced ω phase in the shock loading experiment is equivalent to the athermal treatment, because the duration of the shock loading is typically of the order of a few μs, diffusive atom movement is negligible.

The morphology of three types of ω phase displays different microstructural profiles. The athermal ω size is very smaller and its distribution is random and indefinite. The morphology of athermal ω phase is usually fine particles **[23]**. A typical TEM image of ω_{ath} phase is shown in Figure 1.4a. However, Ping et al. **[42]** found that the athermal ω phase is plate-shape in a Ti–30Nb–3Pd (wt.%) shape memory alloy during quenching (Figure 1.4b). Compared with athermal ω particles, the isothermal ω precipitation could be distinguished by its slightly larger size and a composition gradient along the ω/β interface. Usually, the size of isothermal ω phase are in the range of 10-20nm. The morphology of isothermal ω phase can either be cuboidal or ellipsoidal in Ti-Transition metal alloys **[43, 44]** in term of the lattice misfits (Figure 1.4c and d). As described in some overviews **[28-30]**, the high misfit binary alloys of Ti-V, Ti-Cr, Ti-Mn, and Ti-Fe are reported to have a cuboidal morphology. However, the low misfit binary alloys of Ti-Mo and Ti-Nb are reported to form precipitates with ellipsoidal morphology **[43, 44]**. Regarding the deformation

induced ω phase, it generally displays plate-like morphology **[40]** (Figure 1.4e and f).

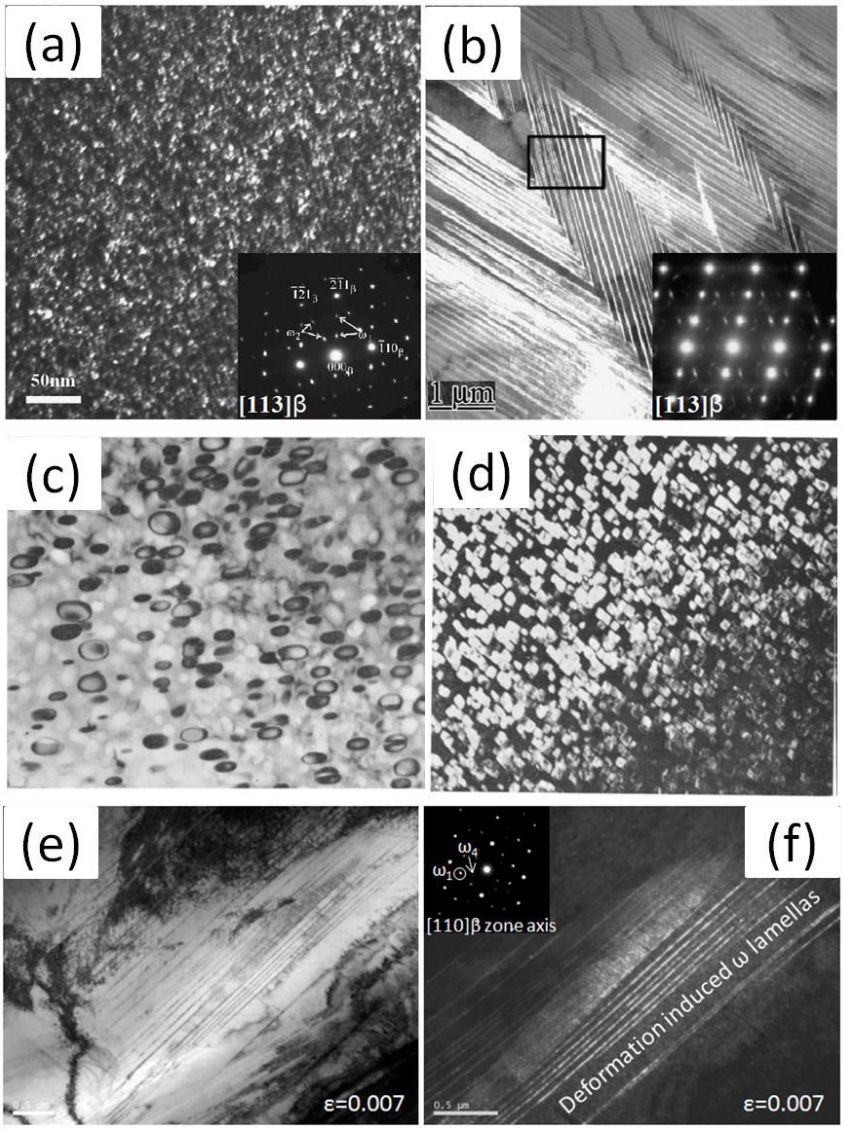

Figure 1.4 The typical TEM micrographs and corresponding diffraction patterns of three types ω phase. (a) very fine nano-size ω particles in the water-quenched Ti-Mo alloys; (b) Plate-shaped ω in the water-quenched Ti–30Nb–3Pd alloy; (c) ellipsoidal ω particles in Ti-Mo alloys; (d) cuboidal ω particles in Ti-V alloys; (e) and (f) the plate-like deformation induced ω phase in the Ti-12Mo alloy upon strain [40].

1.3 Phase transformation in metastable β Ti-alloys

1.3.1 β to ω transformation

The formation of ω_{ath} precipitates was recognized as a diffusionless, pure

displacive, collapse of the {111} planes of the β phase via a shuffle mechanism. On the other hand, the formation of ω_{iso} precipitates have been postulated via a thermally-activated process involving diffusion-based compositional partitioning followed by the collapse of {111} bcc planes in the regions depleted in β destabilizing elements. Therefore, from the viewpoint of instabilities in the β phase, the ω_{ath} results from a pure structural instability while the ω_{iso} results from concurrent compositional and structural instabilities.

Recently, It is generally accepted that the transformation mechanism is the (111) collapse model, which was developed by Fontaine et al. **[45-49]** to explain the dependency of temperature and composition on the diffuse ω reflection and reversible athermal formation **[29]**. The model can be viewed as a collapse of (111) lattice planes of the bcc structure in a sequence shown in Figure 1.5. This orientation relationship can be clearly visualized to observe in the schematics diagram of β to ω phase transformation (Figure 1.5a-d) and be defined as (0001)ω // (111)β; <11-20>ω //<110>β. The three-layer stacking sequence (0, 1, 2 . . .) of {111} planes changes to the two layer stacking sequence of the ω structure when the planes are collapsed in the middle (marked as 1.5) keeping the 0 and 3 planes undisplaced (Figure 1.5c and d). On completion of the collapse, the ω phase has a hexagonal symmetry and the transformation would transform the ABCABC stacking of (111) β lattice planes to an AB'AB' packing in the final β structure **[34]** (Figure 1.5e). Therefore a_ω can be defined as $\sqrt{2}$ a_β and c_ω $\sqrt{3}/2$ is a_β. Four variants of ω can be formed along four nonequivalent <111> directions in the β matrix. However, the collapse is not always complete, which may result in a “rumpled” plane after collapsing and a trigonal system was developed along <111> β direction (Figure 1.5e). Such a periodic displacement of the {111} β-type planes can be proposed to be the result of a longitudinal displacement wave propagating along the <111> β direction. The longitudinal displacement wave can be described as a sinusoidal wave with

wavelength, $\lambda=3d_{222}$, and a corresponding wave vector, K_ω, equal to 2/3<111>* (where <111>* is a vector in the reciprocal space) (Figure 1.5f). The advantage of this description lies in the fact that it can be applied to partial collapse situations also by varying the amplitude of the displacement wave, the amplitude being directly related to the order parameter.

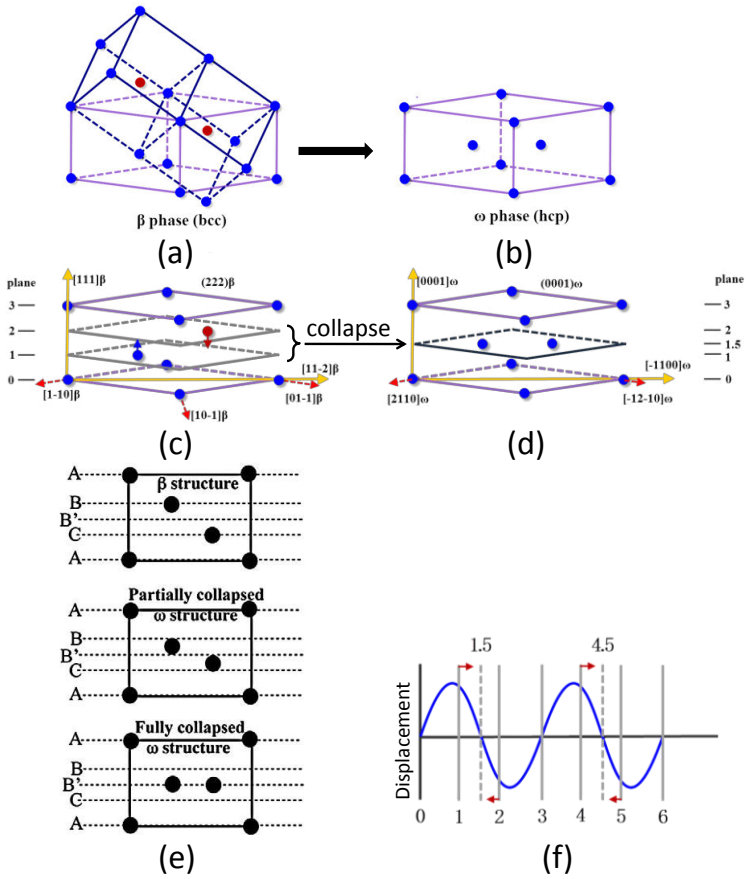

Figure 1.5 (a) and (b) the three-dimension schematic diagram of lattice of β and ω phase, respectively; (c) Planar arrangement of the {222}β atomic planes in the bcc lattice. The 0, 1, 2, . . . sequences of atomic plane arrangements can be seen. (d) The planar arrangement of the (0001)ω atomic planes in the ω lattice. As can be seen the ω-lattice can be obtained from the bcc lattice by collapsing a pair of planes (1 and 2) to the middle (marked as 1.5) while keeping the third one (0 and 3) undisturbed. (e) the schematic figures for the ideal motifs of β, partially collapsed ω and fully collapsed ω structures. The ABCABC stacking of 222 planes in the β and AB'AB' stacking in the collapsed ω structures are highlighted. Completely collapsed {222} planes form a six-fold symmetry, whereas an incomplete collapse forms a three-fold symmetry along the <111> axis. (f) The displacement of {222} planes can also be visualized in terms of a sinusoidal displacement wave where upward movement is seen as a positive displacement and downward as negative displacement.

1.3.2 ω to α transformation

The isothermal ω phase is regarding as one of the potent nucleation sites for α phase. Actually, it has been proved that the isothermal ω structure is a metastable intermediate step in the transformation process from β to α phase. Blackburn et al. **[50]** pointed that the growth dependency of α depends on ω morphology and β/ω phase misfit, via investigating the phase transformation in Ti-Mo and Ti-V alloy. High misfit system such as Ti-V and Ti-Fe tend to have cuboidal ω morphology while low misfits systems like Ti-Mo have ellipsoidal ω **[32, 44, 50]**. In the different misfit system, two thoughts have been developed over years about the mechanism of α nucleation and growth from ω phase. One thought that α nucleates inside the ω particles and consumes the latter during its growth; the other thought that α nucleates coherently at the ω/β interface with an orientation relationship with both ω and β phases. In the high misfit system, the α phase was shown to nucleate at ledges of dislocation which develop at the ω/β interface **[44, 51]**. On the contrary, there has been considerable controversy regarding the nucleation of α for low misfit systems. Azimdazeh et al. **[52]** proposed that α nucleated at some distance from the ω/β interface in Ti-6.8Mo-4.5Fe-1.5Al (LCB) alloy (a low misfit system). However, Prima et al. **[53]** justified that the α phase formed in the core of a ω particle in LCB alloy. Some authors also suggested that the actual nucleation and growth pattern of α depended on ω phase when they investigated the phase transformation on Ti-Mo **[54]**, and Ti-Nb **[55]** alloys.

Recently both thoughts were clarified by using high resolution transmission electron microscopy (HRTEM) imaging. For example, Prima et al. **[53]** showed the nucleation of an α particle in the core of ω phase was followed by dissolution of ω on coarsening of the nucleated α (Figure 1.6a and b). Meanwhile, they also proposed a model (Figure 1.7) that displacive transformation of ω core to α postulate the

mechanism of nucleation of α from ω. In the model, the α/β/ω orientation relationship can be expressed as: (0001) ω // (−12−10) α // (−111) β, (-1-120) ω // (0001)α // (0-11)β and [1-100] ω//[10−10] α // [211] β **[53]**. However, the direct evidence of laths α phase nucleation at an ω/β interface and grow with consuming the ω particles proposed by Ohmori et al. **[56]** is illustrated in Figure 1.6c.

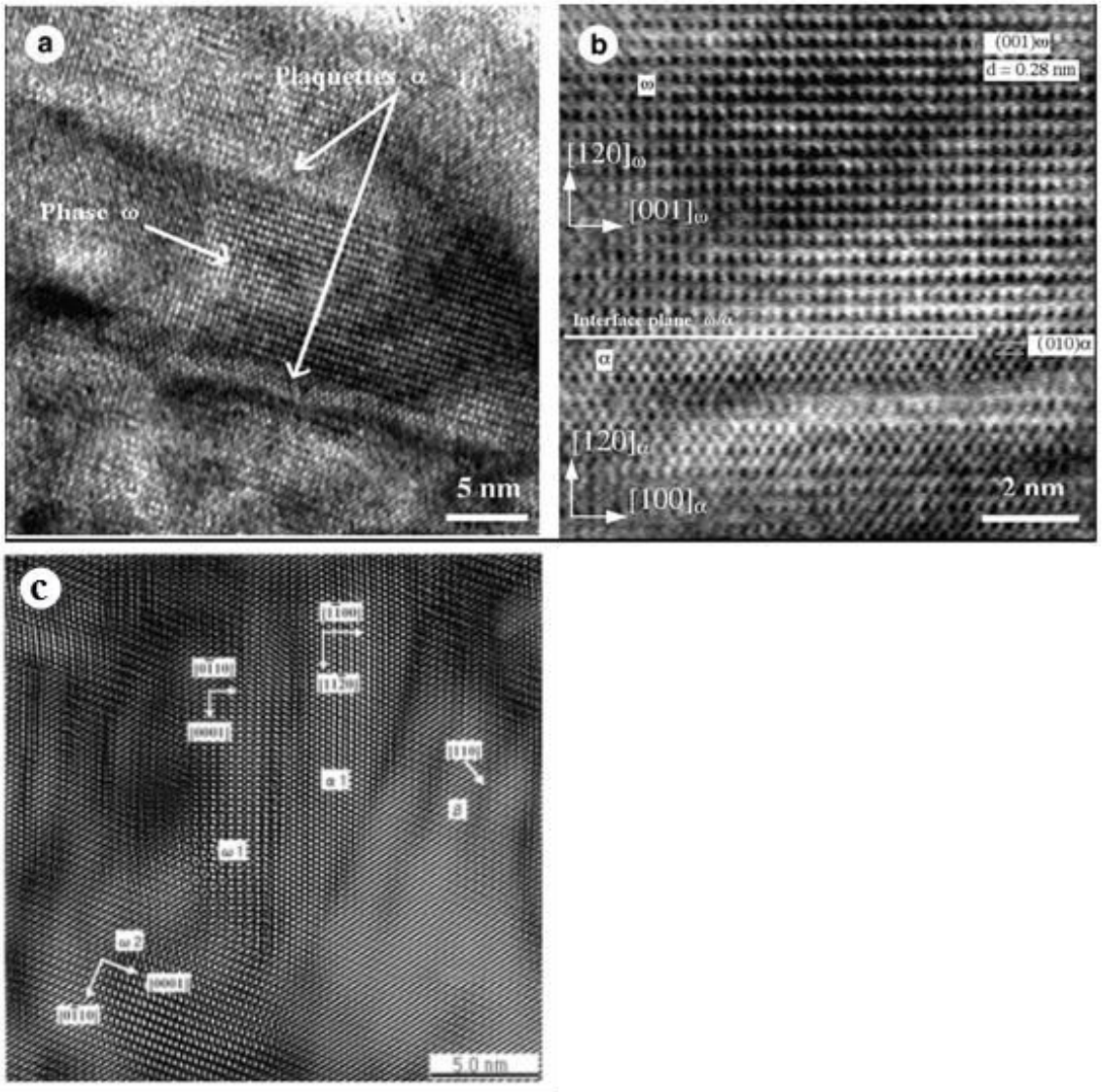

Figure 1.6 High-resolution TEM images showing the nucleation of α from ω and ω/β interface. (a) nucleation of an α phase platelets in the core of an ω particle in LCB Ti-based alloys; (b) the planar coherent interface between α and ω; (c) nucleation of an α phase lath at an ω/β interface in Ti-10-2-3 alloy.

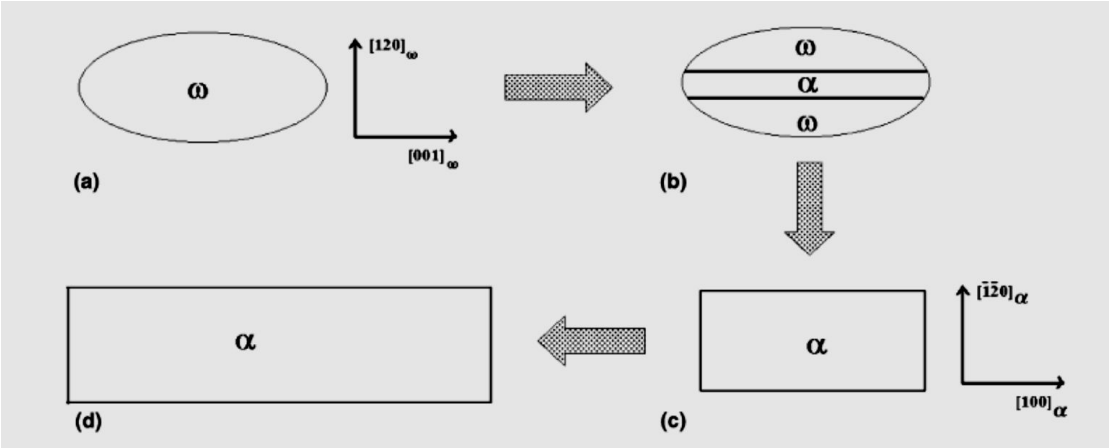

Figure 1.7 Nucleation and growth model of α-phase: (a) ω phase acting as heterogeneous nucleation, (b) α growth from ω consumption, (c) ω disappearance and (d) α growth from β consumption [53].

1.3.3 β to α transformation

The phase transformation from β to α in metastable β Ti-alloys is a diffusion controlled nucleation and growth process, and often occurs with two ways of β->α, and β->ω, ω->α. The nucleation and growth of α phase obey Burgers orientation relationship (OR). Figure 1.8a shows the schematic diagram of Burgers orientation relationship between α and β phase. These differently orientated α formed during the same nucleation event are known as *variants*. The feasible number of such variants is determined by the orientation relationship (OR). The six slip planes and the two slip directions of the β titanium unit cell give a maximum of 12 variants of orientation to the α. The Burgers orientation relationships between α and β are given below:

(0001) α // {011} β; <11-20> α //<1-11> β; {1-100} α // {121} β

However, during the actual phase transformation, upon cooling from the β phase field of titanium the most densely packed planes of the bcc β phase {110} transform to the basal planes {0001} of the hexagonal α phase. The distance between the basal planes in α is slightly larger than the corresponding distance between the

{110} planes. Therefore, the α/β transformation causes a slight atomic distortion (Figure 1.8b). This leads to a slight contraction of the c-axis relative to the a-axis in the hcp α and reduces the c/a-ratio below the value of ideally close packed hexagonal atomic structures. A slight increase in volume is observed macroscopically during cooling through the α/β transformation temperature.

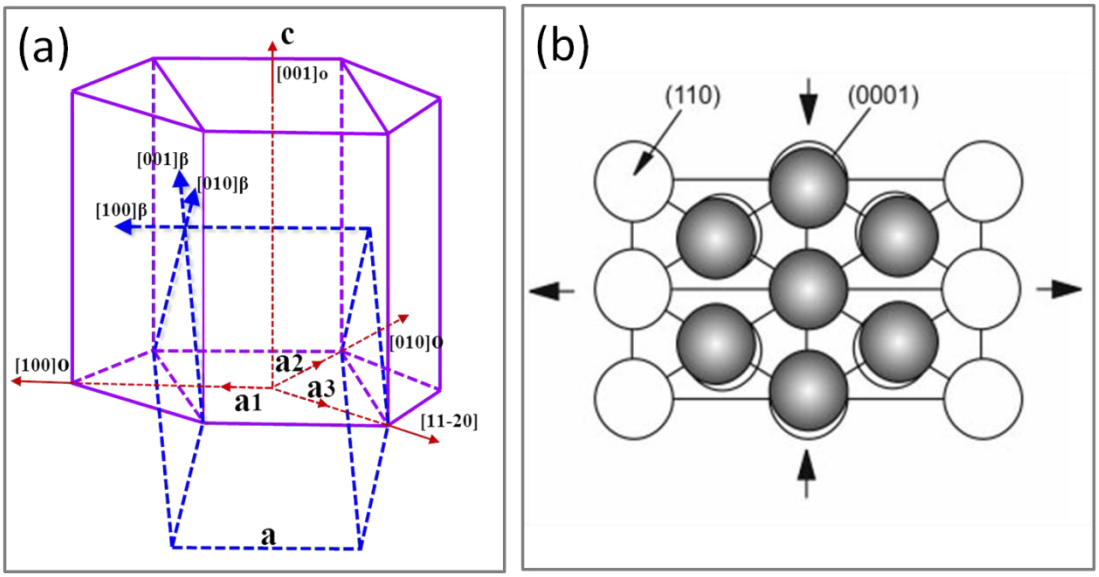

Figure 1.8 (a) the schematic diagram of Burgers orientation between α and β phase; (b) β/α transformation according to Burgers relationship [2].

1.4 Deformation mechanism in metastable β titanium alloys

The deformation mechanism of metastable β Ti-alloys generally included dislocation slip, mechanical twinning and stress-induced phase transformation. Banerjee et al. **[15]** schematically summarizes the variety of inelastic responses of the β phase to stress (Figure 1.9). It can be seen from Figure 1.9 that dislocation slip transforms to {112}<111>-type twinning and {332}<11$\bar{3}$>-type twinning with the stability of the β phase decreasing. At the same time, the stress-induced phase transformation also often occurs in these alloys.

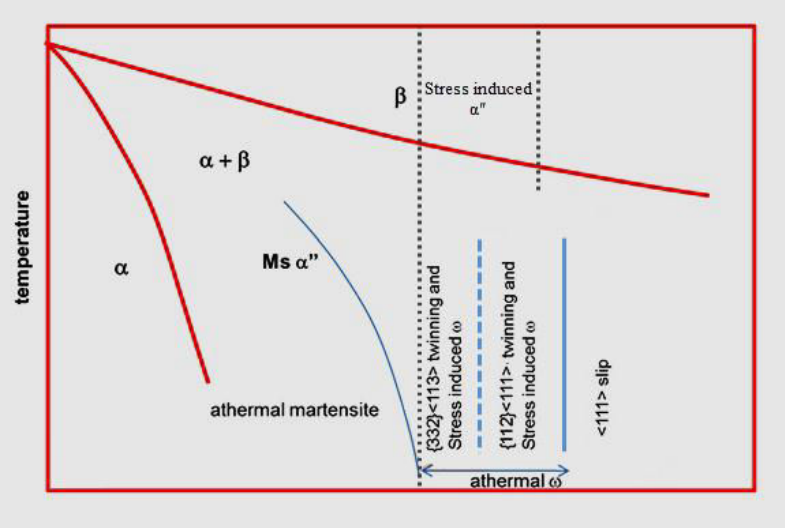

Figure 1.9 A schematic diagram of the effect of β alloys content on β phase deformation mechanism.

1.4.1 Stress-induced martensitic transformation

The stress-induced martensitic α" phase transformation is one of the most important features in metastable β alloys. The reversible SIM α" has recently attracted great attention in developments of shape memory Ti alloys and multifunctional Ti alloys with high strength and low elastic modulus, resulting in the marked pseudo-elasticity and strain recovery. A schematic of the crystal structures of the β phase and α" orthorhombic martensite phase is shown in Figure 1.10. The lattice correspondence between β and α" phases can be expressed as follows:

$[100]\alpha''//[100]\beta$, $[010]\alpha''//[001]\beta$, $[001]\alpha''//[0\bar{1}0]\beta$

$(100)\alpha''//(110)\beta$, $[111]\alpha''//[111]\beta$

In fact, extensively investigations **[57-59]** have been carried out on the SIM transformation during elastic process in the metastable β Ti-alloys. Generally, the metastable materials undergoing SIM transformation during elastic process exhibits a typical stress-plateau in the tensile stress–strain curve. Figure 1.11 shows the

schematic diagram of typical stress-strain curve for an alloy undergoing SIM during elastic process. The curve delineates four stages and exists “double yield”. Stage I is the initial linear elastic region. In this stage, the parent phase undergoes an elastic deformation **[59]**. Stage II or stress plateau region corresponds to stress-induced transformation of metastable parent phase to martensite or reorientation of martensite presented in initial microstructure **[57, 58]**. In case the reorientation of martensite is responsible for deformation strain, the stress plateau is flat, but, when stress-induced martensite contributes to deformation strain, this stage is reported to exhibit gradual increase in stress with increase in strain resulting in a rising stress plateau. The deformation mechanism in stage III is not well established. The Stage IV consisted of the formed martensite and β matrix. With applying strain, dislocation slip of β matrix dominates the deformation process, because it is favorable to slip when the stress is over the Critical Resolved Shear Stress (CRSS) of slip.

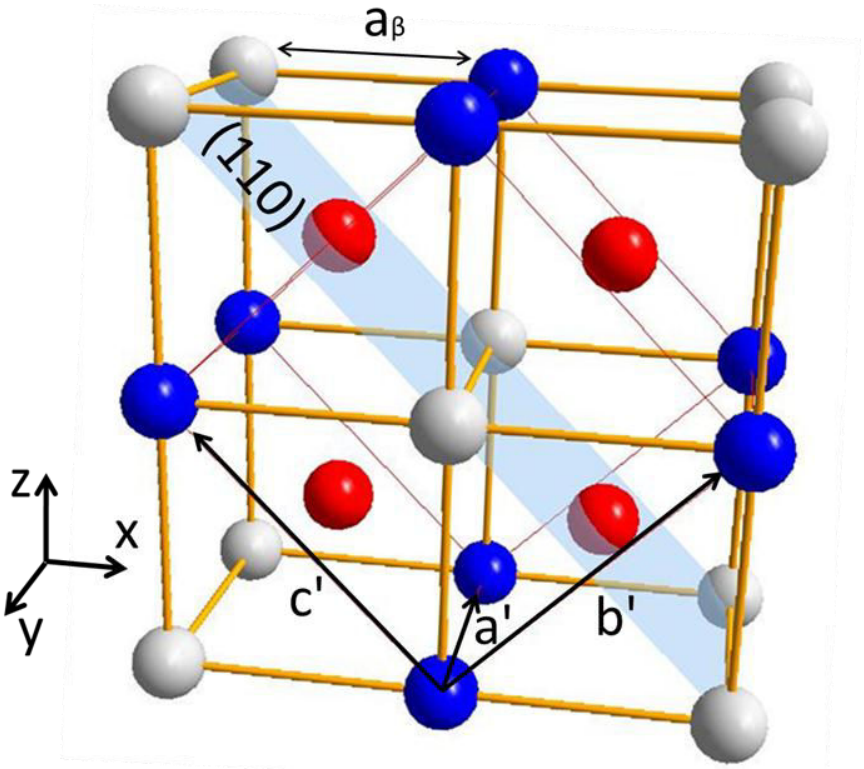

Figure 1.10 A schematic illustration exhibiting lattice correspondence between β and a˝ phases.

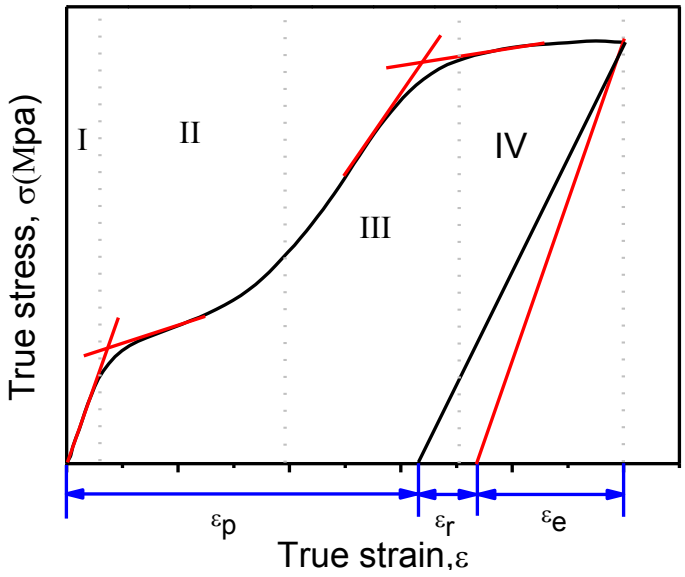

Figure 1.11 Typical stress-strain curve for an alloy undergoing SIM (number donate various stages during tensile test).

Moreover, the stress induced martensitic transformation can also occur in the plastic process in some metastable β Ti-materials **[40, 60]**. The phenomena is called transformation-induced plasticity (TRIP). The TRIP effect is very common in metastable austenitic steels, bringing about a remarkable increase in elongation and work-hardening. The TRIP-steels display high strength, excellent work-hardening and large ductility, due to the combination of the formed martensite and the hardening of the austenite contribute to the overall plastic process **[61]**. Similar with the TRIP-steels, the stress induced martensitic transformation occurred in plastic process is available to improve the mechanical behavior in the metastable β Ti-alloys.

1.4.2 Mechanical twinning

Twinning is an important deformation mechanism not only in materials with low crystal symmetry such as hexagonal (including hcp) metals but also in body-centered cubic (BCC) metals and face-centered-cubic (fcc) metals with low stacking fault energies **[62]**. In BCC structure, the {112}<11$\bar{1}$>-type is a well-known twinning system,

but the {332}<11$\bar{3}$>-type twinning is a unusual twining mode observed in some metastable alloys, like Fe–Ni–C or Fe–Be **[63]**. In β Ti-alloys, both twinning systems {112}<11$\bar{1}$> and {332}<11$\bar{3}$> have been observed, depending on the alloy composition **[39, 64]**. Hanada et al. **[38, 39, 65]** pointed that the {112}<11$\bar{1}$> twinning were usually observed in metastable and/or stable β Ti-alloys. However, the {332}<11$\bar{3}$> twinning always occurs in unstable and/or metastable β Ti-alloys, leading to a low yield stress and large elongation. Figure 1.12 shows the schematic diagram of diffraction pattern of twinning systems {112}<11$\bar{1}$> and {332}<11$\bar{3}$> with β [110] zone.

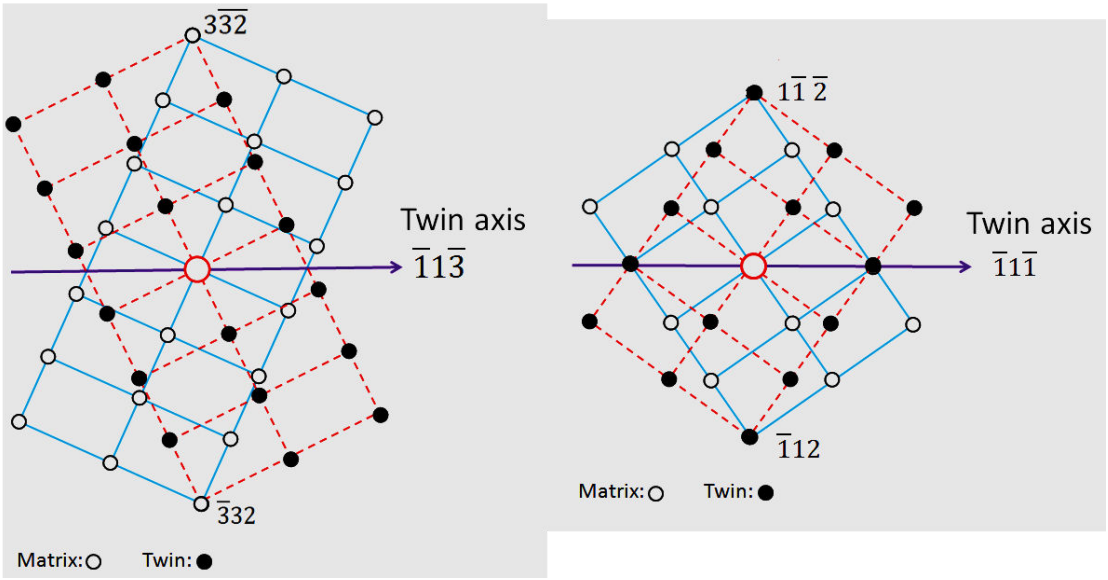

Figure 1.12 The schematic diagram of diffraction spot of {332}<11$\bar{3}$> twinning and {112}<11$\bar{1}$> twinning with β [110] zone, respectively.

The deformation mode of {332}<11$\bar{3}$> twining is an interesting feature in metastable β Ti-alloys, which strongly influences the mechanical properties of these alloys. It has been reported that the deformation of {332}<11$\bar{3}$> twinning in metastable β Ti-alloys caused a large elongation through the significant work

hardening due to the dynamic grain refinement **[66, 67]**. Several special features of {332}<11$\bar{3}$> twining were identified as follows **[68]**: (i) ease of twin intersection, together with secondary twinning inside primary twins; (ii) presence of many dislocations inside the twins and in the matrix adjacent to the twin/matrix boundary; and (iii) presence of a deformation-induced plate-like ω-phase aligned in twins with a single variant. Such special features of {332}<11$\bar{3}$> twinning that it plays an important role in improving the mechanical performance of metastable β Ti-alloys.

1.4.3 Dislocation slip

Similar to a number of BCC metals (Fe, Mo, W, V...), the metastable β titanium alloy has BCC structure at as-quenched state, and the dislocation slip is the important deformation mode. The slip systems in BCC structure are well understood. For the BCC structure, even though the most densely packed planes are the {110} planes, slip can also operate on the {112} and {123} planes, all with the same Burgers vector of type <111>, leading to 48 slip system. Furthermore, cross-slip is often observed in this BCC structure, meaning that the dislocations move from one slip plane to another one along the common <111> direction. The detailed information about the dislocation slip in BCC structure is described in elsewhere**[12]**.

References:

[1] C. Leyens, M. Peters, Titanium and titanium alloys, Wiley Online Library, 2003.
[2] G. Lütjering, J.C. Williams, Springer, Manchester, UK (2003) 1-356.
[3] T. Duerig, J. Williams, Beta Titanium Alloys in the 1980's (1983) 19-67.
[4] I. Weiss, S. Semiatin, Mater. Sci. Eng. A 243 (1998) 46-65.
[5] D. Eylon, A. Vassel, Y. Combres, R. Boyer, P. Bania, R. Schutz, JOM Journal of the Minerals, Metals and Materials Society 46 (1994) 14-15.
[6] P.J. Bania, JOM 46 (1994) 16-19.
[7] T. Saito, T. Furuta, J.H. Hwang, S. Kuramoto, K. Nishino, N. Suzuki, R. Chen, A. Yamada, K. Ito, Y. Seno, Science 300 (2003) 464.

[8] M. Abdel-Hady, K. Hinoshita, M. Morinaga, Scripta Mater. 55 (2006) 477-480.
[9] M. Abdel-Hady, H. Fuwa, K. Hinoshita, H. Kimura, Y. Shinzato, M. Morinaga, Scripta Mater. 57 (2007) 1000-1003.
[10] S. Ankem, C. Greene, Mater. Sci. Eng. A 263 (1999) 127-131.
[11] H. Matsumoto, S. Watanabe, S. Hanada, J. Alloy. Compd. 439 (2007) 146-155.
[12] G. Welsch, R. Boyer, E. Collings, (1994).
[13] B. P., TMS, Warrendale, Pennsylvania (1993) 6.
[14] H.Y. Kim, Y. Ikehara, J.I. Kim, H. Hosoda, S. Miyazaki, Acta Mater. 54 (2006) 2419-2429.
[15] D. Banerjee, J.C. Williams, Acta Mater. 61 (2013) 844-879.
[16] L. Matlakhova, A. Matlakhov, S. Monteiro, S. Fedotov, B. Goncharenko, Materials Science and Engineering A 393 (2005) 320-326.
[17] T. Ozaki, H. Matsumoto, S. Watanabe, S. Hanada, Mater. Trans. 45 (2004) 2776-2779.
[18] S. Ishiyama, S. Hanada, O. Izumi, Isij Int. 31 (1991) 807-813.
[19] M. Ikeda, S. Komatsu, Y. Nakamura, Materials transactions-JIM 45 (2004) 1106-1112.
[20] J.I. Kim, H.Y. Kim, H. Hosoda, S. Miyazaki, Mater. Trans. 46 (2005) 852-857.
[21] J. Qazi, H. Rack, B. Marquardt, JOM Journal of the Minerals, Metals and Materials Society 56 (2004) 49-51.
[22] Y.L. Hao, S.J. Li, F. Prima, R. Yang, Scripta Mater. 67 (2012) 487-490.
[23] J.Y. Zhang, F. Sun, Y.L. Hao, N. Gozdecki, E. Lebrun, P. Vermaut, R. Portier, T. Gloriant, P. Laheurte, F. Prima, Mater. Sci. Eng. A 563 (2013) 78-85.
[24] C.G. Rhodes, J.C. Williams, Metallurgical Transactions A 6 (1975) 2103-2114.
[25] A.V. Dobromyslov, V.A. Elkin, Scripta Mater. 44 (2001) 905-910.
[26] T. Ahmed, H. Rack, J. Mater. Sci. 31 (1996) 4267-4276.
[27] A. Brown, D. Clark, J. Eastabrook, K. Jepson, (1964).
[28] S. Banerjee, R. Tewari, G. Dey, Z. Metallkd. 97 (2006) 963-977.
[29] S. Sikka, Y. Vohra, R. Chidambaram, Prog. Mater. Sci. 27 (1982) 245-310.
[30] B. Hickman, North American Rockwell Corp., Thousand Oaks, Calif., 1969.
[31] P. Frost, W. Parris, L. Hirsch, J. Doig, C. Schwartz, Trans. Am. Soc. Metals 46 (1954) 231.
[32] B. Hickman, J. Mater. Sci. 4 (1969) 554-563.
[33] Yu.A Bagaryatskiy, G.I. Nosova, Phys. Metals and Metallography 13 (1962) 92.
[34] A. Devaraj, S. Nag, R. Srinivasan, R. Williams, S. Banerjee, R. Banerjee, H. Fraser, Acta Mater. 60 (2012) 596-609.
[35] H.P. Ng, A. Devaraj, S. Nag, C. Bettles, M. Gibson, H. Fraser, B. Muddle, R. Banerjee, Acta Mater. 59 (2011) 2981-2991.
[36] T. Kuan, R. Ahrens, S. Sass, Metallurgical Transactions A 6 (1975) 1767-1774.
[37] H. Xing, J. Sun, Appl. Phys. Lett. 93 (2008) 031908-031908-031903.
[38] S. Hanada, M. Ozeki, O. Izumi, Metallurgical and Materials Transactions A 16

(1985) 789-795.
[39] S. Hanada, O. Izumi, Metallurgical and Materials Transactions A 17 (1986) 1409-1420.
[40] F. Sun, J.Y. Zhang, M. Marteleur, T. Gloriant, P. Vermaut, D. Laillé, P. Castany, C. Curfs, P.J. Jacques, F. Prima, Acta Mater. 61 (2013) 6406-6417.
[41] I.A.N. Bagariatskii, G. I.; Tagunova, T. V., Soviet Physics Doklady 3 (1959) 1014.
[42] D. Ping, C. Cui, F. Yin, Y. Yamabemitarai, Scripta Mater. 54 (2006) 1305-1310.
[43] M. Blackburn, R. Jaffe, N. Promisel, H Fukutomi, C. Hartig and H Mecking, Z Metallkde, 1990, pp. 272.
[44] J. Williams, M. Blackburn, North American Rockwell Science Center, Thousand Oaks, Calif., 1969.
[45] D. De Fontaine, Acta Metall. 18 (1970) 275-279.
[46] D. De Fontaine, N.E. Paton, J.C. Williams, Acta Metall. 19 (1971) 1153-1162.
[47] J. Sanchez, D. De Fontaine, Le Journal de Physique Colloques 38 (1977) C7-444-C447-452.
[48] D. De Fontaine, Metallurgical and Materials Transactions A 19 (1988) 169-175.
[49] D. De Fontaine, O. Buck, Philosophical Magazine 27 (1973) 967-983.
[50] M.J. Blackburn, J. Williams, Boeing Scientific Research Labs., Seattle, 1968.
[51] Y. TAKEMOTO, M. HIDA, A. SAKAKIBARA, Japan Institute of Metals, Journal 57 (1993) 261-267.
[52] S. Azimzadeh, H. Rack, Metallurgical and Materials Transactions A 29 (1998) 2455-2467.
[53] F. Prima, P. Vermaut, G. Texier, D. Ansel, T. Gloriant, Scripta Mater. 54 (2006) 645-648.
[54] F. Langmayr, P. Fratzl, G. Vogl, W. Miekeley, Phys. Rev. B 49 (1994) 11759-11766.
[55] D. Moffat, D. Larbalestier, Metallurgical and Materials Transactions A 19 (1988) 1677-1686.
[56] Y. Ohmori, T. Ogo, K. Nakai, S. Kobayashi, Mater. Sci. Eng. A 312 (2001) 182-188.
[57] A. Paradkar, S. Kamat, A. Gogia, B. Kashyap, Mater. Sci. Eng. A 456 (2007) 292-299.
[58] A. Paradkar, S. Kamat, A. Gogia, B. Kashyap, Mater. Sci. Eng. A 487 (2008) 14-19.
[59] Y. Liu, H. Xiang, J. Alloy. Compd. 270 (1998) 154-159.
[60] X. Min, S. Emura, K. Tsuchiya, T. Nishimura, K. Tsuzaki, Mater. Sci. Eng. A 590 (2014) 88-96.
[61] O. Grässel, L. Krüger, G. Frommeyer, L. Meyer, Int. J. Plasticity. 16 (2000) 1391-1409.
[62] J.W. Christian, S. Mahajan, Prog. Mater. Sci. 39 (1995) 1-157.
[63] R. Richman, Gordon and Breach, New York (1964) 237.
[64] M. Oka, Y. Taniguchi, Metallurgical and Materials Transactions A 10 (1979) 651-653.
[65] S. Hanada, O. Izumi, Transactions of the Japan Institute of Metals 23 (1982)

85-94.
[66] X. Min, X. Chen, S. Emura, K. Tsuchiya, Scripta Mater. 69 (2013) 393-396.
[67] S. Hanada, O. Izumi, Metallurgical and Materials Transactions A 18 (1987) 265-271.
[68] X.H. Min, K. Tsuzaki, S. Emura, T. Sawaguchi, S. Ii, K. Tsuchiya, Mater. Sci. Eng. A 579 (2013) 164-169.

Chapter 2

Design of metastable β titanium alloys showing TRIP/TWIP effects

2.1 Introduction

From the metallurgical viewpoint, a common procedure of alloy design consists of two aspects: one is to identify and characterize the fine-scale elements of structure (crystal structure, defect structure, and microstructure); the other is to establish the relationships between properties of interest and details of the structure **[1]**. Regarding the design of Ti-alloys, several alloy design strategies are often used in the history of titanium development, such as “trial-and-error” method, the empiric Mo equivalent and the semi-empiric “d-electron alloy design method”.

Earlier attempts to design Ti-alloys mainly consisted of the empirical procedures based on experience. The methods are waste time and at a high price. However, most of compositions of Ti-alloys have been still formulated by trial-and-error experiments and empiric Mo equivalent, which by no means represent the optimum choices. For example, some new β- and α+β type alloys developed for medical implants materials, such as Ti–15Mo–5Zr–3Al, Ti–5Al–2.5Fe, Ti–12Mo–6Zr–2Fe, Ti–13Nb–13Zr and Ti–5Al–3Mo–4Zr, were formulated principally by trial-and-error **[2]**.

Aiming to save cost and time for Ti-alloy development, several theoretical prediction tools **[2-4]** have been developed. A strategy known as the d-electrons concept proposed by Morinaga **[4, 5]** is applied to design of Ti-alloys using metallic elements, in order to establish the strategic method in predicting elastic properties

of metastable β Ti-alloys and in optimizing the selection of alloying elements. The method is called as "d-electron alloy design method". In our work, we have applied the similar design strategy, though different from the Morinaga's attempts, to develop new metastable β Ti-alloys showing TRIP/TWIP effects by controlling the β stability at the plastic region.

2.2 The d-electron alloy design method

In the early 1990s, a semi-empiric integrative method, called "d-electron alloy design method", was proposed by Morinaga and colleagues **[4, 5]**. It has been confirmed by extensive experiments that this method can be used to guide the selection of adapted contents of specific alloying elements, the prediction of phase stability of alloys **[6]** and alloy properties as well **[7]**. In the method, employing a molecular orbital method (DV-Xa cluster method **[7, 8]**), electronic structures were calculated for BCC Ti alloyed with a variety of elements, and two alloying parameters were determined theoretically. One is the bond order (Bo), which is a measure of the covalent bond strength between Ti and an alloying element. The other is the mean d-orbital energy level (Md), which correlates with the electronegativity and the metallic radius of elements. For titanium alloys, the average values of Bo and Md are defined by taking the compositional averages of the parameters and denote them as $\overline{\mathrm{Bo}}$ and $\overline{\mathrm{Md}}$, respectively. The $\overline{\mathrm{Bo}}$ and $\overline{\mathrm{Md}}$ values, and the chemical compositions of the designed alloys in this study for β-Ti alloys are given in Table 2.1. Electronic parameters $\overline{\mathrm{Bo}}$ and $\overline{\mathrm{Md}}$ for each alloy were calculated from the following expressions:

$$\overline{Md} = \sum X_i (M_d)_i \text{ and } \overline{Bo} = \sum X_i (B_o)_i \quad \text{... eqn.2.1}$$

where X_i is the molar fraction of the i element and $(Md)_i$, $(Bo)_i$ is the numerical values of Md and Bo for each alloying element, respectively.

The "d-electron design method" results in a semi-empiric "stability map" (called

the $\overline{Bo}$–$\overline{Md}$ map). Figure 2.1 shows a general $\overline{Bo}$–$\overline{Md}$ map with alloys vector. The lower part of the $\overline{Bo}$–$\overline{Md}$ map, where the Bo value is less than 2.84, is proposed by Morinaga et al. **[9]**, while the part that the Bo value between 2.84 and 2.96 has been extended by Abdel-Hady et al. **[10]**. The alloys position moves in the $\overline{Bo}$–$\overline{Md}$ map, as the alloy composition varies with the composition average (Bo and Md) of the above mentioned parameters.

Table 2.1 list of Bo and Md value for β-Ti alloys

Element 3d	Bo	Md (eV)	Element 4d	Bo	Md (eV)	Element 5d	Bo	Md (eV)	New Transition Element	Bo	Md (eV)
Ti	2.790	2.447	Zr	3.086	2.934	Hf	3.110	2.975	Al	2.426	2.200
V	2.805	1.872	Nb	3.099	2.424	Ta	3.144	2.531			
Cr	2.779	1.478	Mo	3.063	1.961	W	3.125	2.072			
Mn	2.723	1.194	Tc	3.026	1.294	Re	3.061	1.490	Si	2.561	2.200
Fe	2.651	0.969	Ru	2.704	0.859	Os	2.980	1.010			
Co	2.529	0.807	Rh	2.736	0.561	Ir	3.168	0.677			
Ni	2.414	0.724	Pd	2.208	0.347	Pt	2.252	0.146	Sn	2.283	2.100
Cu	2.114	0.567	Ag	2.094	0.196	Au	1.953	0.258			

As shown in Figure 2.1, the alloying vector drawn in the Bo–Md diagram is useful in classifying elements based on their effect on the phase stability. From the starting point of pure Ti, the alloying vectors are directed mainly to the leftward part of the $\overline{Bo}$–$\overline{Md}$ map for the β-stabilizing isomorphous elements (e.g. Ta, Nb, W, Mo, V), and the eutectoid elements (e.g. Cr, Fe), respectively. The vectors of the α-stabilizing elements (e.g. Al, Sn) are directed mainly towards lower-left part of the map. However, the neutral elements (e.g. Zr, Hf) take a different vector direction towards up-right corner in the $\overline{Bo}$–$\overline{Md}$ map. Therefore, each element possesses its own attribute in stabilizing either the α phase or the β phase, regions of stabilized phase, such as α, α+β and β field, can be localized in Figure 2.1.

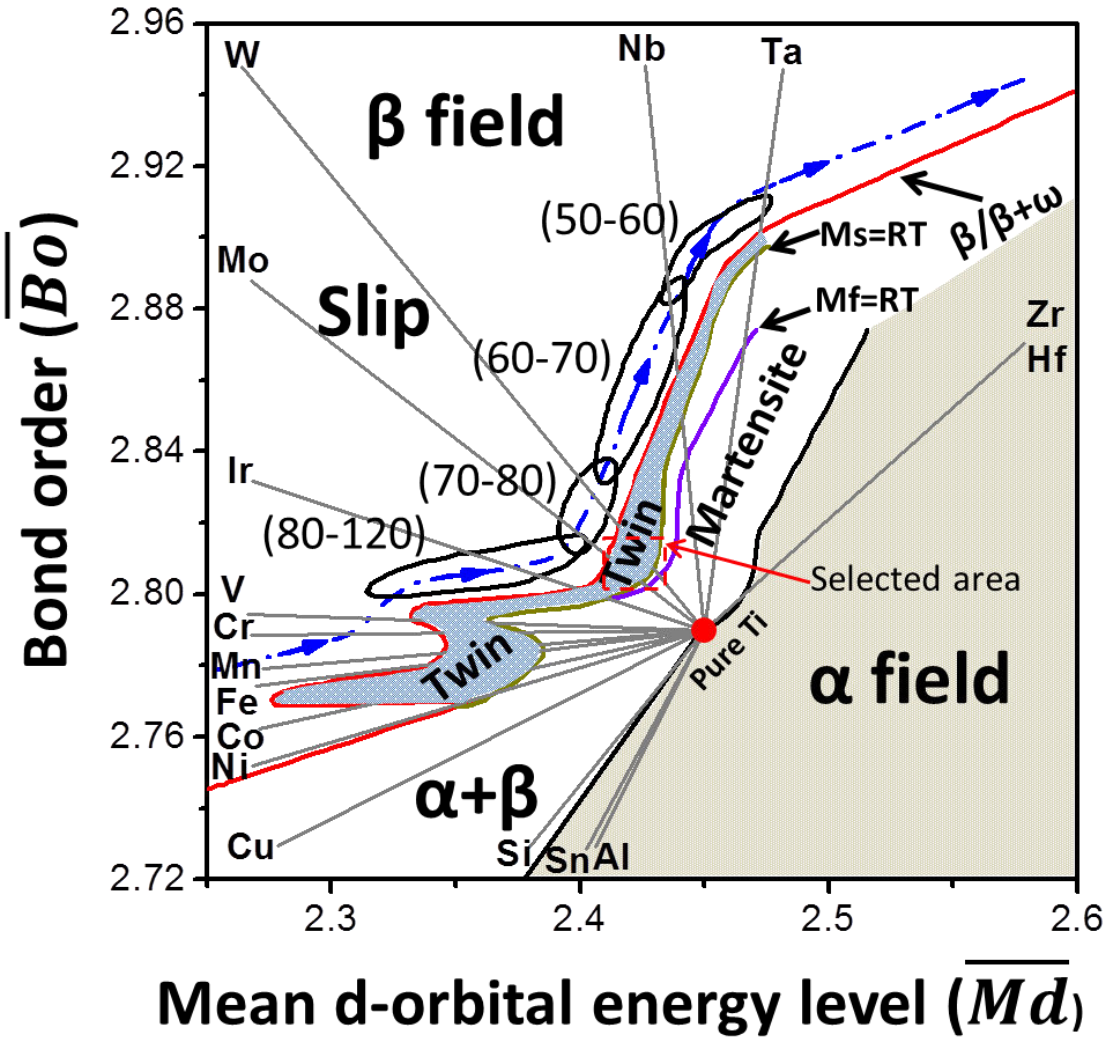

Figure 2.1 The general $\overline{\mathrm{Bo}}$–$\overline{\mathrm{Md}}$ map with alloy vector

Also, the stability of the β phase increases with increasing content of the β-stabilizing elements, in various Ti–M binary alloys (M = V, Cr, Mo, Nb, and Ta) **[10]**. It has been well known that the main deformation mechanism evolves from dislocation slip to mechanical twinning then to stress induced martensitic transformation when β phase chemical stability is decreased. As a result, different zones of "deformation modes" can be drawed on the $\overline{\mathrm{Bo}}$–$\overline{\mathrm{Md}}$ map (Figure 2.1). The boundaries, such as slip/twin, Ms=RT (room temperature) and Mf=RT are plotted on the $\overline{\mathrm{Bo}}$–$\overline{\mathrm{Md}}$ map. These boundaries can be regarded as important reference in designing new β Ti-alloys because of their indication for predicting the mechanical

stability in metastable β phase. In addition, the experimental values of moduli of elasticity of β type alloys expressed in GPa are also shown in parentheses **[9, 10]**.

This map is of great interest because it can be used as a tool to predict "as-quenched" properties of Ti-alloys, independently from the number of alloying elements. For example, the map has been extensively used for the design of the last generation of low modulus/high strength alloys **[5]**. Moreover, the map can be also used to select compositional ranges where the three main deformation mechanisms (i.e. dislocation slip, mechanical twining and stress-induced martensitic transformation) are competitive in β phase alloys.

2.3 Design of new metastable β Ti-alloys with TRIP and TWIP effects

Compared with steels or Co-Cr alloys, the currently major drawbacks of Ti-alloys are both their low ductility (uniform elongation typically less than 0.20) and their lack of work-hardening rate, which limits their application in advanced applications where superior combinations of strength and ductility are required. Indeed, "classical" Ti-based materials usually display a very low work-hardening rate, bring rapid strain localization and low ductility levels **[11]**. Nonetheless, it is reported that the activation of $\{332\}\langle 11\bar{3}\rangle$-type twinning in some metastable β-Ti alloys **[12-15]**, could result in a significant increase in the work-hardening rate, though this increase has not yet been fully explained in BCC materials. On the other hand, the occurrence of twinning is generally accompanied by a small yield stress **[16]**. Furthermore, the effect of mechanically induced martensitic transformation on the plastic properties of Ti alloys has hardly been investigated and optimized.

Moreover, it is well known that a strategy based on TRIP or TWIP effects is often used to dedicate to a general improvement of the mechanical properties in steels materials **[17]**. The strategy has been widely investigated for the development of

new high performance materials **[18]**. Taking inspiration from the superior mechanical performances of TRIP and TWIP effects materials, we think that it is possible to design new β metastable Ti-alloys that can enable a combination of activation of mechanical twinning and stress induced martensitic transformation. However, it is quite a challenge to design such alloys showing combined TRIP/TWIP effects, which are expected in resulting large ductility and high work-hardening rate. As a validation of the design strategy, a model of new binary metastable β alloy was firstly designed to gain an improved combination of high ductility and work-hardening rate. The preliminary experimental results have proved that the concept is feasible. Then, a series of ternary alloys are developed to enlarge the family of combined TRIP/TWIP Ti-materials.

The designing strategy of the new binary metastable β Ti-alloy is to activate a combined deformation mechanism involved in simultaneous twinning and phase transformations. The protocol of "d-electron alloy design" introduced above, was applied in formulating the chemical composition and predicting its deformation mechanism. From the $\overline{\mathrm{Bo}}$–$\overline{\mathrm{Md}}$ map, there exists an area where the transition among dislocation slip, mechanical twinning and stress induced martensitic transformation will occur. In the region, some β stabilizer elements such as Nb, W, Mo, V and Cr, have suitable alloying vectors (indicated in Figure 2.1), thus opening possibilities to trigger various deformation modes upon mechanical deformation. Here, we selected the Mo element as a good candidate for designing the model of new binary metastable β titanium alloy. Three reasons are likely to be explained for taking into account the Mo element. Firstly, the Mo element is a standard β-stabilizer compared with other β-stabilizer. Secondly, the rectangle selected area in Figure 2.1 shows an interesting zone because of its relatively large area with a large distance between slip/twin line and SIM line, which facilitates potential manipulations on alloy chemical stability. Therefore, it is very possible to achieve combined TRIP/TWIP effects when the so-designed binary alloy located in the region. Moreover, a number

of Ti-Mo and Ti-Mo-based alloys have been extensively investigated in SIM and mechanical twining. The reported experimental results can be regarded as important references in the model alloy designed procedure.

Along the Mo vector, we select a region ($\overline{Bo}$~2.80-2.82, $\overline{Md}$~2.41-2.43) from the general $\overline{Bo}$–$\overline{Md}$ map. Figure 2.2 shows the $\overline{Bo}$–$\overline{Md}$ map of the selected region from Figure 2.1, in which two boundaries (i.e. slip/twinning boundary and Ms=RT) were plotted. The alloying vector of Mo is also represented in this figure. It is worth noting that there exists a very important line in Figure 2.2 (red dash line), located halfway between the boundaries of the domains of mechanical twinning and SIM. Due to the intermediate stability of the β phase between pure twining and pure SIM, both TRIP and TWIP effects are expected to be active simultaneously when alloy composition located in the line. We called the line as “iso-stability” line for combined TRIP and TWIP effects. Therefore, along the alloying vector of Mo, a cross-point with the values Bo=2.807 and Md=2.416, is located in the “iso-stability” line. Through calculation, the $\overline{Bo}$ and $\overline{Md}$ value of Ti-12Mo alloy is located in the d-electron of coordinate the cross-point. Thus, the Ti-12Mo alloy was chosen as a candidate to investigate the possible TRIP and TWIP effects. Through TEM microstructural analysis, the SIM transformation and mechanical twining were confirmed to occur in the deformed samples of the Ti-12Mo upon deformation.

In order to enlarge the titanium TRIP/TWIP family of alloys to ternary metastable β Ti-alloys, based on the design route of Ti-12Mo alloy, the third alloying elements were added into the Ti-12Mo alloy by using “d-electron design method”. Two sets of ternary Ti-Mo based alloys were designed. One set is adding third alloying elements but to keep the $\overline{Bo}$ and $\overline{Md}$ of the ternary alloys moving along the “iso-stability” line. By correlating two alloying vectors, Ti-Mo and Ti-W (adjacent to Ti-Mo vector) on the $\overline{Bo}$–$\overline{Md}$ map, a ternary composition, Ti-9Mo-6W (wt.%), can

be given. The d-electron coordinate of this ternary alloy at the (2.809, 2.417) selected near the Ti-12Mo position was located in the "iso-stability" line (position is indicated in Figure 2.2). The ternary alloy was expected to display better mechanical behavior compared with the model Ti-12Mo alloy, keeping combined the TRIP and TWIP effects. The other set is adding neutral element Zr into the Ti-12Mo alloy. The compositions of Ti-12MoXZr (X=1, 3, 5) (wt. %) were designed to investigate the effects of the neutral Zr element on mechanical and microstructural behavior of TRIP/TWIP alloys.

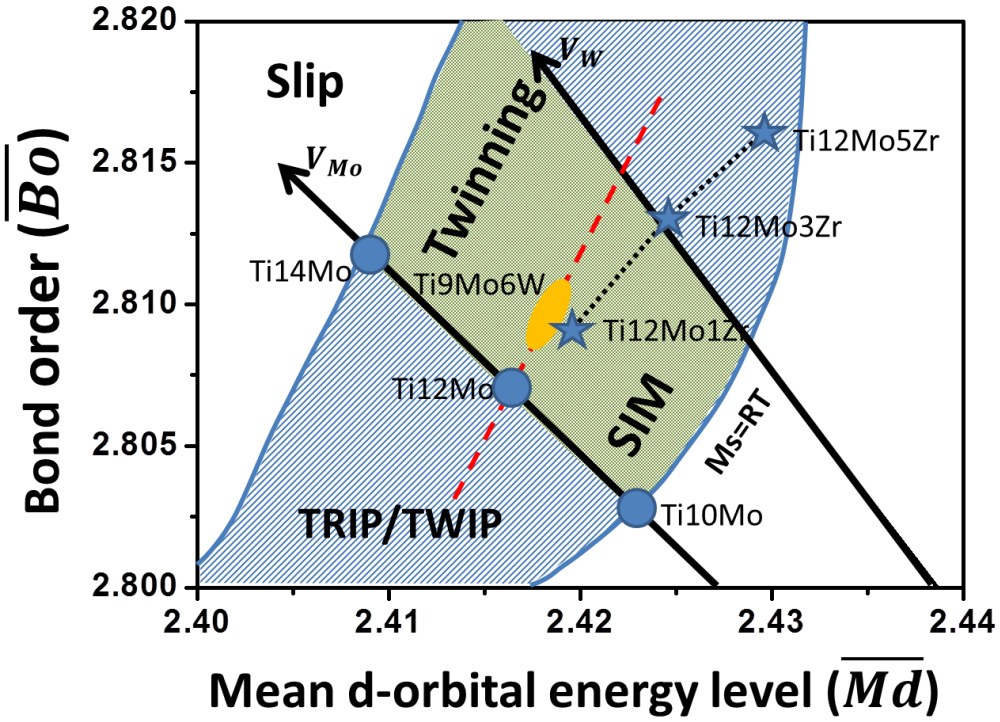

Figure 2.2 The magnified area in Bo-Md map presents different zones of deformation mechanisms. Ti-Mo/W vectors and the formulated chemical compositions are indicated in the map.

In the alloy design procedure, the other electronic parameter, the electron/atom ratio (e/a), was also used to determine the alloy compositions as a supplementary reference. It has been reported in literatures **[19, 20]** that the parameter e/a is regarded as a dominant factor in controlling the elastic properties of bcc transition metals. Some metastable β Ti-alloys with low Young's modulus **[19, 21]**

(e.g. Ti–24Nb–4Zr–7.9Sn (wt. %) **[19]**) were designed via controlling the parameter e/a. Regarding the design of our ternary alloys, a problem is that the given position of the $\overline{\mathrm{Bo}}$ and $\overline{\mathrm{Md}}$ on the $\overline{\mathrm{Bo}}$–$\overline{\mathrm{Md}}$ map may bring about several different ternary compositions. In order to resolve the problem, we selected the parameter e/a as references in determining the ternary alloy compositions. Namely, the parameter e/a values of ternary alloys keep the almost same level with that of the model Ti-12Mo alloy. Table 2.2 lists the calculated results of the electronic parameters ($\overline{\mathrm{Bo}}$, $\overline{\mathrm{Md}}$ and e/a). Meanwhile, the Mo equivalent of each alloy is also presented in Table 2.2.

After designing the Ti-Mo based alloys, their mechanical behaviors and microstructures were characterized in detail by several characterization tools. The mechanical behavior and microstructural evolution of the binary model Ti-12Mo will be presented in chapter 4. The feasibility that “d-electron design method” applied in guiding to design ternary metastable β Ti-alloys with TRIP/TWIP effects will be discussed in chapter 6. The influence of adding third alloys elements on deformation mechanism and microstructural evolution will be also described in chapter 6.

Table 2.2 The composition, Bo and Md, e/a and [Mo]eq for designed alloys

Alloys (wt%)	Bo	Md	e/a	[Mo]eq
Ti-12Mo	2.807	2.416	4.127	12
Ti-9Mo6W	2.809	2.417	4.133	11.6
Ti-12Mo1Zr	2.809	2.419	4.128	12
Ti-12Mo3Zr	2.813	2.424	4.129	12
Ti-12Mo5Zr	2.816	2.429	4.131	12

References:

[1] V.F. Zackay, E.R. Parker, Annu. Rev. Mater. Sci. 6 (1976) 139-155.
[2] Y. Song, D.S. Xu, R. Yang, D. Li, W.T. Wu, Z.X. Guo, Mater. Sci. Eng. A 260 (1999) 269-274.
[3] D. Raabe, B. Sander, M. Friák, D. Ma, J. Neugebauer, Acta Mater. 55 (2007) 4475-4487.
[4] M. Morinaga, N. Yukawa, T. Maya, K. Sone, H. Adachi, Sixth World Conference on Titanium. III;, 6-9 June 1988. , Cannes; France; , 1988, pp. 1601-1606.
[5] D. Kuroda, M. Niinomi, M. Morinaga, Y. Kato, T. Yashiro, Mater. Sci. Eng. A 243 (1998) 244-249.
[6] M. Morinaga, N. Yukawa, H. Ezaki, H. Adachi, Philosophical magazine. A. Physics of condensed matter. Defects and mechanical properties 51 (1985) 223-246.
[7] M. Morinaga, N. Yukawa, H. Adachi, H. Ezaki, Superalloys 1984 (1984) 523-532.
[8] M. Morinaga, H. Adachi, M. Tsukada, J. Phys. Chem. Solids 44 (1983) 301-306.
[9] M. Morinaga, M. Kato, T. Kamimura, M. Fukumotom, I.Harada, K. Kubo, Titanium 1992, Science and Technology, Proc. 7th Int. Conf. on Titanium, , San Diego, CA, USA, , 1992, pp. 276-283.
[10] M. Abdel-Hady, K. Hinoshita, M. Morinaga, Scripta Mater. 55 (2006) 477-480.
[11] C. Leyens, M. Peters, Titanium and titanium alloys, Wiley Online Library, 2003.
[12] T. Furuhara, K. Kishimoto, T. Maki, Materials transactions-JIM 35 (1994) 843-843.
[13] X. Min, X. Chen, S. Emura, K. Tsuchiya, Scripta Mater. 69 (2013) 393-396.
[14] X. Min, K. Tsuzaki, S. Emura, T. Sawaguchi, S. Ii, K. Tsuchiya, Mater. Sci. Eng. A 579 (2013) 164-169.
[15] S. Hanada, O. Izumi, J. Mater. Sci. 21 (1986) 4131-4139.
[16] H. Tobe, H.Y. Kim, T. Inamura, H. Hosoda, S. Miyazaki, Acta Mater. 64 (2014) 345-355.
[17] O. Grässel, L. Krüger, G. Frommeyer, L. Meyer, Int. J. Plasticity. 16 (2000) 1391-1409.
[18] O. Bouaziz, S. Allain, C. Scott, P. Cugy, D. Barbier, Current Opinion in Solid State and Materials Science 15 (2011) 141-168.
[19] Y.L. Hao, S.J. Li, S.Y. Sun, C.Y. Zheng, R. Yang, Acta Biomater. 3 (2007) 277-286.
[20] M. Tane, S. Akita, T. Nakano, K. Hagihara, Y. Umakoshi, M. Niinomi, H. Nakajima, Acta Mater. 56 (2008) 2856-2863.
[21] T. Saito, T. Furuta, J.H. Hwang, S. Kuramoto, K. Nishino, N. Suzuki, R. Chen, A. Yamada, K. Ito, Y. Seno, Science 300 (2003) 464.

Chapter 3

Experimental procedure

3.1 Introduction

In this chapter, we introduced the experimental techniques and analytical software used for fabrication, manufacturing, heat-treatment and characterization of the designed alloys. As shown in Figure 3.1, after designing Ti-Mo based alloys, the elaboration, homogenization treatment and cold-rolled are applied. Subsequently thermal-treatments are employed in the cold-rolled sheets. Then, tensile tests samples are taken from the heat-treated sheets. Finally, the characterizations of mechanical behavior, phase constitutions and microstructural observations are applied. Meanwhile, the different thermal treatments were designed and applied to the alloys in order to improve the mechanical behaviors.

3.2 Fabrication and cold-rolling process

3.2.1 Ti-12Mo binary model alloy

Table 3.1 Ingot chemical composition (wt.%).

Mo	Fe	H	O	N	C	Ti
12.3	0.02	0.004	0.06	0.004	0.011	Balanced

The Ti-12Mo (wt. %) alloy was melted with pure Ti and pure Mo materials by the self-consumable melting technique in Northwest Institute for Nonferrous Metal Research (NIN), xi'an, China. The ingot is about 10kg and its chemical composition was measured (Table 3.1).

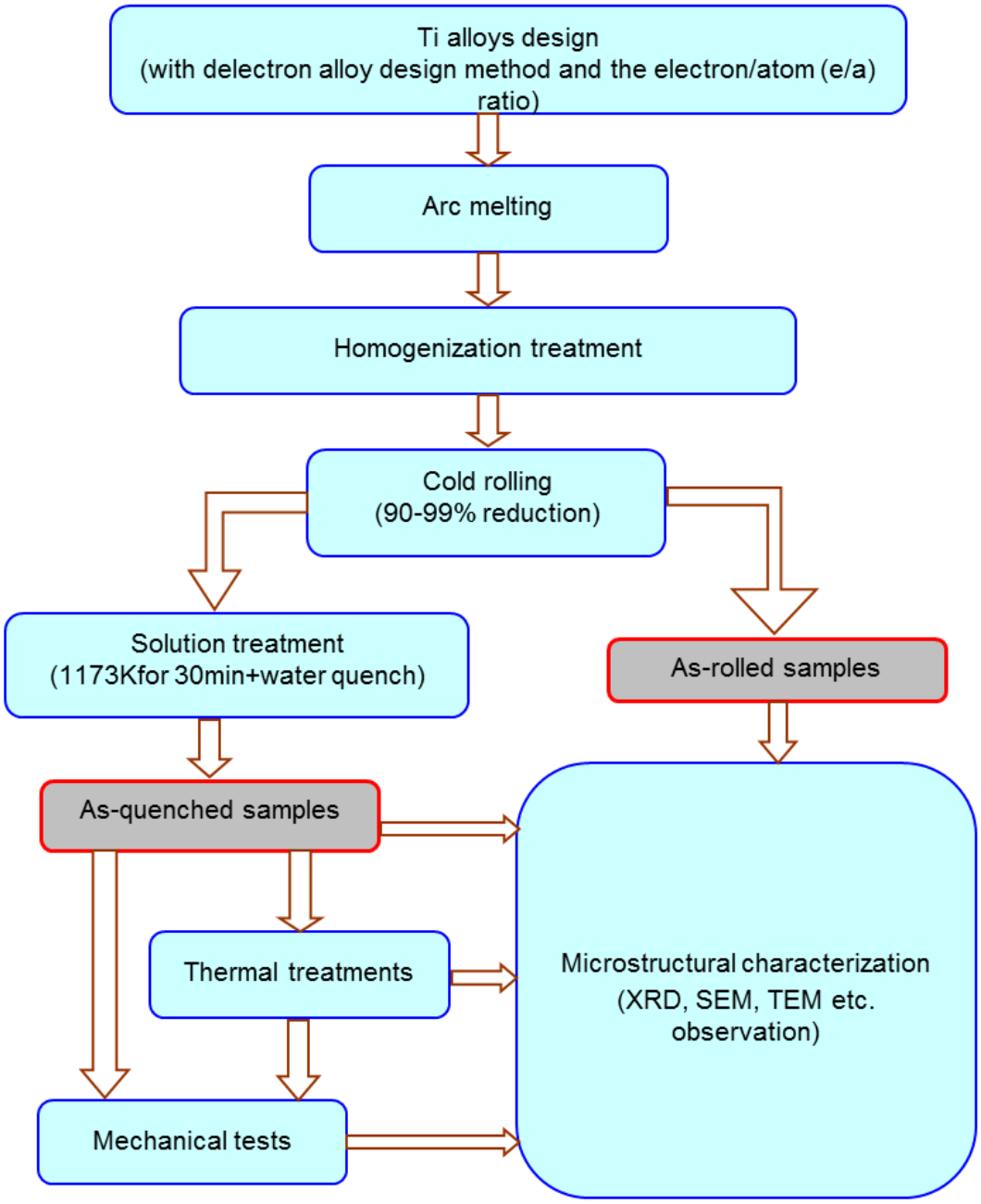

Figure 3.1 The simple procedure diagram of research route for investigated alloys.

3.2.2 Ti-9Mo-6W and Ti-12Mo-xZr ternary alloys

The ingots of Ti-9Mo-6W and Ti-12Mo-xZr (wt. %) were melted by vacuum arc melting furnace (Mini Arc Melting System MAM-1). Each ingot was about 20g. Figure 3.2 shows the photograph of Mini Arc Melting System. It consists of four main parts:

a high vacuum chamber with a large viewing glass; the water-cooled electrode (electrode tip made of tungsten); a water-cooled copper base plate and the operating handle. During elaboration of these ternary alloys, we selected Ti-12Mo material as master alloy. Pieces of Ti-12Mo alloy and pieces of high-purity titanium, tungsten or zirconium plates were fully mixed according to the designed composition. The mixtures of raw materials were subsequently melted by tungsten electrode under argon atmosphere. In the melting process, the alloy ingots were melted for at least five times, and flipped over each time before melting, then finally formed into cylinder shape. After melting, the ingots were homogenized at 900°C for 24h under high vacuum of 10^{-6} Pa using our laboratory self-designed device.

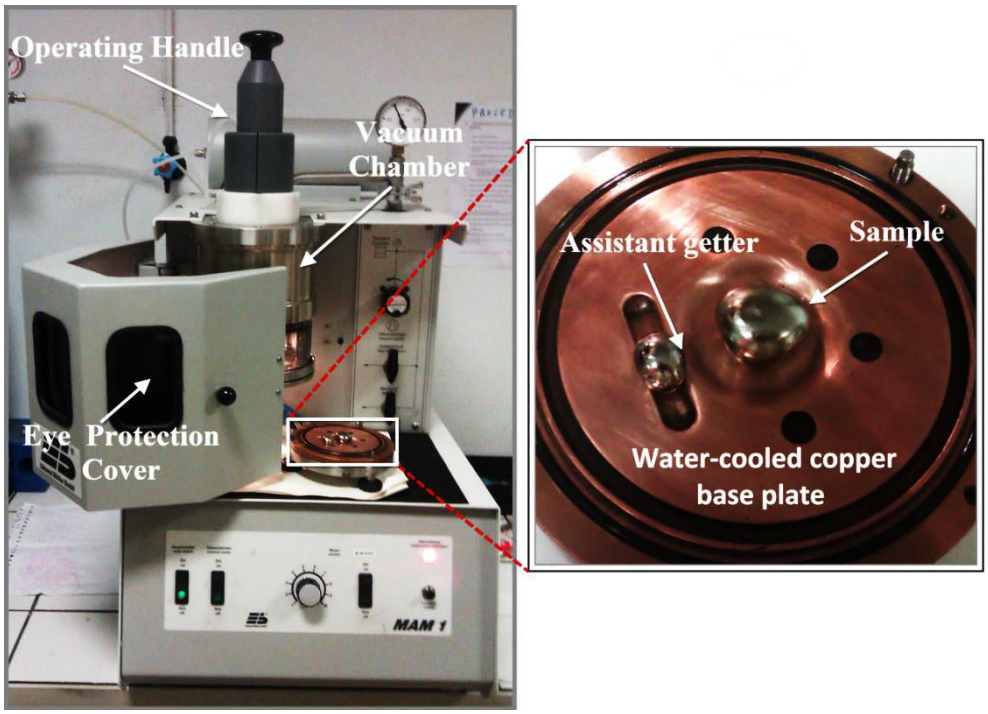

Figure 3.2 The photograph of the vacuum arc melting furnace and melted sample.

3.2.3 Cold-rolling procedure

After homogenization treatment and water-quenching, the ingots were cold-rolled by cold-rolling machine at room temperature. A scheme of rolling process was shown in Figure 3.3a. During the rolling process, a very important parameter is the deformation rate (R). The amount of deformation “R” achieved in a flat rolling

operation (thickness reduction) is determined by the relationship:

$R = 100\% * (H_0 – H)/H_0$ . . . eqn. 3.1

where, H_0 is the thickness before rolling, H is the thickness after rolling. Metastable β Ti-alloys generally possess high cold-rolling rate because of their good workability **[1]**. The initial thickness of the sample was 5~10mm, the final thickness reached 0.5mm via over 95% reduction. Figure 3.3b shows the Ti-12Mo as-quenched sample taken from the ingot and the corresponding as-rolled sheet (R=95%). The as-rolled sheet with smooth edge demonstrates that the alloy displays an excellent cold workability of designed alloy at solution-treatment (ST) state.

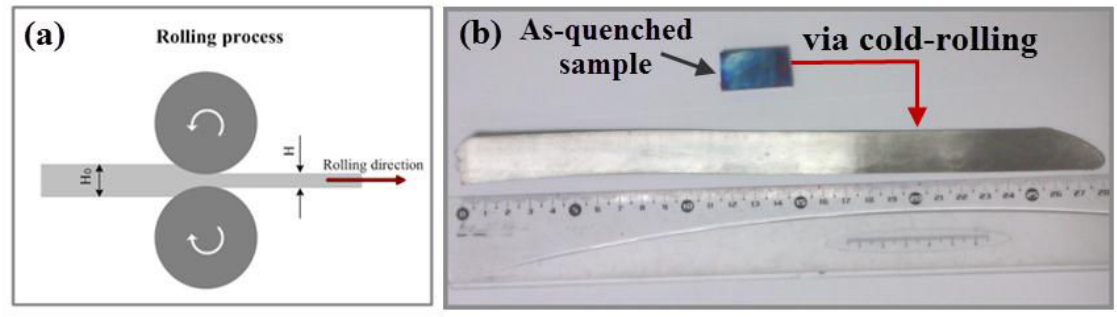

Figure 3.3 (a) the scheme of rolling process; (b) as-quenched ingot and as-rolled sheet of Ti-12Mo alloy.

3.3 Thermo-mechanical treatment and thermal analysis

3.3.1 Thermal treatment procedure

It is easy to form a layer of oxidation on the surface of Ti-alloys specimen when treated at high temperature. The oxidized layer can affect significantly the mechanical properties of Ti-alloys. As a consequence, the thermal treatment is better to be carried out under protective atmosphere. In our work, a vacuum tube furnace with water-quenched accessory was often used in thermal treatments. Figure 3.4 shows the photograph of this furnace and the corresponding schematic buildup of the furnace. It contains four main parts: heating system, controlling system, cooling

system and vacuum system. Before heating the samples, the thermal parameters such as heating temperate and holding time were preset via controlling system. The samples were dropped into the water container through fusing the titanium wire in the trigger circuit when the thermal treatment ended.

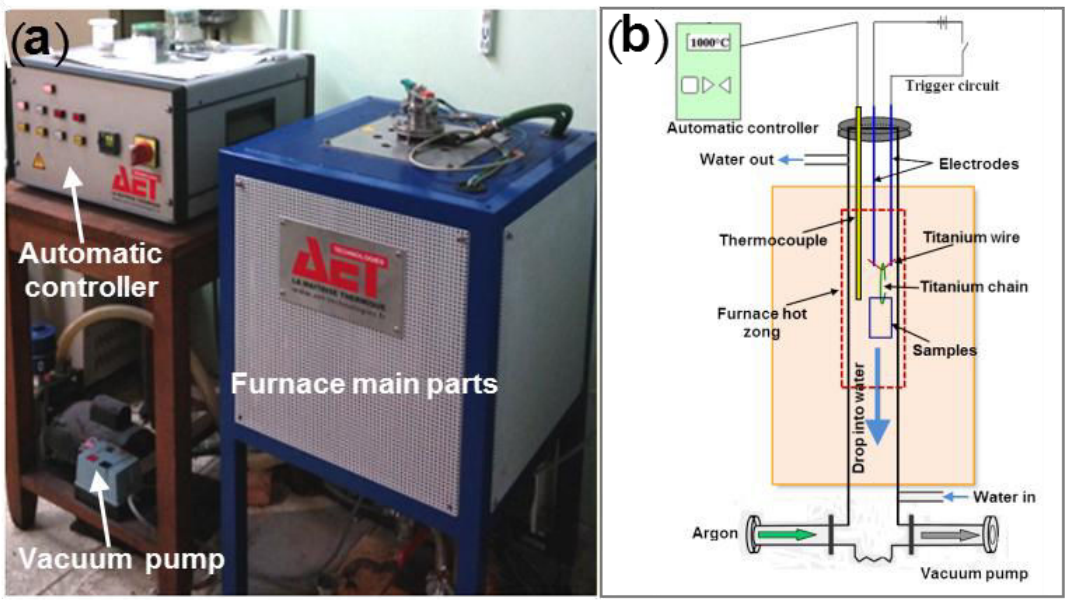

Figure 3.4 (a) the water-quenched furnace apparatus and (b) the corresponding schematic diagram of the water-quenched furnace.

After cold-rolling, the β grain of as-quenched ingots were completely destroyed due to the heavily deformation. The as-rolled samples display extremely high strength without any ductility. In order to restore the β metastable state, solution treatment was applied on the as-rolled sheets. For the designed alloys, the cold rolled sheets were usually heat-treated at 900°C (over their β transus temperature) for 30min and then water quenched. The samples via solution treatment were called ST samples.

The mechanical properties of ST samples can be improved through thermal-mechanical treatments. Recently, it has been reported that several thermo-mechanical strategies, e.g. low-temperature-high-temperature two-step ageing **[2-4]** and β annealed treatment **[5]**, were adopted to introduce ω or α into

the β matrix phase to improve the mechanical properties of metastable β alloys. In this work, we proposed a low temperature aging/short time treatment strategy (LTA). The objective is to manipulate the ω phase transformation without excessive modification of β matrix chemical composition, keeping the possibility for combined TRIP/TWIP effects to occur. The schematic procedure of LTA is shown in Figure 3.5.

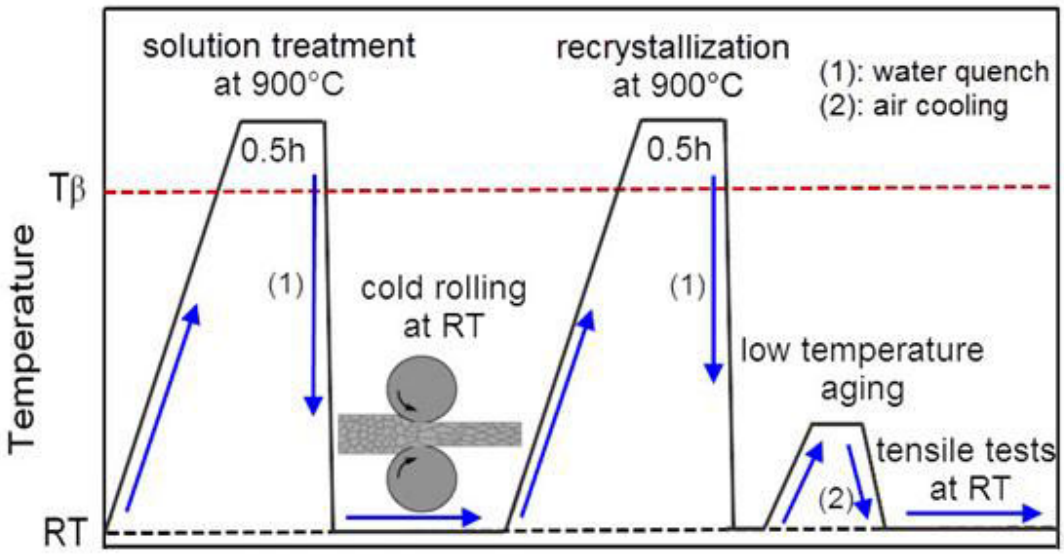

Figure 3.5 Schematic illustration of the thermo-mechanical process for LTA treatment.

3.3.2 Electrical resistivity measurement

The Electrical resistivity is very sensitive to the dislocation density, small-scale precipitates, solute content and phase transformation **[6, 7]** in metal materials. In this work, the Ti-Mo based alloys were characterized by using isochronal or isothermal electrical resistivity measurements (ERM) to investigate the phase transformation. Specimens for electrical resistivity measurements were cut into a thin 20mm×2mm×0.5mm bar from ST sheets. The ERMs were performed by using the four-probe method with a serial electrical circuit set-up composed of: the specimen (in contact with the thermocouple for measuring the temperature), a reference resistor Rref (2Ω), a d.c. source and a computer-controlled data acquisition system (self-designed apparatus). The circuit diagram of four-probe method

measurements is shown in Figure 3.6. All the experiments were carried out under high vacuum (10^{-6} mbar). A constant heating rate of 2 °C/min was used for isochronal analysis methods. Before starting a run, at the initial time t_i, R_i and V_i were the initial resistance of the sample and the initial voltage measured across the sample, respectively.

$$\frac{V_i}{V_f} = \frac{R_i}{R_f} \quad \text{. . . eqn. 3.2}$$

At time t, the measured voltage are V across the sample and V_f across the reference resistor.

$$\frac{\left(\frac{V}{V_f}\right)t}{\left(\frac{V_i}{V_f}\right)t_i} = \frac{\frac{R}{R_f}}{\frac{R_i}{R_f}} = \frac{R}{R_i} \quad \text{. . . eqn. 3.3}$$

If we neglect the thermal expansion of the sample, the electrical resistivity of the sample at t time can be calculated as:

$$\frac{\rho}{\rho_i} = \frac{V}{V_i} = \frac{R}{R_i} \quad \text{. . . eqn. 3.4}$$

where ρ and ρ_i are the electrical resistivity at t time and initial resistivity at room temperature, respectively. Thus, the electrical resistivity ratio plotted as a function of temperature shows the structural transformations and the kinetic of the transformation.

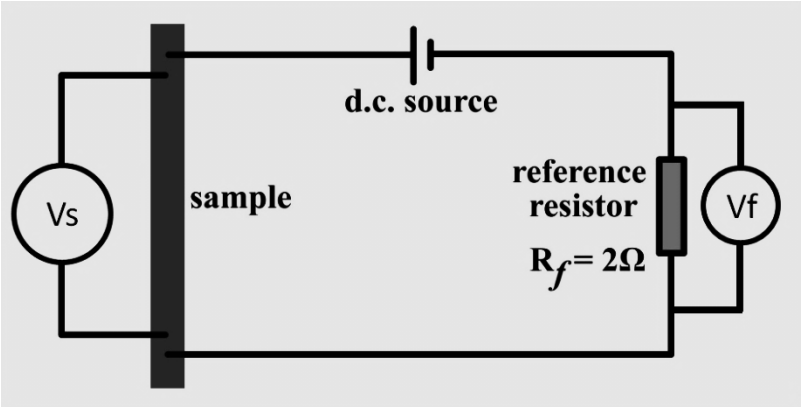

Figure 3.6 Circuit diagram of the experimental set-up for 4-point resistivity measurements

3.4 Microstructural characterization methods

3.4.1 Optical microscope and mechanical polishing

The optical microscope (OLYMPUS PME) was used observe the grain size or deformation bands at low magnification. The samples for OM observations were cut by wet abrasive cut-off machine (BRILLANT 210). The machined samples were mounted by using Beuhler simplimet® 1000 mounting machine with conductive phenolic hot mounting resin (for SEM observation). The mounted samples were polished mechanically on 800, 1200, 2400 and 4000 grit SiC papers. Subsequently, the mounted samples were polished using 1, 0.5, 0.3 and 0.05 microns colloidal alumina solution. Finally, the samples were cleaned in alcohol for 5~10 minutes using ultrasonic cleaning equipment and chemically etched with a chemical solution H2O, HNO3 and HF (5:3:1) (vol.%).

3.4.2 X-ray diffraction

In the work, the conventional X-ray diffraction (XRD) was carried out by PANalytical X'Pert Pro diffractometer with CuKα1 radiation operating at 45kV and 40mA. Furthermore, In-situ synchrotron X-ray diffraction was performed at the European Synchrotron Radiation Facility (ESRF) in Grenoble, France, on the ID31 beam line. In this work, the in-situ XRD was applied on the Ti-12Mo alloy. The tensile sample with gauge width of 4mm and 0.5mm in thickness is placed at the center of the furnace on a rotating sample holder. The incident X-ray wavelength was 0.4 Å. Data collection was performed over the angular range 2-14°, with a step size of 0.005°. Nine scanning stages were carried out at room temperature, starting from the unloaded state, then for increasingly loaded states up to a strain of 0.08 and finally after unloading. Analysis of the diffraction patterns consisted in identifying the phases corresponding to the different peaks and then estimating the lattice parameters owing to Pawley refinement using TOPAS **[8]**. Estimation of the intensity

of specific peaks was also carried out.

3.4.3 Electron backscattered diffraction (EBSD)

In order to identify the deformation products during plastic deformation, specimens deformed to different levels were then observed by Electron Back-Scattered Diffraction (EBSD). The EBSD observations were operated by our co-worker P.J. Jacques (Universite´ Catholique de Louvain, Institute of Mechanics, Materials and Civil Engineering, IMAP). Prior to the EBSD observations, the samples were mechanically polished down to 1 μm using diamond paste, and then electro-polished using a solution of OP-S and H_2O_2. EBSD scans were performed using a field emission gun scanning electron microscope operating at 10, 15 or 20 kV, with step sizes ranging from 0.1 to 0.05 μm.

3.4.4 Transmission electron microscopy (TEM)

In this work, a JEOL 2000FXTEM operating at 200 kV was used to carry out conventional microstructural analysis. A JEOL 3010 TEM operated at 300 kV was used to perform Automatic crystal orientation measurements (ACOM) with an ASTAR system **[9]**. The ACOM scanning was applied in Nano-beam diffraction (NBD) mode with a step size of 20 nm. The NBD patterns of each pixel were positioned and recordedin real time. The orientation/phase identification was then performed off-line by diffraction pattern matching algorithm to reconstruct the deformation microstructure.

Regarding the preparation of TEM samples, the twin jet electrolytic thinning technique was applied based on an electro chemical dissolution. The TEM samples were made from 3mm diameter discs punched out of thin foils of the alloy. Then, the selected samples were polished by mechanical polishing using 800 and 1200 grit SiC papers to attain a final thickness of approximate 20 μm. The prepared samples were finally electro-polished by twin jet electrolytic thinning device using a solution of

53.5% CH_3OH, 33% $C_4H_{10}O$, 11.5% $HClO_4$ and 2% HCl, held at about -10°C. After electro-polishing, the surface of the samples was shiny, and a hole was in in the center of the sample to obtain the observed region. Finally, the electro-polished samples were cleaned by CH_3OH solution for 3~5min.

3.5 Mechanical Testing Tools

3.5.1 Vickers hardness Testing

The Vickers hardness test is used for measuring the hardness of materials by producing a small indent with a known load and then measuring the size of the indent **[10]**. In our work, the Vickers hardness measurements were carried out on a Diamond Vickers Hardness tester (MHT-200), at an indentation load of 50gf and a dwell time of 5s. Hardness measurements were applied on the polished surface of the specimen. At least ten indentations were taken for each specimen and the average values were calculated.

3.5.2 Tensile Testing

For evaluating the tensile behavior for the designed alloys, the uni-axial tensile tests and cyclic loading-unloading tests were carried out using an INSTRON 5966 machine at a constant strain rate of $10^{-3}s^{-1}$ at room temperature. Figure 3.7a shows the photograph of the tensile test machine. The dimension of tensile specimen was also presented in Figure 3.7b. The cyclic loading-unloading tests were carried out by the increments of 5% strain until fracture. An extensometer was used to precisely measure the deformation of the specimens. All tensile tests were performed along the rolling direction.

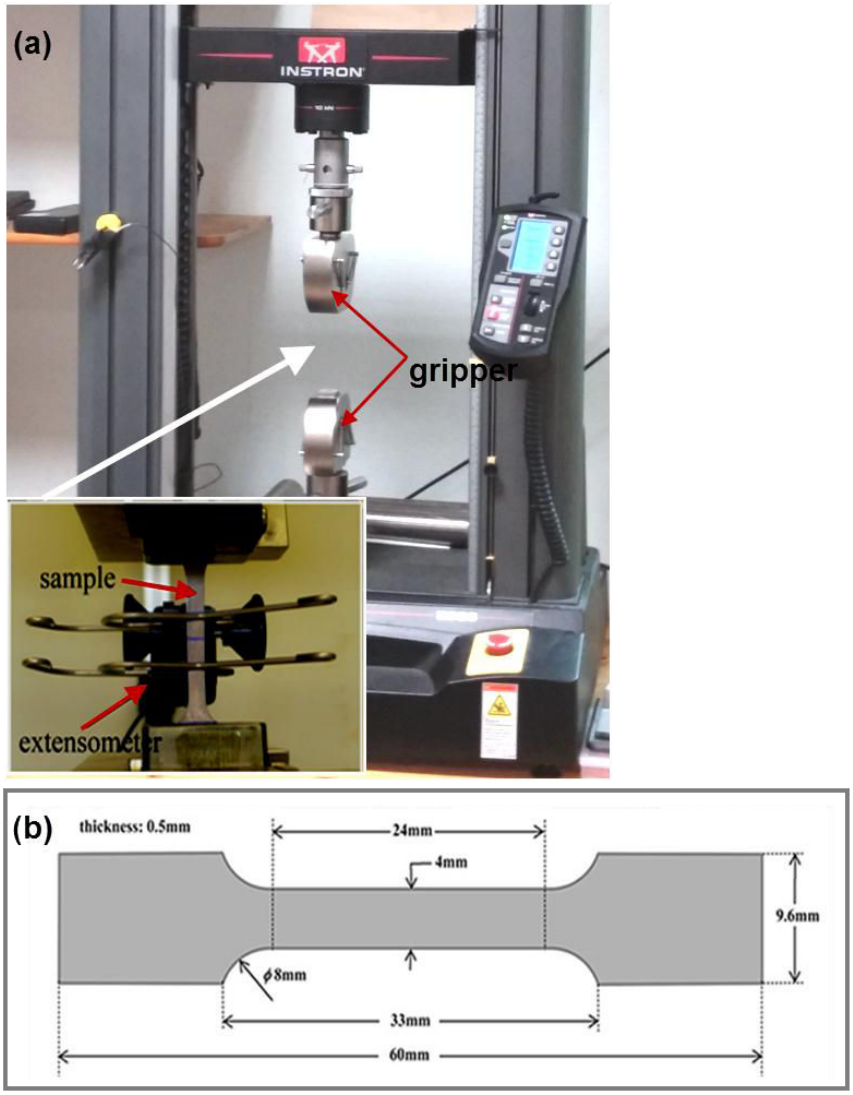

Figure 3.7 (a) the tensile test device (INSTRON 5966) and (b) the dimension of the sample for testing.

References:

[1] C. Leyens, M. Peters, Titanium and titanium alloys, Wiley Online Library, 2003.
[2] O. Karasevskaya, O. Ivasishin, S. Semiatin, Y.V. Matviychuk, Mater. Sci. Eng. A 354 (2003) 121-132.
[3] O. Ivasishin, P. Markovsky, Y.V. Matviychuk, S. Semiatin, C. Ward, S. Fox, J. Alloy. Compd. 457 (2008) 296-309.
[4] O.M. Ivasishin, P.E. Markovsky, S.L. Semiatin, C.H. Ward, Mater. Sci. Eng. A 405 (2005) 296-305.
[5] G. Lütjering, J.C. Williams, Titanium, Springer, 2007.

[6] S. Malinov, P. Markovsky, W. Sha, Z. Guo, J. Alloy. Compd. 314 (2001) 181-192.
[7] S. Malinov, P. Markovsky, W. Sha, J. Alloy. Compd. 333 (2002) 122-132.
[8] A. Coelho, TOPAS-Academic, Version 4.1; .
[9] A. Kobler, A. Kashiwar, H. Hahn, C. Kübel, Ultramicroscopy 128 (2013) 68-81.
[10] R.M. German, Handbook of mathematical relations in particulate materials processing, John Wiley & Sons, 2009.

Chapter 4

Mechanical behavior and microstructural evolution in metastable β Ti-12Mo titanium alloy showing combined TRIP/TWIP effects

4.1 Introduction

During the past few decades, the interest for Ti-alloys has been continuously increasing due to their combination of properties such as high strength **[1-6],** low density, biocompatibility **[7-10]** and good corrosion resistance **[11, 12]**. However, both their low ductility (uniform elongation typically less than 0.20) and their lack of work-hardening when compared with steels or Co-Cr alloys **[11, 13]**, limit their use in advanced applications where superior combinations of strength and ductility are required.

A strategy dedicated to a general improvement of the mechanical properties based on TRIP/TWIP has been widely investigated in the case of steels **[14-16]**. An optimization of mechanical properties can be also achieved in Ti-based alloys, when controlling the metastability of the β matrix through its chemical composition **[4, 5, 13, 17, 18]** that strongly influences the martensitic start (Ms) temperature **[5, 13, 19]** and the critical resolved shear stress (CRSS) for twinning. Indeed, it has been reported that several deformation induced phase transformations, i.e. ω phase and α'' phase precipitation, and two twinning modes, {112}<111> type and {332}<113> type, could be activated under different stress conditions (strain rate, temperature, etc.) in some specific Ti alloys **[3, 20-25]**. These mechanisms can be activated in various alloys exhibiting shape memory effect **[19]**, superelasticity **[18-20, 23, 24, 26]**

or work-hardening behaviour **[3, 4, 27, 28]**.

The design of Ti-12Mo (wt. %) alloy has been introduced in chapter 2. Tension results display that the alloy exhibits excellent mechanical performances: high tensile strength (~1000MPa), large uniform ductility (ε=0.38) and a significant work-hardening effect close to the theoretical limit **[27, 29]**. These values of strength and elongation were hardly reached before in BCC alloys. Both mechanical twinning and stress/strain induced phase transformations were observed in deformed samples, in good agreement with the theoretical predictions. However, the sequence of deformation processes, involving both twinning induced plasticity (TWIP) and transformation induced plasticity (TRIP) is still unclear and needs to be investigated in more details to understand the role of the synergy between these mechanisms in the improvement of the work-hardening. As a consequence, microstructural evolutions were characterized at different strain levels, by using *in-situ* synchrotron X-ray diffraction (SXRD) and conventional X-ray diffraction (XRD), optical microscopy (OM), electron backscattered diffraction (EBSD) mapping and transmission electron microscopy (TEM) analysis. Deformation mechanisms at different deformation stages are further discussed, based on microstructural evolution evidences.

4.2 Results

4.2.1 Tensile behavior

Mechanical characterization, including the conventional and cyclic tensile tests, of the solution-treated alloys samples have been performed using tensile tests at room temperature. The uniaxial tensile loading curve of solution treated Ti-12Mo specimen is shown in Figure 4.1. The true strain/true stress curve exhibits a large uniform elongation close to 0.4 as well as a significant work-hardening rate, much larger than in the case of the conventional Ti-alloys **[30, 31]**. The corresponding

work-hardening rate (dσ/dε) also represented in Figure 4.1 illustrates a multi-stage deformation process as classically observed in microstructures exhibiting multiple plasticity phenomena **[14-16, 32]**. From elastic limit to ε=0.1, there is first a monotonic increase of the work-hardening rate that reaches a maximum value around 2000 MPa, which is close to the theoretical limit of such alloy (E/50) **[27, 29]**. Three stages of the work-hardening rate are defined in the deformation process (Figure 4.1). The work-hardening phenomenon of our investigated Ti-12Mo alloy is similar to some TRIP/TWIP steels **[14-16, 32].** Stage I corresponds to the conventional transition between the elastic and plastic regimes (the onset of plastic range). Stage II relates to a large increase of the work-hardening rate from the elastic limit to ε=0.1 (the early deformation stage). The work-hardening then decreases in Stage III (the late deformation stage). It is necessary to classify the detailed microstructural evidences of combined TRIP/TWIP effects in every evolution stages, in order to further understand the evolution of work-hardening rate.

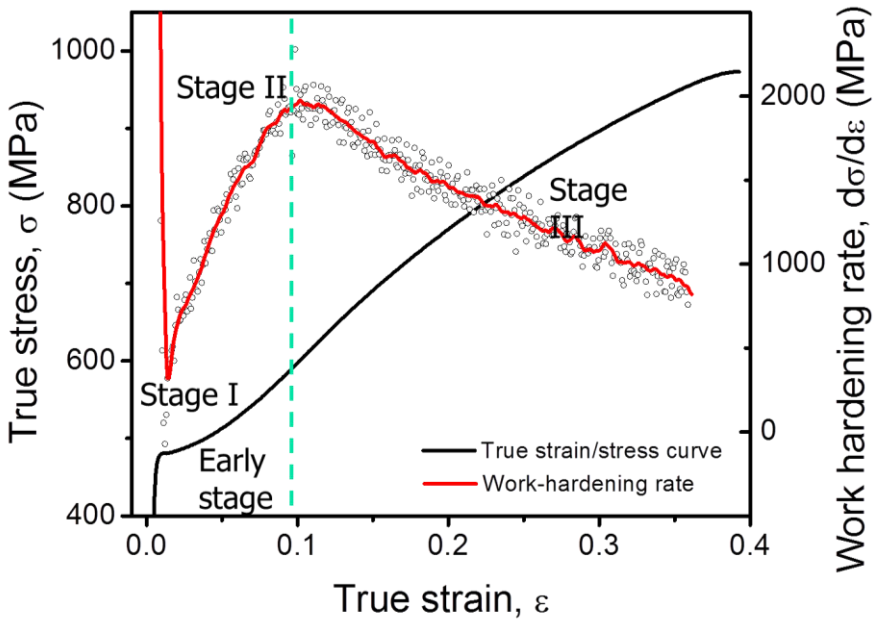

Figure 4.1 Tensile true strain/true stress curve of solution treated Ti-12Mo alloy is shown in black line. The corresponding work-hardening rate, dσ/dε, is plotted in black cycles and the smoothed curve is shown in red.

The cyclic loading-unloading tensile tests were carried out until fracture with the increments of 5% strain, in order to evaluate the reversible phase transformation (β/α") at each strain level. The stress-strain curve example of the first cycle was presented in Figure 4.2. The unloading curve exhibits a pseudo-elastic behavior, due to the reversible SIM α"→β transformation. Three types of strain were then defined to characterize the phase transformation process during unloading, namely, the elastic strain (ε_e), the recovered strain through α"→β phase transformation (ε_R) and the plastic strain (ε_p). The three types of strain were measured from the cyclic loading-unloading curves, plotted in Figure 4.3 versus the applied strain. Meanwhile, the apparent Young's modulus at every loading cycle was calculated and presented in Figure 4.3. It can be seen from Figure 4.3 that ε_R gradually decreases, indicating the volume fraction of the reversible SIM α" decreases when the total deformation increases. Similarly, the apparent Young's modulus also decreases with strain, from 90GPa (first loading cycle) to about 32GPa (last loading cycle). Since the shear modulus of martensite is lower than the β phase, it is thought that the decrease of Young's modulus as a function of applied strain was probably due to an increase of the residual SIM volume fraction in the β matrix.

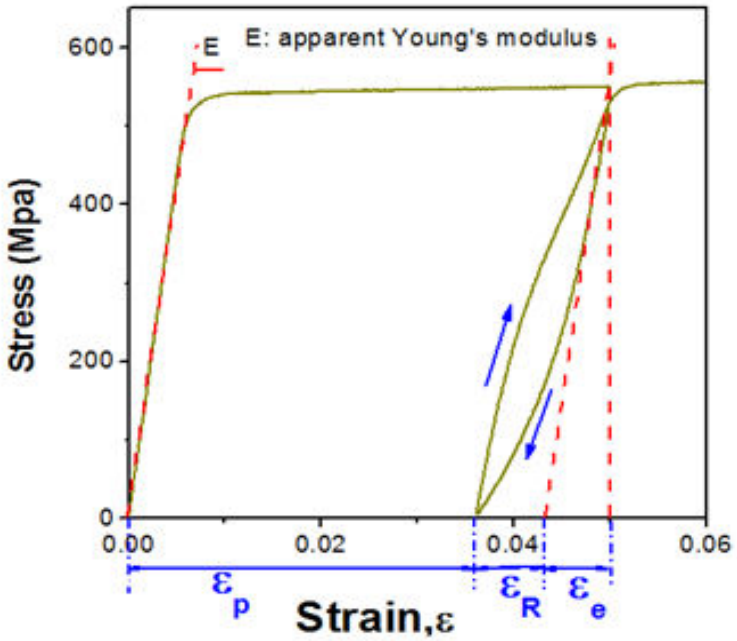

Figure 4.2 The stress-strain curve of first cyclic loading-unloading test is presented, some characteristic mechanical data such as the elastic strain (ε_e), the recovered strain via reverse transformation after discharge (ε_R), the plastic strain (ε_p) are also indicated.

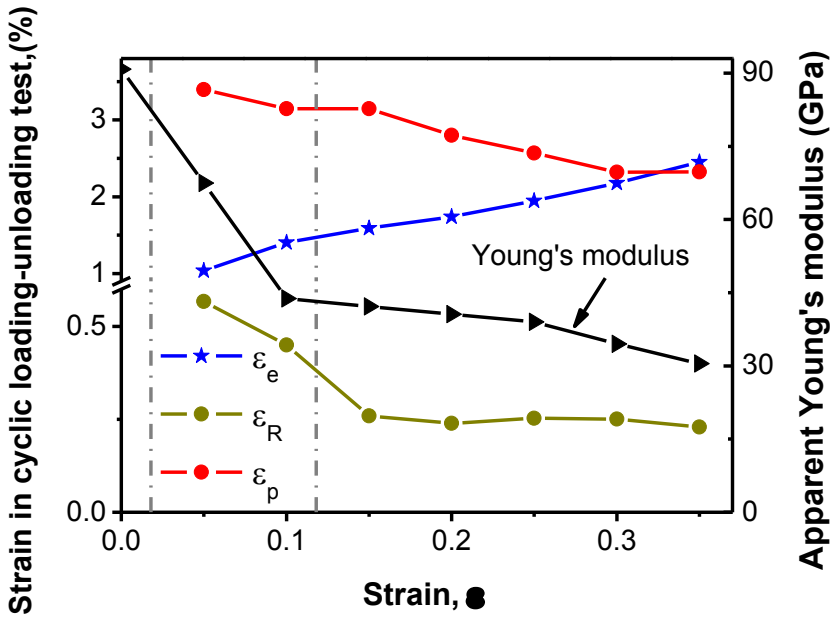

Figure 4.3 Three types of strain determined from the cyclic loading-unloading curves of ST Ti-12Mo alloy are plotted as a function of strain. The apparent Young's modulus at every loading cycle is calculated and also presented versus the strain.

4.2.2 Phase transformation characterization

In order to characterize the phase transformation during deformation procedure, two kinds of X-ray diffraction technique are used: *In-situ* synchrotron X-ray diffraction and conventional X-ray diffraction. The SXRD patterns corresponding to different strain levels at the early stage (stage I and stage II) are given in Figure 4.4. Diffraction peaks corresponding to additional deformation-induced phases can be noticed on these diffraction patterns (Figure 4.4a). Pawley refinement **[33, 34]** was applied on each SXRD pattern for identification and characterization of the phases induced upon deformation. Figure 4.4b gives an example of the refinement after unloading, where strong stress or strain-induced martensite (SIM) α'' diffraction can be clearly identified. Figure 4.4c presents the position and intensity of the major diffraction peaks of ω, α'' and β phases. As classically observed for metastable β Ti alloys, the initial ST microstructure of the present Ti-12Mo alloy exhibits some athermal ω phase together with the β matrix. The characterization of this ω phase is always

difficult by conventional XRD technique due to its size and distribution at the nano-scale. Here, the accurate SXRD scans are able to provide precious information on the evolution sequence of this ω phase in the strained bulk material. The volume fractions of the phases are directly proportional to the integrated intensity of their specific diffraction peaks. Figure 4.4d shows the evolution of the integrated intensity of the (0001)ω and (110)α'' characteristic diffraction peaks, illustrating the sequence of appearance/disappearance of the ω and α" phases. In the initial ST state, the intensity of the ω peaks is due to the quenched-in athermal ω precipitates **[3]**. At the onset of plastic yielding (ε=0.5%-0.7%), the ω intensity exhibits a sudden increase then followed by a decrease. The diffraction peaks of ω phase start to vanish after ε>0.7% when the SIM α" signature starts to increase monotonically with strain. Finally, the volume fraction of SIM α" phase reaches a maximum at about 8% strain and displays a reduction after unloading.

The conventional X-ray diffraction profiles at different deformation levels of ST specimens are presented in Figure 4.5a. The single β phase was detected on the ST sample via the conventional XRD pattern. Furthermore, minor ω peaks in β matrix are hardly detected from conventional XRD after deformation. Similar to the SXRD results at the early deformation stage, the intensity of SIM α" peak increases along with applying strain. By measuring the full width at half maximum (FWHM) of (111) α" peak at the full deformation range, the value raises monotonically with the applying strain (Figure 4.5b). A broadening effect was observed on the (111) α" peak evolution. The broadening effect is probably owing to the refinement of the SIM α" phase when deformed very heavily. And the refinement maybe result in difficulty to detect the very fine SIM α" phase through the conventional XRD technique.

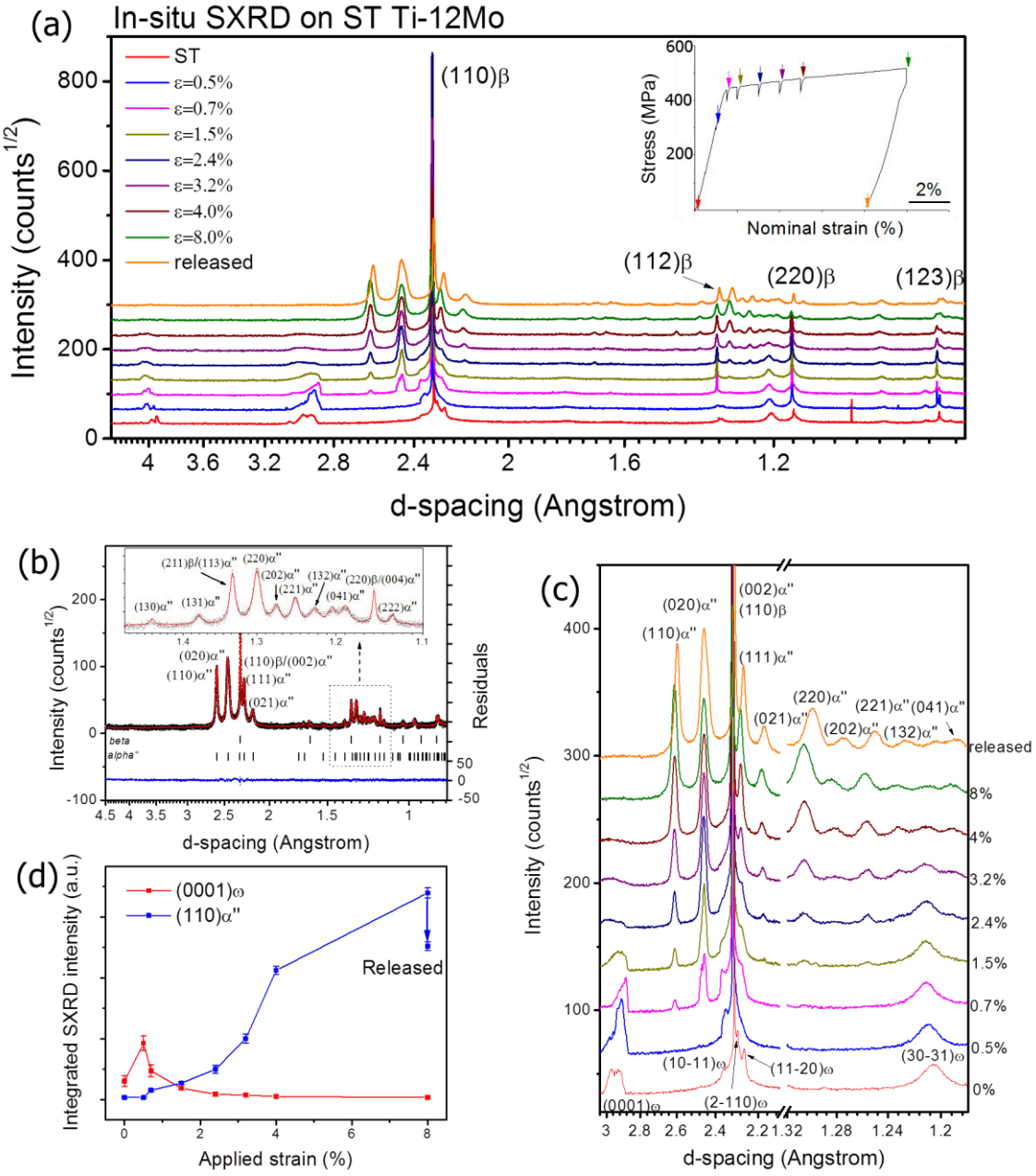

Figure 4.4 In-situ synchrotron x-ray diffraction (SXRD) results. (a) SXRD patterns corresponding to increasing deformation levels as well as before and after loading. The stress/strain curve is shown in the inset; (b) Final Pawley refinement on the SXRD profile after release from 8.0% strain; (c) The shifting of the major peaks of ω and α'' phases as a function of applied deformation; (d) The evolution of the intensity of the characteristic peaks (0001)ω and (110)α'' as a function of applied strain.

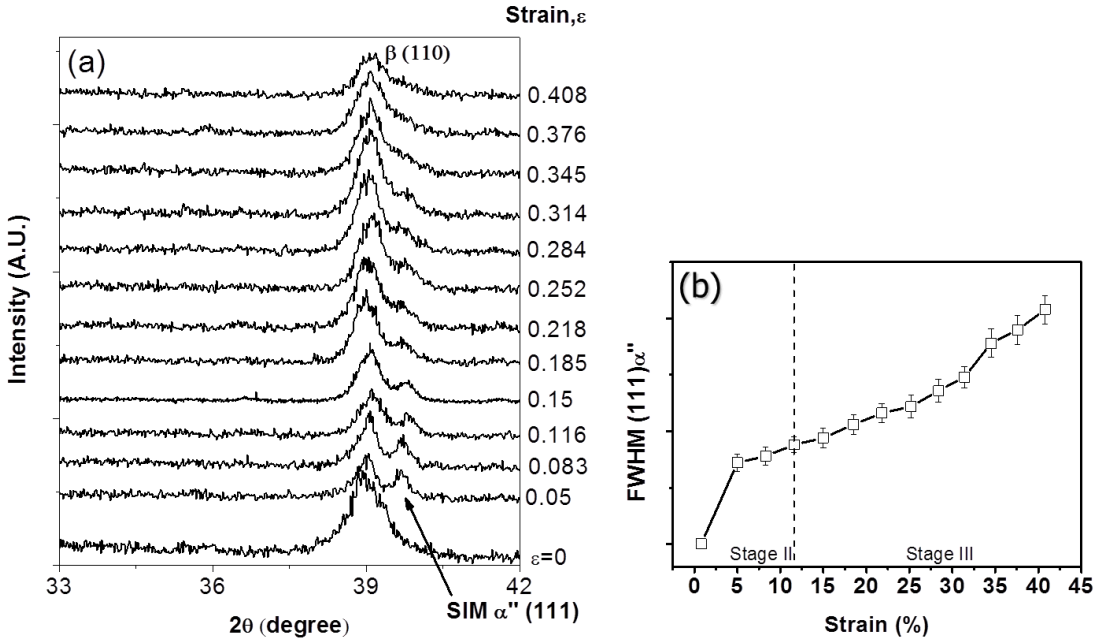

Figure 4.5 (a) X-ray diffraction profiles of the solution-treated Ti-12Mo alloy specimen at different strain levels; (b) The FWHM of (111) α'' peak as a function of strain.

4.2.3 Microstructural evolution

4.2.3.1 OM observations

Figure 4.6 shows some typical OM images at strains of 0, 0.02, 0.05, 0.15 and 0.25. At ST state (ε=0), the microstructure of Ti–12Mo alloy was constituted by equiaxed β phase with grain size of about 80 μm (Figure 4.6a). Upon tensile straining, band-like deformation products start to occur at the beginning of the plastic deformation process. The band-like deformation products has been proved to mainly consist of {332}<113> type mechanical twin and SIM α″ phase in our previous papers [27, 35]. In order to evaluate the evolution of area fraction of deformation products, several OM micrographs at each strain levels were taken from the surface of the deformed samples at the center position. The average area fractions of deformation bands at each strain levels were measured using Software ImageJ based on all of the

recorded OM images. Figure 4.7 shows the evolution of area fractions of deformation bands as a function of strain. And the work-hardening rate, dσ/dε, is also plotted in Figure 4.7.

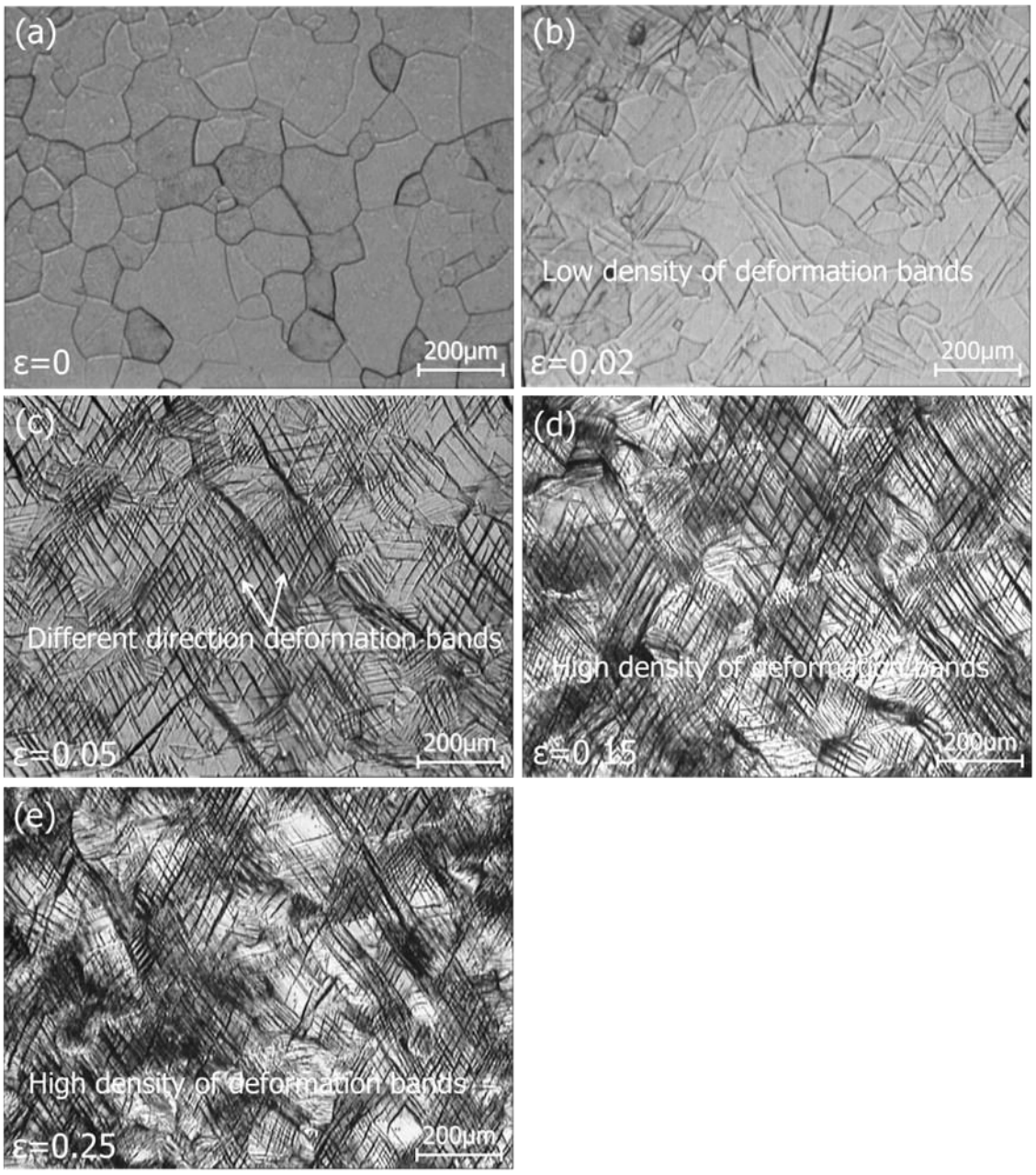

Figure 4.6 Some typical OM micrographs of the ST Ti-12Mo alloy at strains of 0, 0.02, 0.05, 0.15 and 0.25, respectively.

The area fraction of deformation bands increases rapidly before ε=0.10. Corresponding to the rapidly increase of work-hardening rate (Figure 4.7), the area

fraction of deformation bands saturated at ε=0.10~0.15, then finally reached a stable value (~60%). The saturation phenomena is similar to the early reports on TRIP materials and TWIP materials, e.g., Fe–20Mn–1.2C (wt. %) TRIP steel [36] and TWIP Ti-15Mo (wt. %) alloy [37]. However, the plastic flow at the post-saturation region shows differences to the mentioned TRIP materials and TWIP materials, i.e., a significant uniform plasticity was maintained until ε~0.35. It is thought that a respective effect of dynamic Hall-Petch effect and a composite effect (i.e secondary deformation products in the twined β matrix [35]) could be dominated one after the other during the entire plastic region, implied by the saturation of primary mechanisms at the early stage.

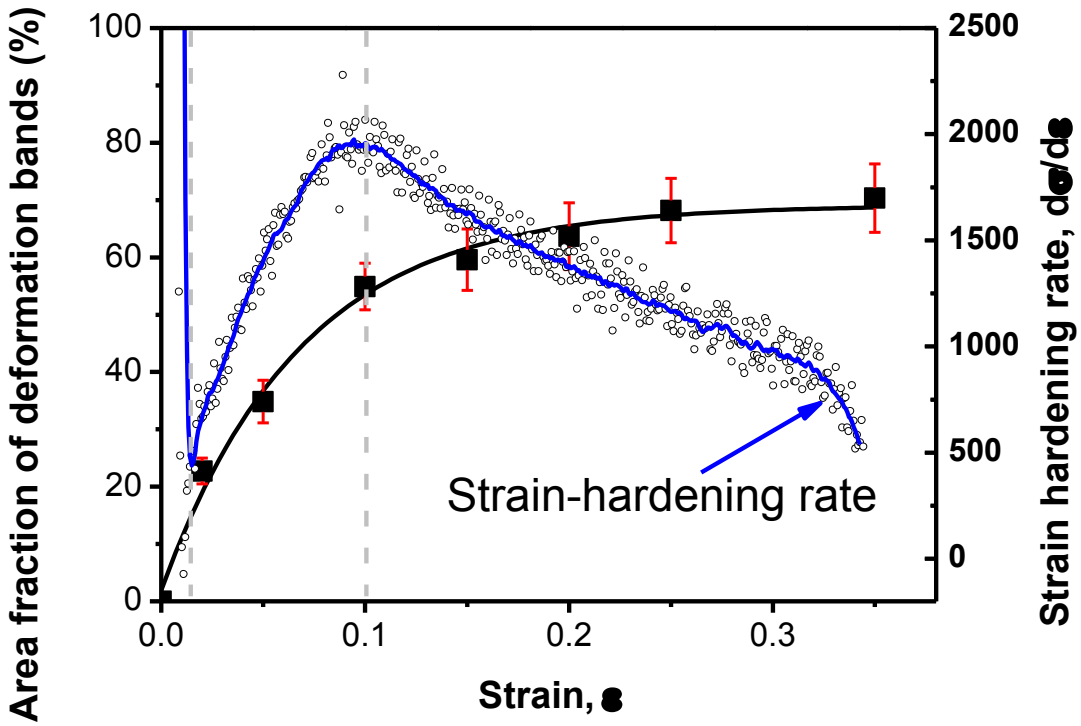

Figure 4.7 The area fraction of deformation bands is described as a function of strain in tensile. The work-hardening rate, dσ/dε, is also plotted.

4.2.3.2 EBSD analysis

EBSD mapping has been performed on specimens strained to different levels, to highlight the complex patterns. No deformation bands were observed by EBSD with its own spatial resolution for specimens strained up to ε=0.005. However, both {332}<113>twins and SIM α" plates have been observed at ε=0.01, as illustrated on Figure 4.8a-d. Figure 4.8a shows that two twinning systems are activated from the beginning of plasticity. It is worth noting that twins are not confined into one grain like in TWIP steels **[16, 38]**. Indeed, they propagate through grain boundaries to surrounding grains while undergoing a small misorientation corresponding to the one between these neighbouring grains. The width of these twins has been measured and ranges between 600 and 800 nm. In Figure 4.8b and d, band contrast and phase identification also suggest the formation of a three-variant network of SIM α" needles deeper beneath the sample surface with conventional α"/β orientation relationship, i.e. $(110)_{\alpha''}$ //$\{112\}_{\beta}$ and $[001]_{\alpha''}$//$<110>_{\beta}$, with a width ranging from 250 to 400 nm. Moreover, one can notice a small band of α" phase within the twin indicated by the open arrow in Figure 4.8b. This phenomenon of α" precipitation within twin bands has been widely observed in specimens strained to larger levels. Figure 4.8c and d illustrate the complexity of the deformation features in this alloy at a strain level as small as 0.01. SIM α" nanoscale precipitates are forming a multi-variant deformation band. Some parts of this band are also indexed as β phase, either with the matrix orientation or with a {332}<113>twin orientation. This kind of features is more and more observed for increasing strain. The indexing level decreases very rapidly with strain as illustrated by Figure 4.8e and f. Only a few twins and martensitic plates can be indexed on this figure, while most of the deformation areas, e.g. the dark clusters (black arrows) and the interiors of the coarsen bands (open arrows), are left as unidentified.

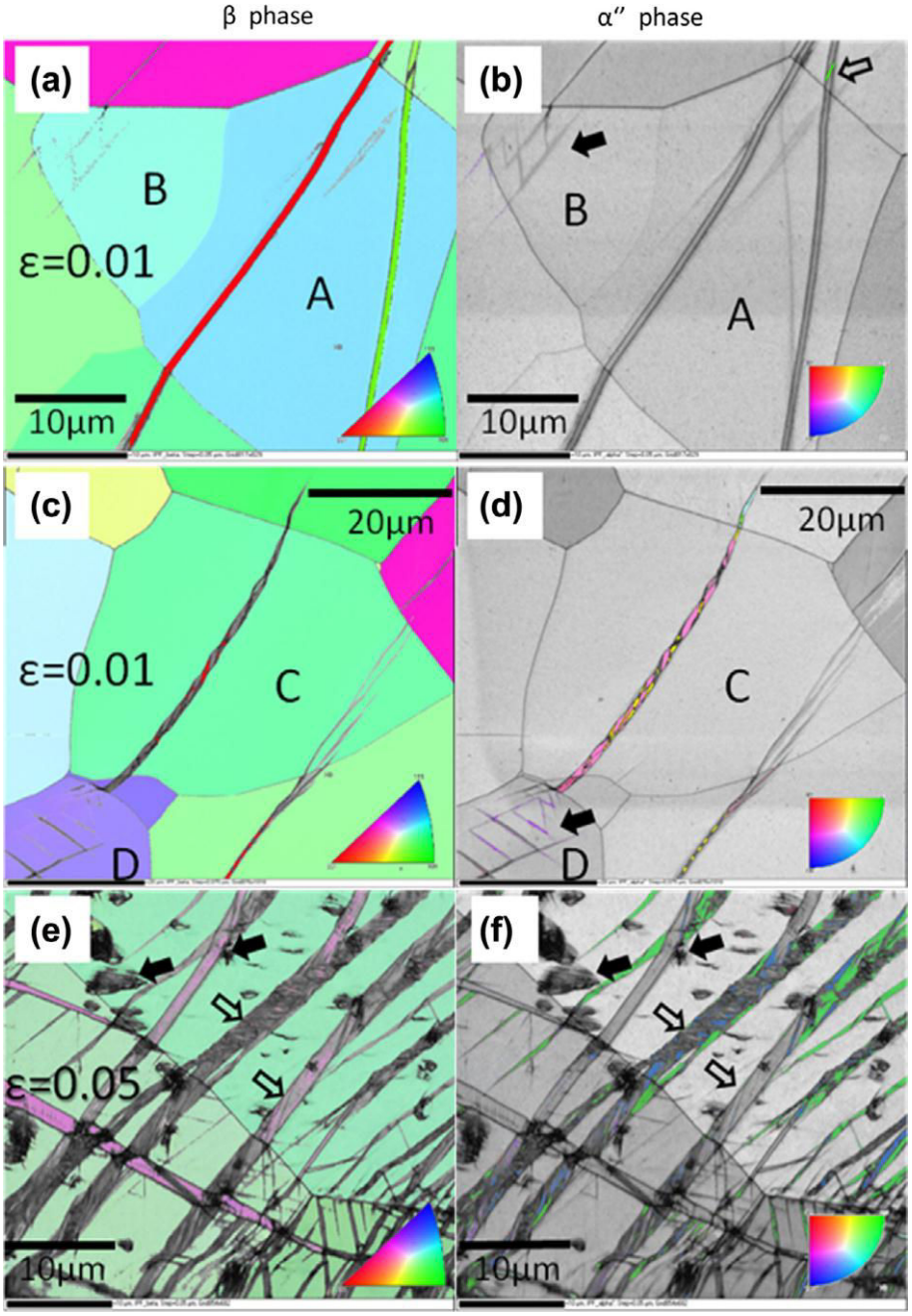

Figure 4.8 EBSD inverse pole figure maps shows complex deformation patterns at ε=1% and ε=5%. (a) Two transgranular {332}<113> twins in different orientations; (b) Needle-like α'' martensites in β matrix are indicated by black arrow, and a piece of α'' martensite inside the twin band is indicated by white arrow; (c) Several pieces of {332}<113> twins are located in complex deformation bands; (d) Two kinds of α'' martensites in different orientations are shown in the deformation bands. Needle-like α'' martensites in β matrix are indicated by black arrow; (e) Indentified {332}<113> twins in the complex deformation pattern at ε=5%; (f) Two kinds of α'' martensites in the complex deformation pattern at ε=5%. Areas of unidentified dark clusters and deformation bands with complex substructures are indicated by black arrows and white arrows respectively.

4.2.3.3 TEM investigation

Detailed microstructural investigations of the deformed samples were performed by using TEM observation at each evolution stage. At the onset of plastic deformation, the deformation-induced ω phase starts to occur. Figure 4.9 shows TEM images of the deformation-induced ω phase at ε = 0.007 and ε = 0.015. A set of parallel thin lamella induced by deformation and identified as ω can be clearly seen. The corresponding dark-field image reveals ω lamellas are in thickness of 10 to 20nm. The appearance of these bands is consistent with the synchrotron measurements of Figure 4.4. It can be observed from the diffraction patterns (inset of Figure 4.9b) that one of the two variants of ω phase is favoured, resulting in an intensity increase of the diffracting spots. The edge-on lamellas are parallel to (1-12)β plane.

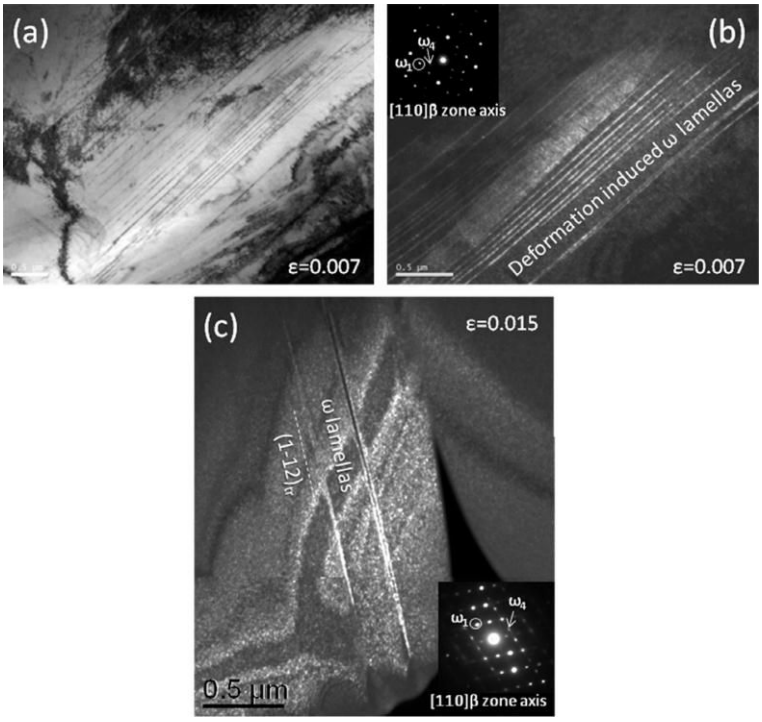

Figure 4.9 TEM images of the deformation-induced ω phase at ε=0.007 and ε=0.015. (a) Bright-field image at ε= 0.007. (b) Dark-field image of the deformation-induced ω lamellae at ε=0.007. (c) Dark-field image of the deformation-induced ω lamella at ε=1.5%. The corresponding diffraction patterns are presented in the insets of each dark-field image, showing a difference of the diffraction intensity between the two variants (ω1 and ω4 of the four variants) of ω precipitates.

The mechanical twinning bands and SIM α" were also observed simultaneously in the β matrix at the onset of plastic deformation. Figure 4.10 shows that the dark clusters of α" SIM (at ε=0.015) that were not indexed by EBSD (Figure 4.8e). Two sets of acicular plates of 200-300nm in thickness indexed as primary α” martensitic plates on the corresponding SAED pattern are identified. Furthermore, Figure 4.11 presents a representative example of the complexity of deformed samples, already at ε=0.015. Consistently with EBSD observations (Figure 4.8), the diffraction pattern along the <111>β zone axis (Figure 4.11a and Figure 4.11c) shows that two kinds of deformation products, i.e. twin and martensite, surrounded by the β matrix are present. The twinning system is identified as {332}<113> . Selecting a set of diffraction spots corresponding to α” and twin, dark field image of Figure 4.11b shows three zones of interest marked as Z1, Z2 and Z3, highlighted in Figure 4.12. Figure 4.12a and Figure 4.12b show that two different sets of α” variants can be found. They are present either within twinned β (variant α''_{V1} in zone Z1) or within the β matrix (variant α''_{V2} in zone Z2). The α''_{v2} yields conventional relationship with respect to the β matrix, i.e. (-110)α''_{V2}//(-112)β, whereas α''_{v1} accommodates crystallographically to a {332}<113> twinned β zone as (-110)α''_{V1}//$(-112)_{twin}$. For convenience, they are called hereafter primary α’’ martensite and secondary α’’ martensite, respectively. It can be noticed from this dark field image, that the {332}<113> β twin are almost completely fulfilled with the α’’ martensitic phase. In the case of zone Z3 fulfilled with a high volume fraction of stress-induced α’’ phase, Figure 4.12c and d show that the martensitic phase is actually internally twinned with the twinning plane identified as (-110)α''_{V1}, bringing about the variants α''_{V1} and α''_{V1T} as illustrated on the Figure 4.12e and f.

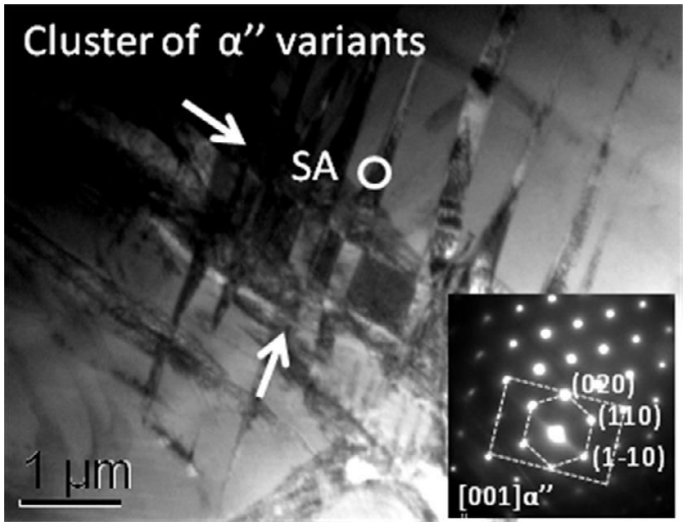

Figure 4.10 Bright-field TEM image of a deformation feature identified as a cluster of α'' variants. The corresponding SAED pattern is given in the inset.

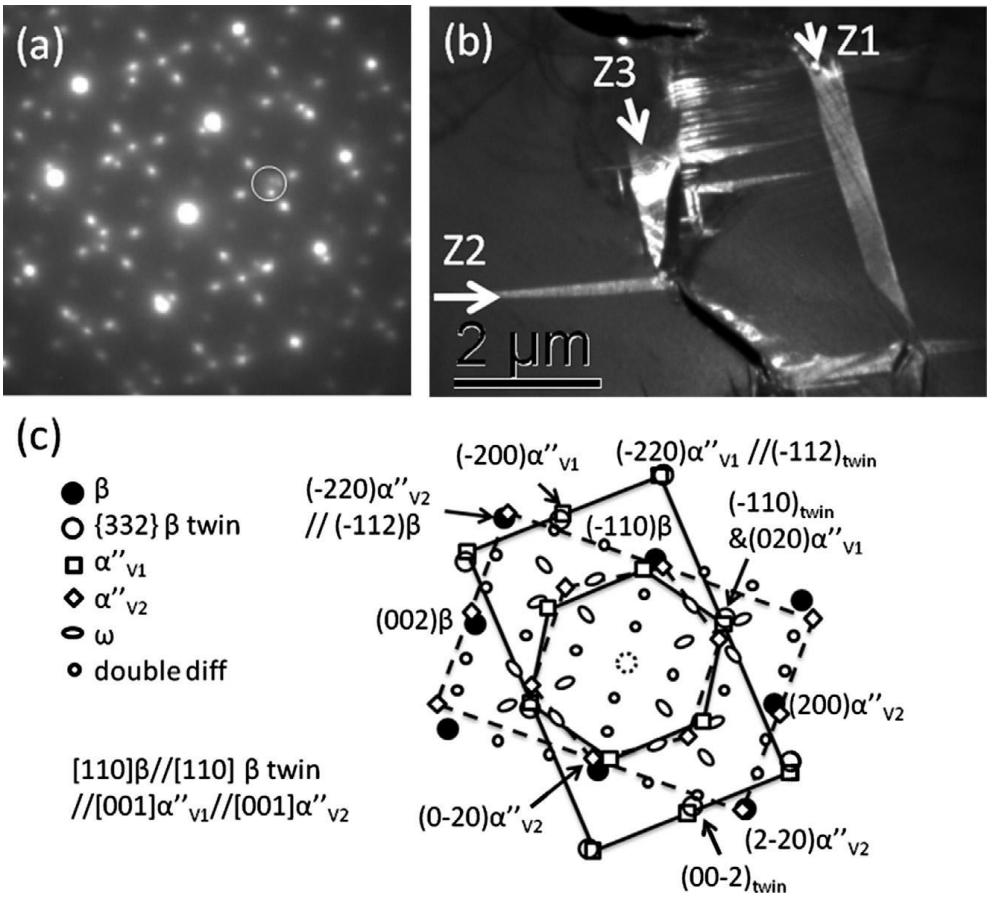

Figure 4.11 TEM images of a sample deformed to ε=0.015. (a) Diffraction pattern exhibiting multiple phases; (b) corresponding dark-field image of the deformation products by selecting the diffraction spots highlighted in (a). Three morphologies of the deformation products are revealed, labelled as Z1, Z2 and Z3. (c) Indexed diagram corresponding to {332} β twinning, ω phase and two kinds of a00 martensite, noted as α'' V1 and α'' V2.

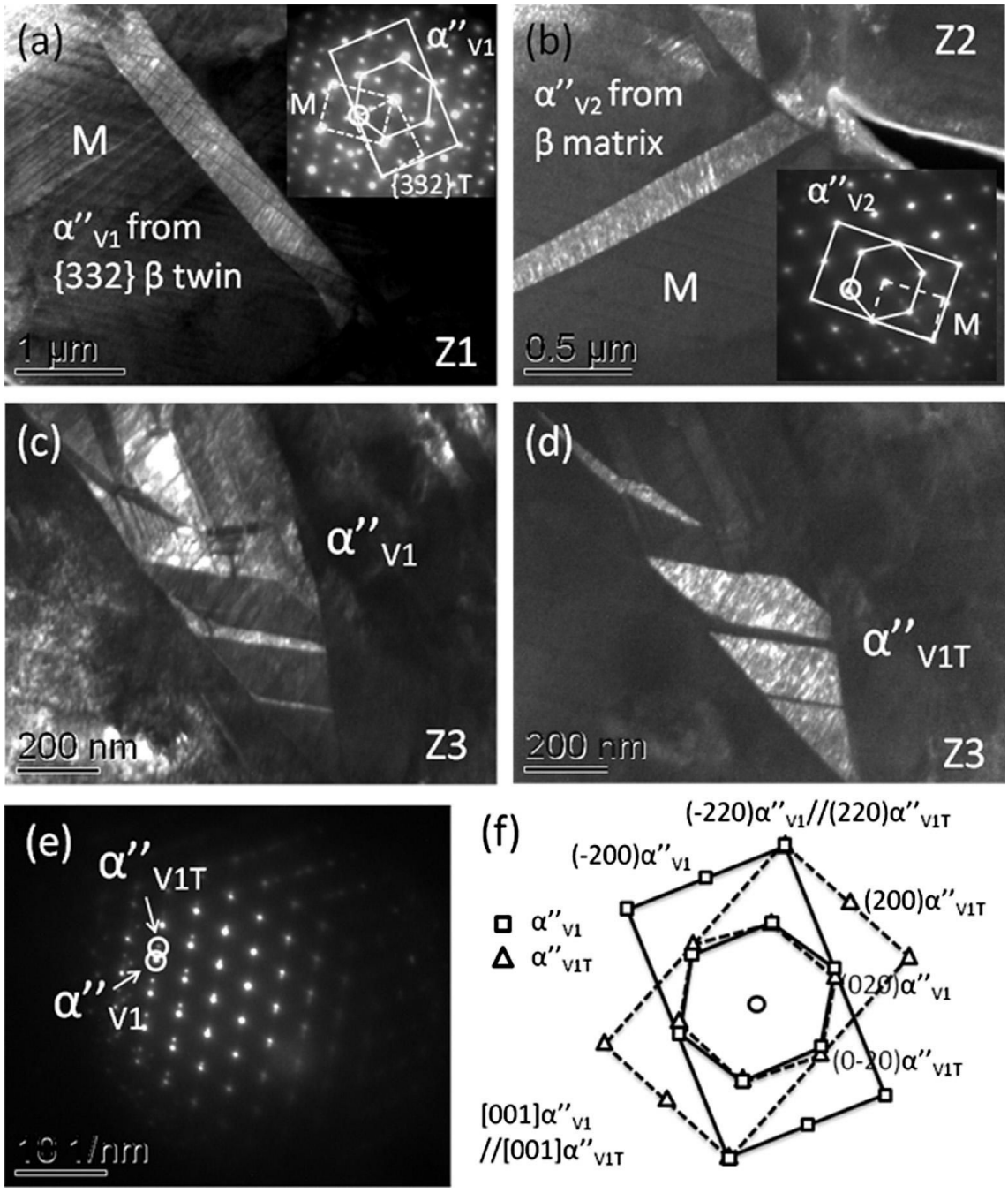

Figure 4.12 TEM images and schematic illustrations of the deformation induced α'' martensites (ε=1.5%). (a) Dark field image of two kinds of α'' martensites (ε=1.5%), labeled by α''V1 and α''V2; (b) Dark field image at the dash square in (a) shows the morphology of α''V1; (c) Dark field image at the dash square in (a) illustrates the twinned variant of α''V1, denoted α''V3; (d) The diffraction pattern of (a) shows orientation relationships among β, ω, α''V1 and α''V2; (e) The diffraction pattern of the dash square area in (a) shows a twinning relationship between α''V1 and α''V3; (f) The schematic indexation of (d); (g) The schematic indexation of (e).

The bright field image reported on Figure 4.13 displays some details of the mechanical twins found after a deformation of ε=0.005. The tip section of the {332}<113> twin band was examined for microstructural details (Figure 4.13c). The magnified image shows a set of alternated matrix and twin zones (indicated by M and T). The micrograph also reveals internal structure composed by plate-like bands of tens of nanometers in size. In order to further investigate the morphologies and interfaces of this phenomenon, the specimen was rotated by ~30° from Figure 4.13a position and tilted 45° around c-axis of the twin to superimpose the two twinning layers with $[010]_T$ zone-axis. The corresponding [010]β SAED (inset of Figure 4.13d) reveals extra spots due to the lamellar microstructure. Nano beam diffraction (NBD) analysis of the substructure was performed on/near these internal bands and shows substructures lying in layers with orientations switching from [010]β to [1-11]β. Such phenomenon can be interpreted from the NBD and the pole figure analysis (Figure 4.13f) as a multiple twinning effect in the {332}<113> twinning system, with nucleation and growth of a {332}<113> type secondary twinning system within the primary twins. The interlayer crystallographic relationship is schematically demonstrated in the superimposed pole figure along [010]/[1-11]β zone axis of Fig. Figure 4.13f. The SAED pattern of this area exhibits a double diffraction effect due to the overlapping interfaces among matrix/twin and twin/$twin_{nano}$. The corresponding dark-field image (Figure 4.13e) reveals the morphology of nano-size internal twins. It is worth noting that the {332}<113> twinning system was not the only twinning system found in this alloy since the other well-known twinning mode in BCC metals {112}<111> was also observed. However, the volume fraction of this twinning mode is very low according to the TEM analysis. This mode will not be discussed here since it may be of minor importance in the final mechanical properties of the material.

With the strain further increasing, substructures including secondary twin and secondary SIM α" occurred in the twinned β zones. In order to analyze the

substructures, an individual twin with internal sub-bands was investigated in detail, along the <110>β zone axis (Figure 4.14a). The corresponding diffraction pattern (inset of Figure 4.14a) indicates clearly SIM α" spots and ω spots. The dark-field image (Figure 4.14b) reveals that two kinds of in-plate substructures can actually be generated by the deformation inside the primary β twins, i.e. secondary α" martensite ($\alpha"_{2nd}$) and secondary twinning (T_{2nd}), respectively. The $\alpha"_{2nd}$ martensite plates are in much finer size (30-150 nm in thickness) when compared to the primary $\alpha"_{2nd}$ martensite plates. Similarly, the secondary twins display smaller size of less than 100 nm in thickness. In order to identify the crystallographic relationship between T/T_{2nd}, the sample was tilted to {133}β zone axis. Nano-beam diffraction (NBD) analysis was performed in a primary twin to identify the T/T_{2nd} orientation relationship. The corresponding NBD patterns are presented in the insets of Fig. Figure 4.14c. As shown in the schematic illustration (Figure 4.14d) by superposing the two NBD patterns, clear {332} type twinning relationship is observed with sharing (3-2-3)β plane.

At the late stage of the plastic strain process, the deformation microstructure is difficult to be analyzed, due to the large applied strain (as shown in Figure 4.15). At this strain level, none of large deformation products can be observed in a complete band-like shape by TEM. The grain structure is completely destructed, exhibiting high density of dislocations and structural defects. The observation area is fulfilled by heavily distorted zones and fine segments from the deformed twins/martensite. Figure 4.15a illustrates the fragments of a heavily deformed twin. The twin pieces are in size of several hundred nanometers. SIM α" phase shows a similar situation. Very fine α" lamellas (<100 nm) are identified in the nearby area (Figure 4.15b), resulting in the uncertainty of XRD measurements. The corresponding diffraction pattern (inset of Figure 4.15b) indicates that two α" variants are present, displaying a twinning relationship with a (110)α" common plane.

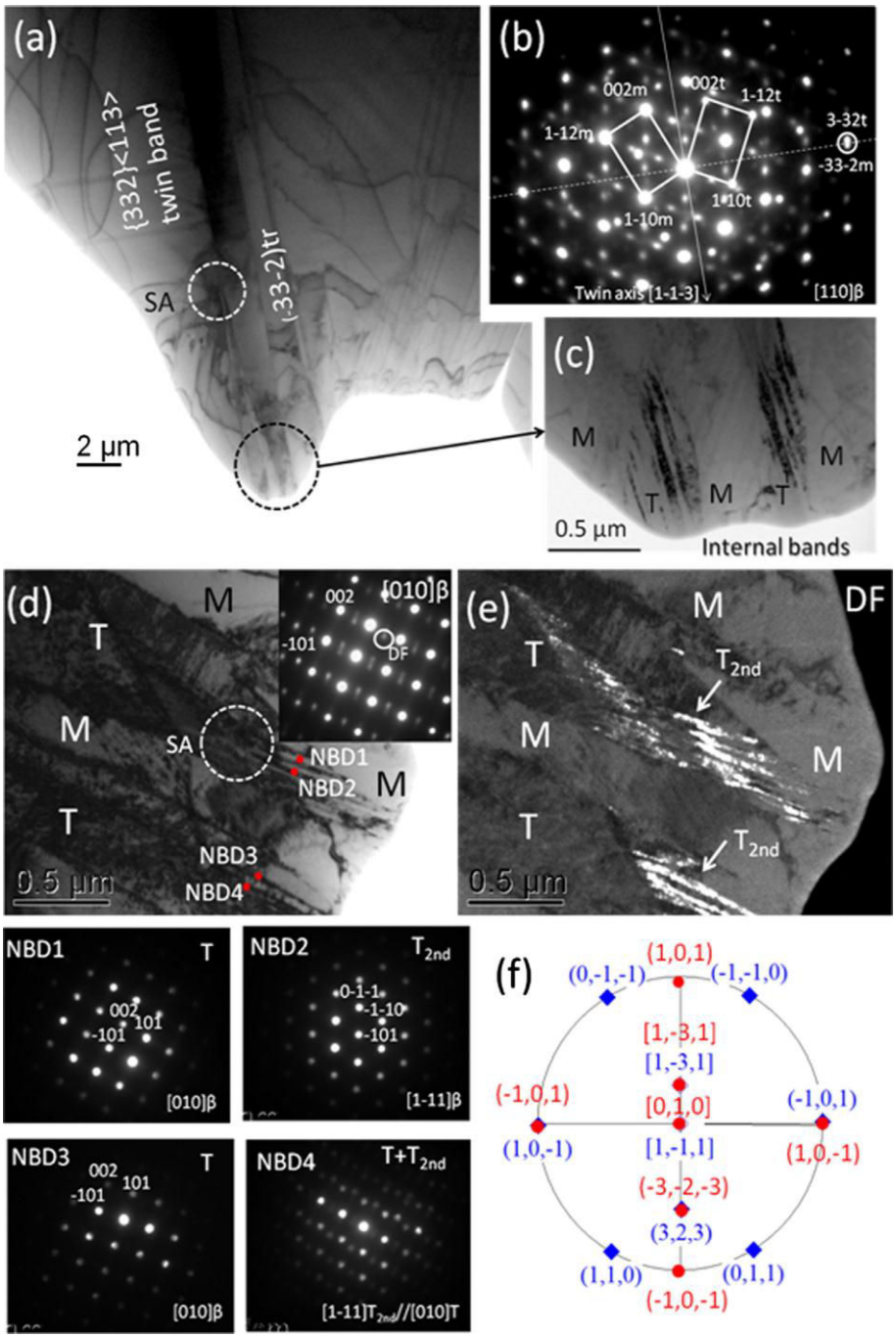

Figure 4.13 TEM images of major deformation features. (a) Bright-field image of a set of {332} <113> twin bands. (b) The corresponding SAED pattern illustrates twinning plane and twinning axis. (c) The magnified region shows the sub-structures of fine internal bands. (d) Bright-field image of the region after rotating and tilting the specimen. The corresponding SAED pattern is shown in the inset. Nanobeam diffractions (NBDs) were performed on the nanobands indicated by red dots. (e) Dark-field image in twin spot (DF) of the secondary twins marked by T2nd. (f) A schematic stereo projection figure to illustrate the crystallographic relationship of internal {332} <113> twin layers along the zone axis [010]//[1-11]β.

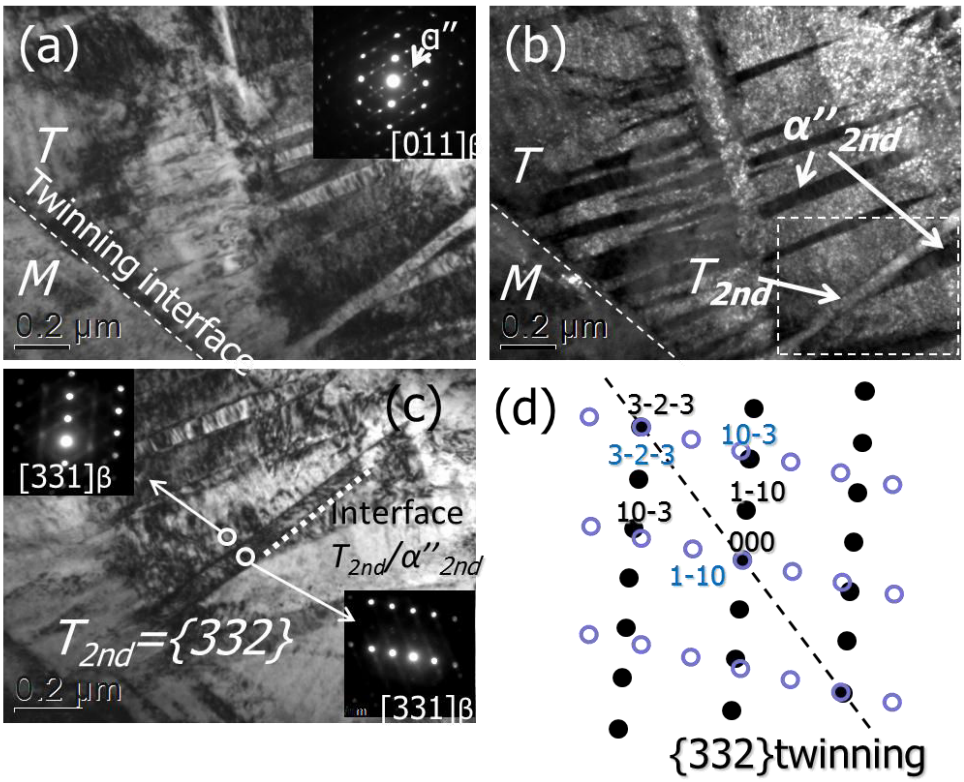

Figure 4.14 TEM images of the internal substructures in a primary twinning band. (a) Bright-field image of the primary twinning band (T) with internal plate-like substructures. The corresponding diffraction pattern of the twin (inset) indicates spots of α'' phase; (b) Dark-field image illustrates two different kinds of the internal plates, which are secondary SIM α'' (α''$_{2nd}$) and secondary mechanical twinning (T$_{2nd}$), respectively; (c) Nano-beam diffractions (NBD) indicates a {332} type twinning relationship between the primary twin (T) and secondary twin (T2nd); (d) Schematic indexation of superposed NBD patterns demonstrates the twinning relationship by sharing (3-2-3) plane.

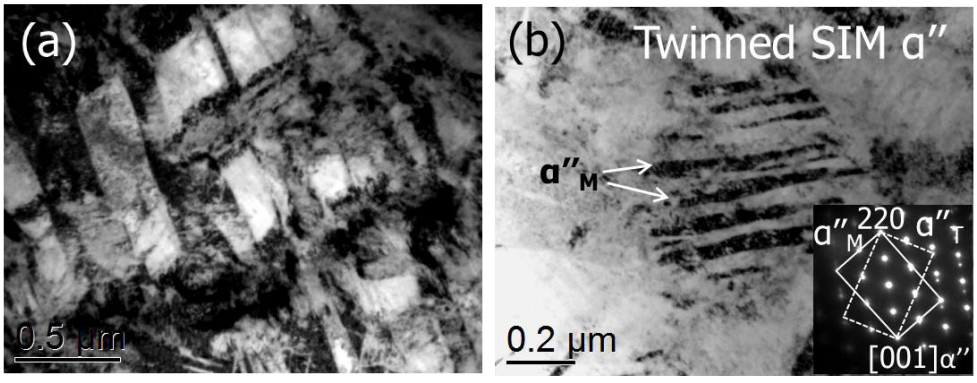

Figure 4.15 TEM images of microstructures after tensile fracture. (a) Bright-field image illustrates fine fragments of the mechanical twins; (b) Bright-field image shows thin α'' SIM plates in the deformed β matrix. The corresponding diffraction pattern is shown in the inset.

4.3 Discussion

As expected from the design strategy, the Ti-12Mo alloy displays a mechanical behaviour based on multiple deformation mechanisms such as TRIP and TWIP effects. Regarding the complexity of the deformation process, several characterization techniques have been used in a complementary way to identify the different mechanisms activated during straining. Three main kinds of deformation mechanisms have been shown to be activated: stress induced ω phase, SIM α'' and mechanical twinning. The conjunction of these deformation mechanisms leads to a complex evolution of the microstructure in the whole stages of deformation.

4.3.1 Deformation mechanisms

4.3.1.1 Deformation induced ω phase

As illustrated in section 1.3.2, three different ways of ω precipitation have been reported for Ti-alloys: (i) during quenching from the high temperature β range owing to a shuffling mechanism (athermal ω phase); (ii) during low temperature aging, in a process controlled by a diffusion mechanism (isothermal ω phase); (iii) during straining (deformation induced ω phase) by shear stress. **[39, 40]**. Regarding the ST Ti-12Mo material, it is worth noting that the athermal ω phase is present in the microstructure prior to any deformation. Furthermore, in-situ SXRD (Figure 4.4) reveals a slight increase of the ω volume fraction at the onset of plasticity, followed by its fast disappearance. The TEM investigation of Figure 4.9 confirmed the presence of a needle-like ω phase displaying the typical signature of a shear-induced product in the specimens strained to 0.007 and 0.015. Since athermal ω phase is already present in the microstructure prior to deformation, it is important to clarify if the increase of the ω volume fraction is actually based on nucleation of a new deformation induced ω phase or on a preferential growth of the existing athermal ω

phase. Experimental evidences of such deformation induced ω precipitation are hardly reported for Ti-alloys. However, similar observations were made on Ta based alloys after shock-induced impact deformation **[41]** and on nanocrystalline Mo based alloys **[42]** after severe plastic deformation process (high pressure torsion). These investigations revealed that, similarly to deformation twinning, the <111> shear on {112} planes may play a major role in the formation of ω phase. As a consequence, it was shown that this kind of ω phase can be formed based on a dislocation mechanism during shear deformation **[40-42]**. The atoms in different planes have to move a distance of 1⁄12[111] (layer 2), 1⁄3[111] (layer 3) and 1⁄12[111] (layer 4) in the transformation process from β phase to ω phase. Therefore, it was demonstrated that the ω phase could be generated by the glide of partial dislocations of types 1⁄3[111], 1⁄6[111] and 1⁄12[111], which are dissociated from 1⁄2[111] perfect dislocations in the BCC structure **[43]**.

The assumption of a preferential growth of the ω phase induced by an external strain, has been previously simulated by phase field modelling **[44].** The compressive or tensile stress may modify the equi-probable growth of the four variants of athermal ω phase. As a consequence, a selective growth of specific variants occurs whereas the other variants are inhibited. Both nucleation and growth mechanisms may lead to a change in the corresponding ω diffraction intensity (insets of Figure 4.15b), where ω_1 is found to be much stronger than ω_4 (diffractions of ω_2 and ω_3 are not distinguishable from the β spots). The alignment of the promoted ω variants constitutes the deformation induced ω lamellas (Figure 4.9) and results in an increase in the ω volume fraction, as observed on the SXRD (Figure 4.4d).

Concerning the subsequent evolution of ω phase volume fraction, which is observed as the strain decreased from ε=0.007 to ε=0.04, a reasonable explanation can be given, based on shearing and shuffling of the parent β lattice. The fact that ω phase rapidly disappears is probably due to a shear band mechanism. Similarly to the

work of Gysler et al. **[21]**, the ω phase destruction may be due to the intense dislocation slip in the active {112}<111>slip system. Therefore, these shear bands {112}<111>may destroy all ω particles within the strain concentrated volume.

4.3.1.2 SIM α'' transformation and mechanical twinning

It is really worth mentioning that SIM and mechanical twinning can be triggered simultaneously from the onset of plasticity in a deformed BCC alloys since very few examples have been found in the previous studies dealing with TWIP and TRIP effects. However, this situation was expected according to our design strategy of the chemical stability of the β phase and is shown to result in large improvement of both the tensile ductility and the work-hardening behaviour. It can be observed from Figs. 4.10, 4.11, 4.12 and 4.15 that a complex pattern of SIM α" phase is developed upon deformation, both in the matrix and in twins. This result is consistent with previous work reporting the mechanical activation of the α'' transformation in the range of 7% to 12% of molybdenum addition **[45]** whereas pure twinning deformation mode occurs around 14% of Mo addition **[46].** Since containing less β-stabilising Mo, the critical stress for the activation of the martensitic transformation in the present Ti-12Mo grade is smaller than in the case of previous work on Ti-14Mo. However, this critical stress is larger than the elastic limit so that no pseudo-elasticity occurs in the first loading from ST state (Fig. 4.2), but it should be noticed that a reverse transformation from α''->β occurs at unloading process (Fig. 4.5d). While the reversible SIM always causes elastic softening **[4]** in metastable β Ti-alloys, previous researches **[20, 27, 29]** suggest that the SIM activated in the plastic regime is able to increase the work-hardening rate when compared to typical β+α microstructures. In metastable β Ti alloys, the activated twinning system shifts from {112}<111> to {332}<113> when the β phase stability decreases **[4, 17, 22, 47, 48]**. For example, in a deformed Ti-14Mo single crystal **[28]**, two twinning modes were observed together.

However, {332} twins were observed in a much larger volume fraction when compared to {112} twins in that material. In the present Ti-12Mo alloy, due to the higher β instability, the transgranular {332} twins can be seen as the major twinning system, whereas {112} twins have been scarcely observed.

With the different deformation mechanisms in Ti-12Mo, i.e. dislocations glide, SIM, {332} twinning and {112} twinning, an "orientation factor", similar to the well known "Schmid factor", may play a critical parameter for the determination of the resolved shear stress for each deformation mechanism **[49]**. The preferential activation of a specific deformation mechanism in different β grains depends on the crystallographic orientation with respect to the applied shear stress. It is indeed illustrated on the EBSD maps of Figure 4.8a-d, where twinning is favoured in grain A while SIM is favoured in grains B and D and both deformation mechanisms are activated in grain C. Furthermore, in-plate substructure composed by SIM and twin is present in grain C, suggesting that the twinned β zones exhibit a modified orientation factor when compared to the β matrix. These twinned zones are then subsequently submitted to their own deformation pathway in which secondary deformation products are favoured. Furthermore, the transformed volume fraction from β Twins to secondary SIM α'' is much higher (Fig. 4.8d) than that in grain D (favoured in SIM). Similarly, secondary twinning can also be activated in the primary twins (Figure 4.13 and 4.14), depending on the modified orientation factor of the secondary twinning plane in the primary twins. This confinement behaviour suggests a size effect in the nucleation and growth of the deformation products in Ti-12Mo. Depending on the orientation factors of the twinned zones, two configurations can occur: secondary SIM and secondary twinning. These two configurations have been observed by EBSD and TEM (Section 4.3.3.3). However, the complexity of the deformation microstructure is far beyond this investigation of the early stages of plasticity, more efforts will be made for further understanding of the material.

4.3.2 Activation of deformation mechanism during three stage work-hardening process

According to the above microstructural characterization of every evolution stage, the primary deformation mechanisms are activated in the β matrix, i.e. deformation-induced ω, primary SIM α" and primary mechanical twining. And then the secondary deformation mechanisms are shown to be triggered at the twinned β zones, i.e. secondary SIM α" and secondary mechanical twining. They are a competing process among the deformation mechanisms. The deformation microstructural features are summarized in Table 4.1. A schematic representation of the activation of deformation mechanism is given in Figure 4.16, illustrating the microstructural evolution from the initial ST matrix to the deformed state in the whole deformation stages. The initial β matrix after the ST process is composed by textured recrystallized β grains with quenched-in athermal ω phase. The ω phase is the first phase to appear within the β matrix strained in tension. These ω precipitates are first promoted and then gradually disappear during subsequent straining as shown both by synchrotron diffraction (Figure 4.4). In the meantime, primary deformation mechanisms are activated simultaneously, exhibiting a state with the combination of plate-like {332}<113> twins and needle-like SIM α'' precipitates. The volume fraction of both primary deformation products increases with strain. The twinning mechanism is shown to dominate the primary deformation regime by forming a transgranular network of twin bands in the β grains. The network of twins is formed at a larger scale than that of the SIM α'' assembles (Fig. 4 and 6). After the formation of β twins, secondary deformation mechanisms are triggered in the twinned β zones. It is thought that the activation of the secondary mechanisms is actually regulated by locally modified orientation factors and probably by size factor in the twinned β zones. As observed in the deformed twins, two configurations are

found with the activation of either a secondary twinning system or a secondary SIM precipitation. It should be noticed that the secondary deformation mechanisms are very active in every twinned zone observed in this investigation. This situation could probably due to the size effect of the twinned zone, which promotes the nucleation and growth of the secondary products. However, the situation seems in contradiction to some previous reports **[50-52]**. The respective effect of orientation factor and size factor remains unclear regarding the secondary mechanisms in twinned β zones.

Table 4.1 Microstructural features for Ti-12Mo alloy during uniform plastic deformation

	Uniform plastic deformation region	Major phases	Major deformation microstructural features
ST	0	$\beta+\omega_{ath}$	N/A
Stage I	0.007-0.018	$\beta+\omega_{ath}+\omega_{SI}$	Planar dislocation slip and lamellar ω_{SI}
Stage II	0.018-0.118	$\beta+\alpha''_{SIM}$	Primary mechanical twin and primary SIM α"
Stage III	0.118-0.38	$\beta+\alpha''_{SIM}$	Secondary mechanical twin and secondary SIM α"

ω_{ath}: athermal ω phase; ω_{SI}: Stress induced β->ω transformation; α''_{SIM}: SIM α"

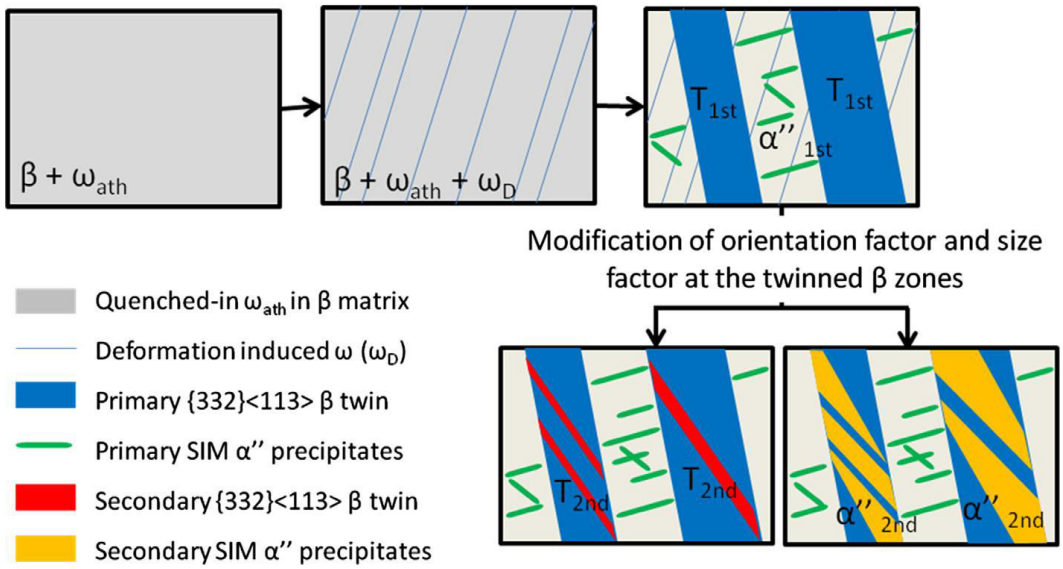

Figure 4.16 Schematic illustration of the evolution of the microstructure of the Ti–12Mo alloy when deformed in tension. The activation sequence of different deformation mechanisms is shown from the ST state to the early deformation stages (Stages I and II), i.e. deformation-induced ω phase, mechanical twinning and SIM a". The secondary deformation twins and SIM α" phase are denoted with subscript "2nd".

At the onset of plastic deformation, planar dislocation slip and plate-like ω structure are the dominant deformation mechanisms. The athermal ω phase and deformation-induced ω phase can be formed during quenching from high temperature β region and cold deformation, respectively. They have been reported in metastable Ti-V **[25]**, Ti-Mo **[3, 21, 25, 39]**, and Ti-Cr **[53]** alloys. In the present study, SXRD results (Figure 4.4) reveal that athermal ω phase forms through water-quenching in the ST samples. By applying external stress, plate-like ω phase is induced by local shearing strain (Figure 4.9). Regarding the previous researches **[41, 43]** on the relationship between ω phase and dislocation slip, it is thought that the formation of such phase is related to the initial dislocation slip on {112}β slip plane.

In the early deformation stage, the deformation products, primary mechanical twins and primary SIM, are formed in the β matrix simultaneously. The deformation products divide the original β grains into smaller volumes separated by SIM plates and twinning interfaces. As high angle grain boundaries, such interfaces are obstacle for the dislocation slips, restricting the propagation of dislocations. As a consequence, the sub-division of the β grains leads to a dynamical reduction of the mean free path for the dislocations movement, resulting in a significant work-hardening rate. At the meantime, the secondary twinning and secondary SIM (Figure 4.14) occur in the twinned β zones and continue to form in the stage III.

During the stage III, the dominating deformation mechanism changed from creating primary products in β grains to creating sub-mechanisms in the deformation products. The sub-mechanisms include secondary mechanisms happened in primary β twins and internal twinning of SIM α" phase. Such situation could be explained by the strong interactivities between the microstructure and local strain/stress configuration. The deformation microstructure created by primary twinning results in a local modification of crystallographic orientation factor, which may favor the secondary mechanisms. A confinement effect at twinned zone of nanometric

thickness is probably able to promote the activity of secondary mechanisms. Evidences can be seen from the heavy deformed microstructure (Figure 4.15a), the secondary deformation activities fully occupied the deformed area by destructing the primary twinning network, leaving very fine segments of the primary twins.

On the other hand, we still need to consider the contribution of SIM α" reaction to the applied strain during late deformation stage. It is shown in Figure 4.15 that the further deformation of a SIM α" precipitate is conducted by nanometric mechanical twinning inside the phase. The size of α" twinning lamella is about 100 nm in thickness. Such intensive twinning phenomenon is due to the further accommodation of the deformation strain after the end of primary mechanisms. Since the hardness of SIM α" phase is lower than β phase, the tensile strain is concentrated on the α" martensite. The deformation of α" martensite also affects the reversible strain (ε_R) (plotted versus applied strain in Figure 4.3). In a deformed SIM α" plate, the density of structural defects is increasing due to the local plastic strain. The dislocations blocked on the α" twinning interfaces and α"/β interfaces during plastic deformation, leading to the difficulties on the reversed transformation from α" to β **[6, 26]**. During the cyclic loading-unloading test, the weakened reversibility of the martensitic transformation causes an increase of residual SIM α" volume fraction after each cycle. At the following loading step, the residual SIM α" phase indicates a noticeable "softening effect" from the reduction of apparent Young's modulus (Figure 4.3). It is thought that the "softening effect" from deformed α" martensite may also be advantageous to gain a uniform plasticity by avoiding plastic instability. As a consequence, the work-hardening rate keeps decreasing at Stage III whereas uniform elongation is achieved until ε=0.38.

4.4 Conclusion

Combined TWIP and TRIP effects were shown to occur in the metastable β

Ti-12Mo alloy, as expected from the design strategy. The activated deformation mechanisms are phase transformations and mechanical twinning. Stress induced β->ω phase transformation was observed at the onset of plastic deformation. Upon straining, {332}<113> twinning and stress induced martensitic (SIM) β->α" transformation were both identified locally in the deformed β matrix as primary mechanisms. Secondary mechanisms such as 2nd twinning and 2nd SIM, were then observed in the primary β twins. At the end of the uniform plastic deformation, a complex deformation microstructure was observed, showing highly disturbed matrix induced by a high volume fraction of twins and occurrence of multiples secondary mechanisms. As a result, a high work-hardening rate associated to a large ductility result from the peculiar sequence of different deformation mechanisms. The features of the whole plastic deformation stage are summarized in the following aspects.

(1) Deformation induced ω precipitation was observed at the very beginning of the tensile strain, prior to SIM phase transformation and mechanical twinning. The volume fraction of ω phase reached a maximum value at ε=0.005, then gradually disappeared around ε=0.04. It is thought that the ω precipitates were dissolved by the dislocation glide on {112} slip planes.

(2) Primary mechanical twinning and primary SIM α'' precipitation were activated simultaneously at ε=0.007 in the β matrix. In the meantime, secondary mechanical twinning and secondary SIM α'' precipitation were triggered in the twinned β zones. The activation of such in-plate phenomena could probably be due to the modification of orientation factor and size factor in the twinned zones.

(3) The volume fraction of SIM α'' precipitates kept increasing during the early plastic deformation regime. However, the primary SIM α'' mechanism was much lower in volume fraction when compared to mechanical twinning. The dominating twinning system was {332}<113> in the early stage. The volume fraction of {112}<111>

twinning system was very limited.

(4) At late deformation stage, the stable plastic deformation is maintained by secondary deformation mechanisms and mechanical twinning of martensites. The microstructure was intensively refined by the secondary products and further twinning of SIM, resulting in a very complex microstructure fulfilled by fine β twins and nanometric α" twins.

References

[1] D. Avery, N. Polan, Metallurgical and Materials Transactions B 5 (1974) 1159-1162.
[2] Y.L. Hao, Z.B. Zhang, S.J. Li, R. Yang, Acta Mater. 60 (2012) 2169-2177.
[3] F. Sun, F. Prima, T. Gloriant, Mater. Sci. Eng. A 527 (2010) 4262-4269.
[4] Y.L. Hao, S.J. Li, S.Y. Sun, C.Y. Zheng, R. Yang, Acta Biomater. 3 (2007) 277-286.
[5] Y.L. Hao, S.J. Li, F. Prima, R. Yang, Scripta Mater. 67 (2012) 487-490.
[6] F. Sun, Y.L. Hao, J.Y. Zhang, F. Prima, Mater. Sci. Eng. A 528 (2011) 7811-7815.
[7] R.S. Bedi, D.E. Beving, L.P. Zanello, Y. Yan, Acta Biomater. 5 (2009) 3265-3271.
[8] H.-S. Kim, W.-Y. Kim, S.-H. Lim, Scripta Mater. 54 (2006) 887-891.
[9] M. Niinomi, D. Kuroda, K.-i. Fukunaga, M. Morinaga, Y. Kato, T. Yashiro, A. Suzuki, Mater. Sci. Eng. A 263 (1999) 193-199.
[10] D. Kuroda, M. Niinomi, M. Morinaga, Y. Kato, T. Yashiro, Mater. Sci. Eng. A 243 (1998) 244-249.
[11] J.C. Williams, E.A. Starke Jr, Acta Mater. 51 (2003) 5775-5799.
[12] S. Samuel, S. Nag, S. Nasrazadani, V. Ukirde, M. El Bouanani, A. Mohandas, K. Nguyen, R. Banerjee, J Biomed Mater Res A 94 (2010) 1251-1256.
[13] I. Weiss, S. Semiatin, Mater. Sci. Eng. A 243 (1998) 46-65.
[14] P.J. Jacques, Q. Furnémont, F. Lani, T. Pardoen, F. Delannay, Acta Mater. 55 (2007) 3681-3693.
[15] F. Lani, Q. Furnémont, T. Van Rompaey, F. Delannay, P.J. Jacques, T. Pardoen, Acta Mater. 55 (2007) 3695-3705.
[16] O. Grässel, L. Krüger, G. Frommeyer, L. Meyer, Int. J. Plasticity. 16 (2000) 1391-1409.
[17] S. Hanada, O. Izumi, Metallurgical and Materials Transactions A 18 (1987) 265-271.
[18] J.Y. Zhang, F. Sun, Y.L. Hao, N. Gozdecki, E. Lebrun, P. Vermaut, R. Portier, T. Gloriant, P. Laheurte, F. Prima, Mater. Sci. Eng. A 563 (2013) 78-85.
[19] H.Y. Kim, Y. Ikehara, J.I. Kim, H. Hosoda, S. Miyazaki, Acta Mater. 54 (2006) 2419-2429.

[20] T. Grosdidier, M.J. Philippe, Mater. Sci. Eng. A 291 (2000) 218-223.
[21] A. Gysler, G. Lutjering, V. Gerold, Acta Metall. 22 (1974) 901-909.
[22] S. Hanada, M. Ozeki, O. Izumi, Metallurgical and Materials Transactions A 16 (1985) 789-795.
[23] F. Sun, Y.L. Hao, S. Nowak, T. Gloriant, P. Laheurte, F. Prima, J. Mech. Behav. Biomed. 4 (2011) 1864-1872.
[24] R.J. Talling, R.J. Dashwood, M. Jackson, D. Dye, Acta Mater. 57 (2009) 1188-1198.
[25] S. Hanada, O. Izumi, Metallurgical and Materials Transactions A 17 (1986) 1409-1420.
[26] F. Sun, S. Nowak, T. Gloriant, P. Laheurte, A. Eberhardt, F. Prima, Scripta Mater. 63 (2010) 1053-1056.
[27] M. Marteleur, F. Sun, T. Gloriant, P. Vermaut, P.J. Jacques, F. Prima, Scripta Mater. 66 (2012) 749-752.
[28] M. Hida, E. Sukedai, C. Henmi, K. Sakaue, H. Terauchi, Acta Metall. 30 (1982) 1471-1479.
[29] U. Kocks, H. Mecking, Prog. Mater. Sci. 48 (2003) 171.
[30] M. Niinomi, Mater. Sci. Eng. A 243 (1998) 231-236.
[31] M. Niinomi, J. Mech. Behav. Biomed. 1 (2008) 30-42.
[32] K. Renard, H. Idrissi, D. Schryvers, P.J. Jacques, Scripta Mater. 66 (2012) 966-971.
[33] G. Pawley, P. Reynolds, J. Kjems, J. White, Solid State Commun. 9 (1971) 1353-1357.
[34] G. Pawley, R. Rinaldi, Acta Crystallographica Section B: Structural Crystallography and Crystal Chemistry 28 (1972) 3605-3609.
[35] F. Sun, J.Y. Zhang, M. Marteleur, T. Gloriant, P. Vermaut, D. Laillé, P. Castany, C. Curfs, P.J. Jacques, F. Prima, Acta Mater. 61 (2013) 6406-6417.
[36] K. Renard, P.J. Jacques, Mater. Sci. Eng. A 542 (2012) 8-14.
[37] X. Min, X. Chen, S. Emura, K. Tsuchiya, Scripta Mater. 69 (2013) 393-396.
[38] I. Gutierrez-Urrutia, D. Raabe, Acta Mater. 59 (2011) 6449-6462.
[39] R. Wood, Acta Metall. 11 (1963) 907-914.
[40] F. Prima, J. Debuigne, M. Boliveau, D. Ansel, J. Mater. Sci. Lett. 19 (2000) 2219-2221.
[41] L.M. Hsiung, D.H. Lassila, Acta Mater. 48 (2000) 4851-4865.
[42] G.M. Cheng, H. Yuan, W.W. Jian, W.Z. Xu, P.C. Millett, Y.T. Zhu, Scripta Mater. 68 (2013) 130-133.
[43] A. Lasalmonie, C. Chaix, Philosophical Magazine A 44 (1981) 973-981.
[44] B. Tang, Y.W. Cui, H. Kou, H. Chang, J. Li, L. Zhou, Comp. Mater. Sci. 61 (2012) 76-82.
[45] R. Davis, H. Flower, D. West, J. Mater. Sci. 14 (1979) 712-722.
[46] Y. Takemoto, M. Hida, Scripta Metallurgica;(United States) 25 (1991).
[47] M. Besse, P. Castany, T. Gloriant, Acta Mater. 59 (2011) 5982-5988.
[48] T. Grosdidier, C. Roubaud, M.-J. Philippe, Y. Combres, Scripta Mater. 36 (1997)

21-28.
[49] E. Bertrand, P. Castany, I. Péron, T. Gloriant, Scripta Mater. 64 (2011) 1110-1113.
[50] Q. Yu, Z.W. Shan, J. Li, X. Huang, L. Xiao, J. Sun, E. Ma, Nature 463 (2010) 335-338.
[51] F. Gil, J. Manero, J. Planell, J. Mater. Sci. 30 (1995) 2526-2530.
[52] Y. Aikawa, T. Terai, T. Kakeshita, Journal of Physics: Conference Series, IOP Publishing, 2009, pp. 012057.
[53] S. Hanada, O. Izumi, J. Mater. Sci. 21 (1986) 4131-4139.

Chapter 5

Microstructural characterization and mechanical behavior of Ti-12Mo alloy subjected to low temperature aging treatment

5.1 Introduction

It has been shown in previous chapter that Ti-12Mo (wt. %) alloy exhibits peculiar mechanical properties, due to combined TWIP and TRIP effects. As observed the TRIP/TWIP properties are originally based on the β phase stability. In order to further investigate the relation between the β stability and TRIP/TWIP effects, low temperature aging (LTA) has been performed on Ti-12Mo alloy. As already hypothetized the ω phase may play a central role in the nucleation mechanism of twins. The strategy adopted here is to manipulate the ω phase transformation in the β matrix to improve the mechanical performance without excessive modification of β matrix chemical composition. In other words, the question adressed here is to know if it is possible to obtain significant improvement of the initial mechanical properties (yield strength for example) while keeping the initial TRIP/TWIP effects, for Ti-12Mo alloy after LTA treatments.

It has been reported by many researches **[1-3]** that the mechanical performances of metastable β alloys can be optimized through various thermo-mechanical strategies. However, the designed strengthening strategies for materials with peculiar, i.e. shape memory effects (SME), superelasticity and TRIP/TWIP effects have to be performed while avoiding extensive, modification of β phase stability (i.e. chemical composition) for a conservation of deformation mechanisms. In metastable β Ti alloys, the instability of β matrix is critical to the

activation of stress induced phase transformations and mechanical twinning **[4-6]**. As a result, a possible approach could be based on a short-time thermal treatment strategy at relatively low temperatures. This strategy has been developed with success to optimize the mechanical performances of superelastic alloys **[7]**. From low temperature aging (LTA) in the ω phase precipitation range, nanostructuration from β→ω transitions is expected owing to the precise control on treatment parameters. It is well-known that dispersion strengthening due to nano-sized precipitates in parent matrix is an effective way to improve the mechanical properties of materials **[3, 8-11]**. The strengthening effect via nanostructuration depends on microstructural factors, i.e. volume fraction, size, morphology and distribution of precipitates **[12]**. However, the mechanical properties of β Ti-alloys are changed drastically by the precipitation of the ω phase **[8]** after aging for long time. Generally, the large increase in yielding stress is accompanied by a drastic reduction in ductility **[8, 13]**. As a consequence, in order to reach a good balance regarding the mechanical properties, we propose here to use a low temperature aging treatment combined with very short treatment times, trying to keep the original combination of deformation mechanisms for ductility but with increased yield strength.

Therefore, this part of the work aims at investigating the influence of short time LTA treatments on tensile deformation behavior and the corresponding microstructure evolution. Thermal treatments have been performed in air furnace for 60s and 600s respectively in a [110°C- 260°C] temperature range and all samples have been subsequently water quenched. Electrical resistivity measurement (ERM) was carried out, since the technique is very sensitive to minor constitutional changes produced by thermal treatment, i.e. the athermal or isothermal nano phase transformation sequences in our case **[14]**. The true stress-strain curves of LTA specimens were obtained by uni-axial tensile tests. Phase constitutions and microstructural evolutions, before and after deformation, were observed by using X-ray diffraction (XRD) and transmission electron microscopy (TEM) analysis. The key

factors on deformation mechanism activations as a function of LTA treatments are discussed based on the experimental evidences.

5.2 Experimental results

5.2.1 Investigation of Ti-12Mo mechanical behavior after LTA treatment

The tensile behavior of aged specimens have been performed by uniaxial tensile tests at room temperature. The true stress (σ)-strain (ε) curves of the specimens are plotted in Figure 5.1. The yield strength (YS), ultimate tensile strength (UTS) and total elongation at fracture, determined from the true strain/stress curves, are summarized in Table 5.1. Meanwhile, the Vickers hardness, as a basic mechanical property of a material, are measured and reported in table 5.1. For comparison, the relative mechanical properties of as-quenched specimen were also tested and shown in table 5.1.

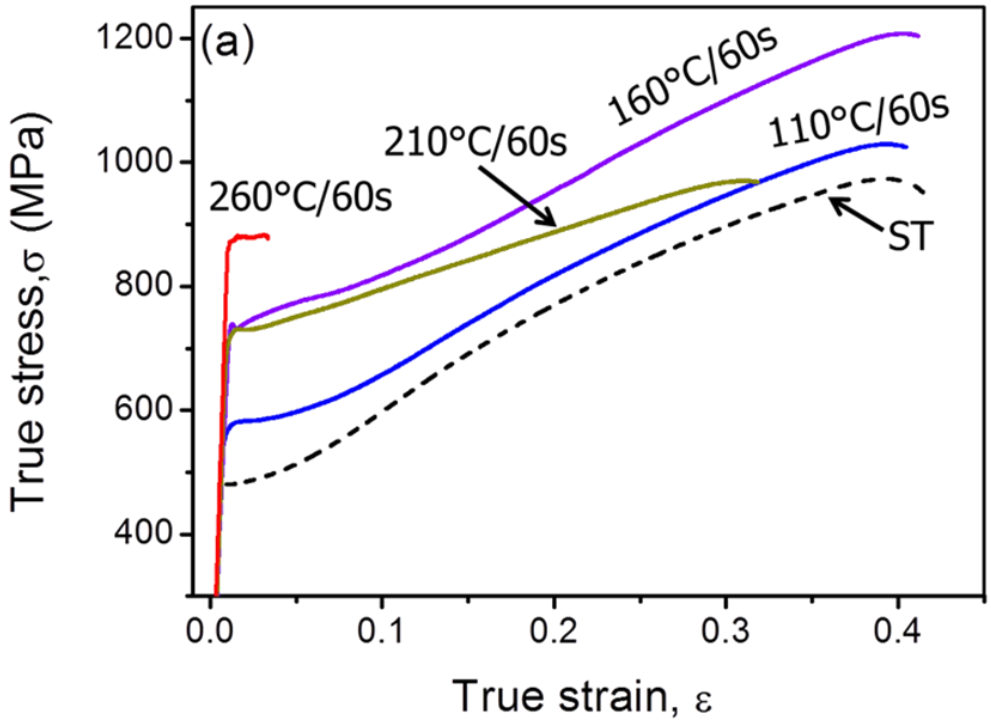

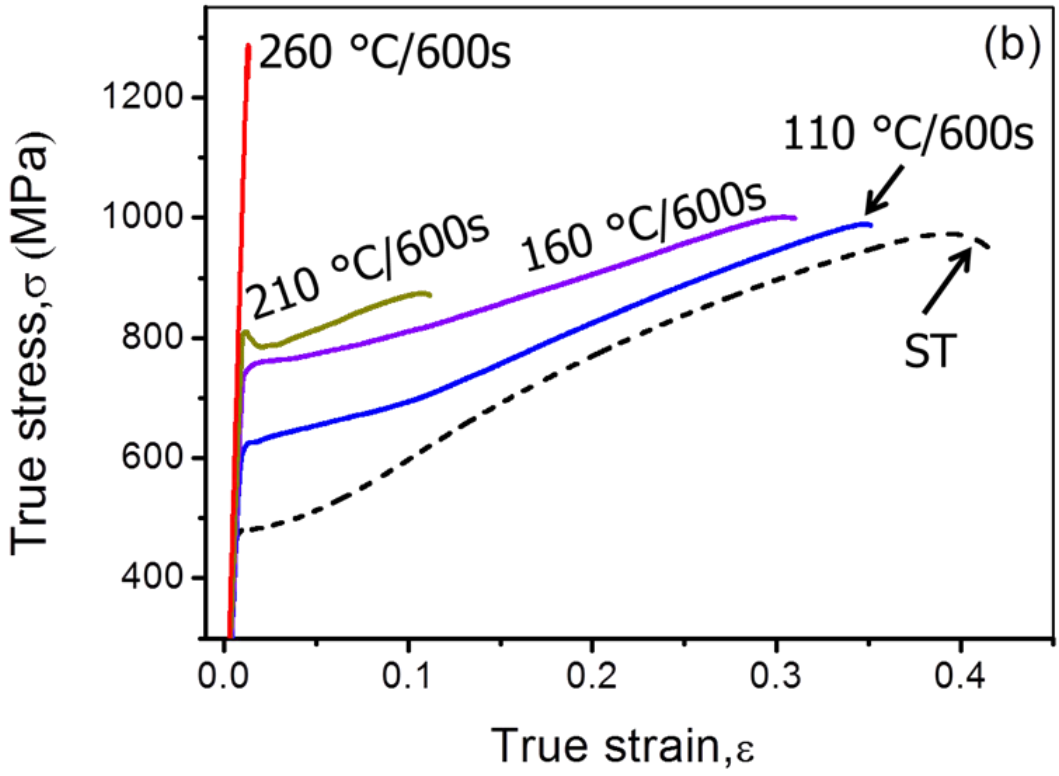

Figure 5.1 Tensile performances of the ST specimen and LTA specimens, (a) true strain – true stress curves of the specimens at ST state and after 60s LTA treatments, (b) specimens at ST state and after 600s LTA treatments.

In Figure 5.1a, the tensile curves of LTA for 60s are plotted with the ST curve as a reference. It can be seen that the tensile strengths of all the LTA specimens were significantly improved. Here, the LTA110^{o}C and 160^{o}C specimens show interesting features. Both the uniform plasticity range and work-hardening behavior are kept from the ST state without visible detrimental effects after LTA treatments. The tensile strength is the only increased property as a function of LTA temperatures up to 160^{o}C. It can be observed that, a LTA 260^{o}C sample, the yielding stress is strongly increased, however, a drastic ductility loss to ε=0.033 is noticed. Results of LTA treatments for longer duration of 600s are shown in Figure 5.1b. Similarly, the yielding stress increases as a function of LTA temperature increasing. However, the ductility is also dropping with increasing temperature. After LTA 260^{o}C for 600s, the tensile strength reaches around 1300MPa but is accompanied with a total embritlement and no plastic deformation is still visible. The Vickers hardness of the LTA samples increases

with the LTA temperature increasing. And the Vickers hardness of the LTA samples for a 600s thermal treatment duration is always superior than those treated for 60s.

Table 5.1 Tensile properties and Vickers hardness of the heat-treated specimens for Ti-12Mo alloy.

Heat treatment (Temperature: °C)		YS (Mpa)	UTS (Mpa)	ER (%)	Hardness (HV)
As-quenched		487	980	53.5	308(±4.8)
110	60s	566	1035	52.6	327(±4.2)
	600s	616	990	42.3	333(±3.8)
160	60s	715	1210	51.5	339(±2.3)
	600s	738	1000	37.7	366(±7.0)
210	60s	712	972	41.6	352(±9.0)
	600s	769	880	12.2	385 (±5.6)
260	60s	844	880	3.4	408 (±6.1)
	600s	1255	1280	-	441(±8.0)
310	60s	1261	1262	-	464(±5.1)
	600s	1261	1248	-	451(±5.95)

A summary of the tensile performances is integrated in Figure 5.2. It can be seen from Figure 5.2a that the tensile properties display important changes around 160°C. This temperature is close to the transition temperature of isothermal ω precipitation ($T\omega_{iso}$). It is well known that the precipitation of ω_{iso} phase is critical to the mechanical behavior of metastable β Ti alloys **[8, 13, 15]**. The growth of such phase leads to significant embrittlement **[8, 16]**. The work-hardening effect of the specimens is evaluated by measuring the work-hardening strength (Δσ). The parameter is defined by:

$$\Delta\sigma_{LTA} = \sigma_{UTS} - \sigma_{YS} \quad \text{... eqn. 5.1}$$

where σ_{UTS} is ultimate tensile stress and σ_{YS} is yielding stress. By plotting Δσ versus

uniform strain of the specimens, noticeable differences on plastic deformation can be seen. An evolution route of work-hardening effect can be illustrated in Figure 5.2b as a function of uniform plasticity for different LTA parameters. The work-hardening behavior is closely related to activation of deformation mechanisms at plastic range **[17]**. Different deformation modes are triggered in sequence by increasing LTA temperature and duration.

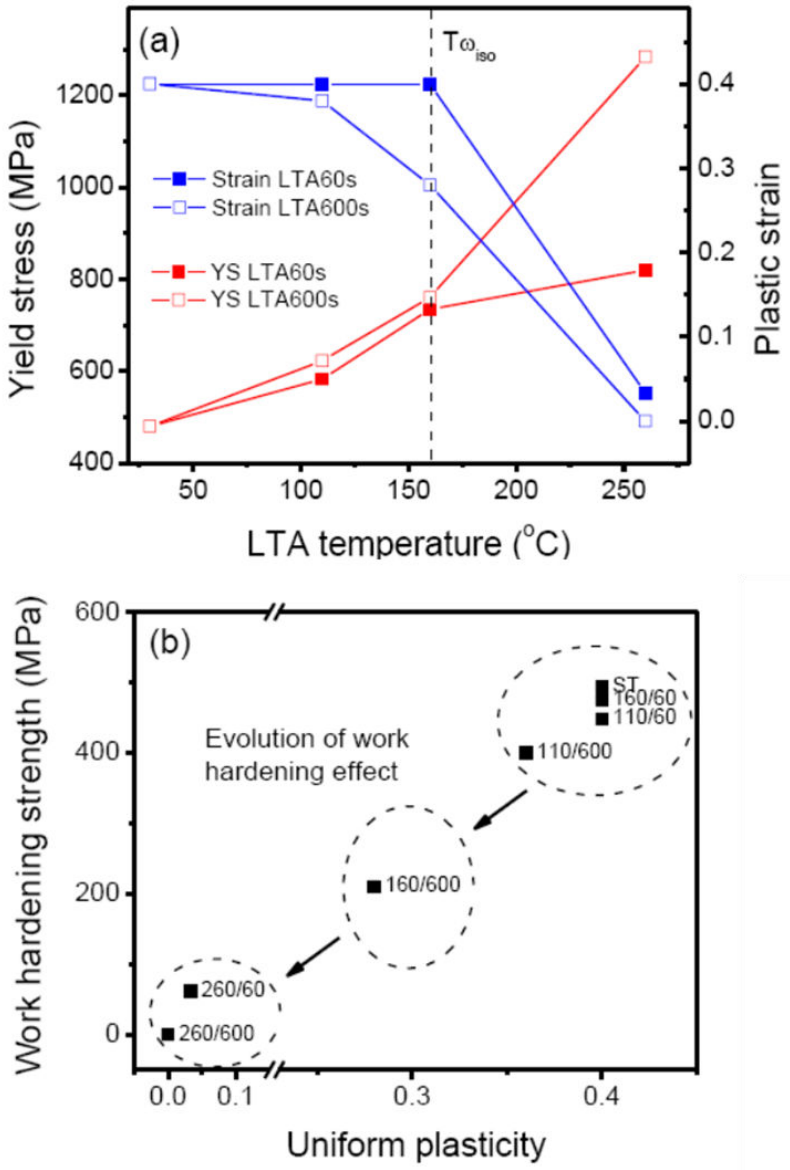

Figure 5.2 Summary of tensile properies of the ST specimen and LTA specimens, (a) plotting of yield stress and plastic strain of LTA specimens as a function of aging temperature, (b) plotting of work-hardening strength versus uniform plasticity. 3 groups of LTA specimens are divided by their apparent tensile performances.

5.2.2 Phase transformation during LTA treatments

The activation of different deformation modes is highly sensitive to the phase constitution in Ti-12Mo alloy. The phase constitution of the LTA specimens was analyzed by conventional XRD technique. Here, several typical XRD patterns are shown in Figure 5.3. The XRD profiles of LTA 110°C/600s and LTA 260°C/600s show a single β phase. But the LTA 310°C/600s profile confirms the occurrence of weak ω and α phase.

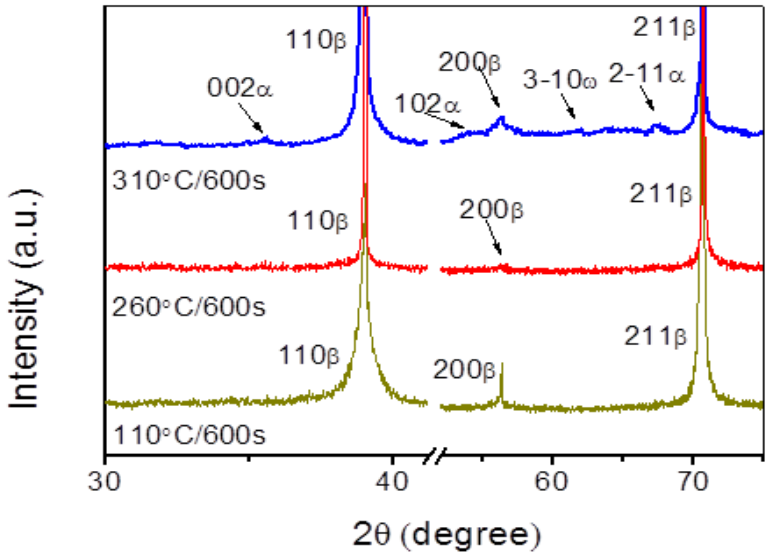

Figure 5.3 XRD profiles of the specimens after LTA treatments for 600s.

However, the conventional XRD technique used here can hardly detect the presence of ω_{ath} phase nor distinguish the ω_{iso} phase from ω_{ath} phase. In order to investigate the evolution of ω phase in LTA samples, the electrical resistivity measurement (ERM) technique has been used, which is an effective method to analyze the transitions of ω phases and α phase in metastable β Ti alloys **[14]**. Here, both isochronal mode and isothermal mode were applied to characterize the phase transformations during LTA treatments. The isochronal scanning from RT to 500°C is shown in Figure 5.4a to measure the transition temperatures for different phases. The phases (temperatures) are ω_{iso} phase ($T\omega_{iso}$), ω_{iso} assisted intragranular nano α phase ($T\alpha_{nano}$) **[14, 18]** and the conventional intergranular α phase (Tα). The

isochronal ERM curve starts by a negative temperature dependence (NTD) effect due to the ω_{ath} -> β transformation **[19]**. This transformation is fully reversible as a function of temperature before the activation of subsequent ω_{iso} and α phases **[19]**. $T\omega_{iso}$ is measured to be around 160°C. The temperature range of ω_{iso} precipitation is from $T\omega_{iso}$ to around 260°C, contributing to an increase in the electrical resistivity (ER) of the material. ω_{iso} assisted α_{nano} precipitation occurred at 260°C (Tαnano=260°C). A NTD effect is visible from 260°C due to the nucleation and growth of α_{nano} phase from ω phase, based on a strong contribution of ω vanishing process on total resistivity evolutions. Intergranular α phase precipitates at around 430°C (Tα=430°C), indicated by an interference on the NTD curve. The LTA temperatures were selected based on the critical transition temperatures detected by ERM. In order to clarify the LTA duration influences on phase transformations, isothermal measurements were applied at each LTA temperatures. The results are shown in Figure 5.4b. LTA 110°C is in the fully reversible β/ω_{ath} range. The ω_{ath}-> β transformation stopped after the first 100 seconds. And no further phase transformation was detected up to 600 seconds. LTA 160°C is at the ω_{iso} transition temperature. At the first 60s, the phase transformation is ω_{ath}-> β. ω_{iso} nucleation took place at 60s and its volume fraction kept increasing during the 600s LTA process. The volume fraction of the ω_{ath} transformed to β phase is proportional to the amount of ER decrease. According to the isochronal result (Figure 5.4a), the maximum ER decrease caused by β/ω_{ath} transition is about 0.01. Therefore, the LTA160°C/60s activated about 80% of ω_{ath} phase in a reversible passage, whereas about 20% in LTA110°C/60s. The β/ω_{ath} NTD curve was absent at 260°C ($T\alpha_{nano}$) due to the very high transformation rate. The ω_{iso} nucleation process finished in the first 60s with initial growth of the ω_{iso} nano particles. The 60s-600s range is composed by combined phase transformations, including further growth of ω_{iso} phase and precipitation of intragranular α_{nano} phase and intergranular α phase. It is in good accordance to the XRD analysis. The LTA treatments can be grouped according to the different types of phase transformations induced during LTA processes. First group: only reversible β/ω transitions were

involved in LTA 110°C/60s, 110°C/600s and 160°C/60s specimens; Second group: initial nucleation of ω_{iso} phase was induced in LTA 160°C/60s specimen; Third group: complete ω_{iso} nucleation + further growth of ω_{iso} phase and α phases were induced in LTA 260°C/60s and 600s specimens. This grouping based on phase transformations gives the same result as grouping by plastic performances (Figure 5.2b).

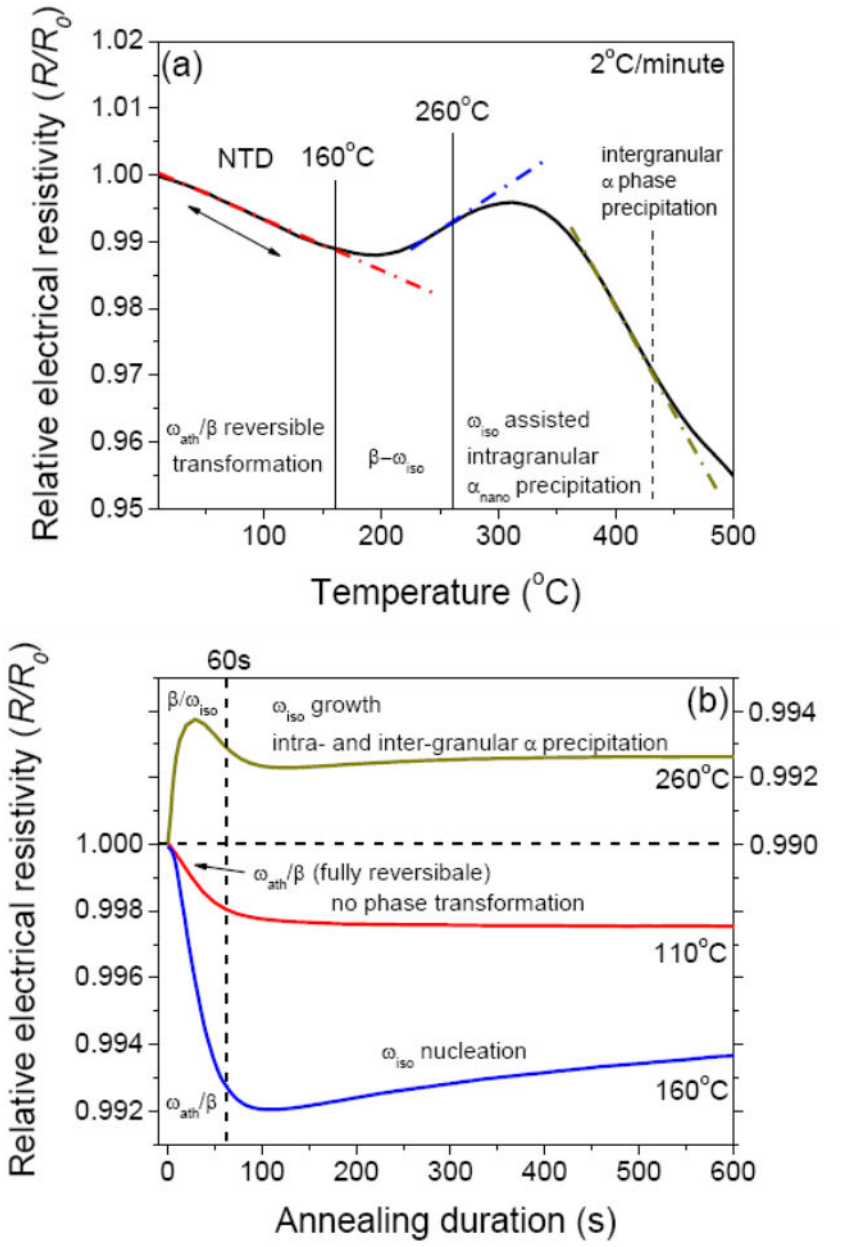

Figure 5.4 Relative electrical resistivity measurements on ST Ti-12Mo material, (a) non-isothermal scanning from room temperature to 500°C at a heating rate of 2 °C/minute, (b) isothermal aging for 600s at 110 °C, 160 °C and 260 °C, respectively, show the thermal induced phase evolution at each LTA process.

5.2.3 Deformation products

The phase transformations induced by plastic deformation were characterized by XRD on the LTA specimens after tensile tests until fracture. The XRD profiles are shown in Figure 5.5. The SIM α'' phase was detected in all the LTA specimens except LTA260°C/600s. The intensity of SIM α'' is decreasing when the LTA temperatures and durations are increasing. The SIM α'' is gradually suppressed by LTA treatments. According to our previous investigations of deformation mechanisms in ST Ti-12Mo **[17]**, the main deformation mode is a combination of stress induced martensitic (SIM) phase transformations and mechanical twinning. In detail, there are primary mechanisms, primary stress-induced ω and α'', primary twinning (T1st); and secondary mechanisms, SIM α'' and twins formed in the T1st zones. Since some of the LTA behaviors are very similar to that of ST specimen, there are two possible deformation products, the stress-induced ω and mechanical twinning, are not able to be characterized by conventional XRD.

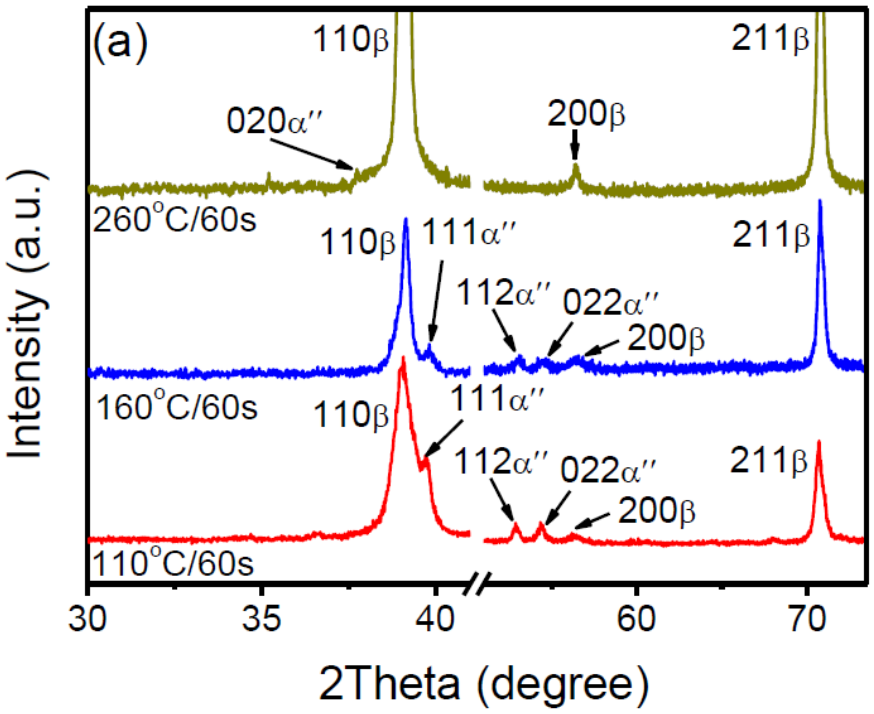

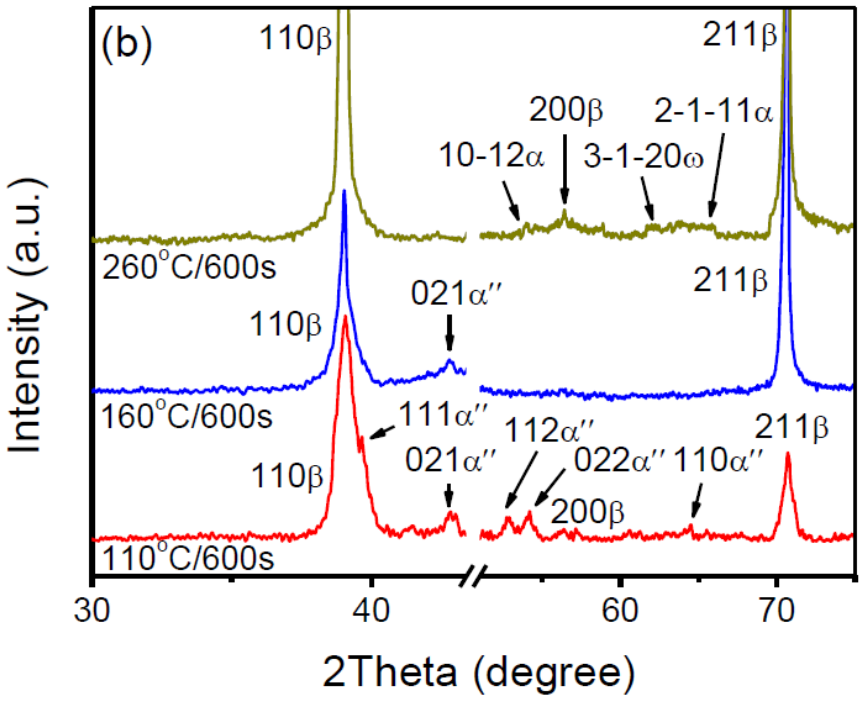

Figure 5.5 XRD profiles of the specimens after tensile deformation, (a) after LTA 60s, (b) after LTA 600s.

A series of TEM observations were performed to investigate these deformation mechanisms in LTA specimens. The deformation modes of LTA 110°C/60s, LTA 110°C/600s and LTA 160°C/60s specimens are shown to be almost similar to the ST state upon deformation. The microstructural details of LTA 160°C/60s specimen, the sample with best balance on strength and ductility, are shown in Figure 5.6 to clarify the LTA influences (fully reversible β/ωath transition) on TRIP/TWIP effects from ST Ti-12Mo. Figure 5.6a and b demonstrate the primary SIM α'' martensite at a grain boundary. The thickness and density of martensitic plates are both less than those in ST specimen **[12, 17, 20]** at the same strain level. However, the volume fraction and the density of stress-induced ω phase were both promoted after the LTA treatment when compared to ST state. In Figure 5.6c and d, the formation of a {332}<113> β twin was observed in a dense colony of parallel stress-induced ω lamellas. The twinning mode was characterized by SAED (inset of Figure 5.6c) to be {332}<113>β. Secondary SIM α'' and β twins were observed in a primary {332} β twin (shown in Figure 5.6e and f). The secondary twinning mode is {112}<111> according to the

SAED analysis. The 2nd twinning system in LTA specimen is different from that in ST state displaying a {332}<113> mode. Moreover, the density of such twins is also much higher than at ST state. These changes in the activation of deformation mechanisms are due to the reversible β/ω_{ath} passage of the first LTA group, resulting in the improvement of tensile strength without ductility reduction . It should be noticed that this unusual phenomenon was only accompanied by the aging process (T<Tωiso), before incubation of diffusion controlled ωiso precipitates. The diffusionless process implies an important microstructural influence from LTA to the β matrix on ωath level (dispersion of nanometric linear domains), leading to a major strengthening effect before elastic limit with minor modifications on plastic deformation behavior.

The deformation microstructure of 2nd group (LTA 160°C/600s) is shown in Figure 5.7. Both stress-induced ω phase and α'' phase are identified in the SAED pattern (inset of Figure 5.7a). Dark-field images (Figure 5.7a and b) show the morphology and distribution of these phases. The density of stress-induced ω lamellas and SIM α'' plates are much lower than those of 1st group. The size of SIM α'' plate is lowered. Primary twins were identified in {112}<111>β twinning system (Figure 5.7c and d). The density and volume fraction of these twins are limited. No more secondary deformation products were observed in this specimen. The tendency on suppression of the deformation products still increases in 3rd group LTA specimens. The deformation microstructure of LTA 260°C/60s is shown in Figure 5.8. stress-induced ω was the only deformation induced phase found in this specimen (Figure 5.8). The density and size of the stress-induced ω plate are very limited. Precipitate obstacles are visible on the edge of the ω plates (Figure 5.8a), resulting in the inhibition on forming lamella-like morphology. SIM α'' martensite and β twins were not found in the specimen. The massive dislocation glides in the 3rd group specimens were seriously impeded by isothermal precipitates, leading to very high tensile strength of 1200 MPa (LTA 260°C/600s) but almost no plasticity.

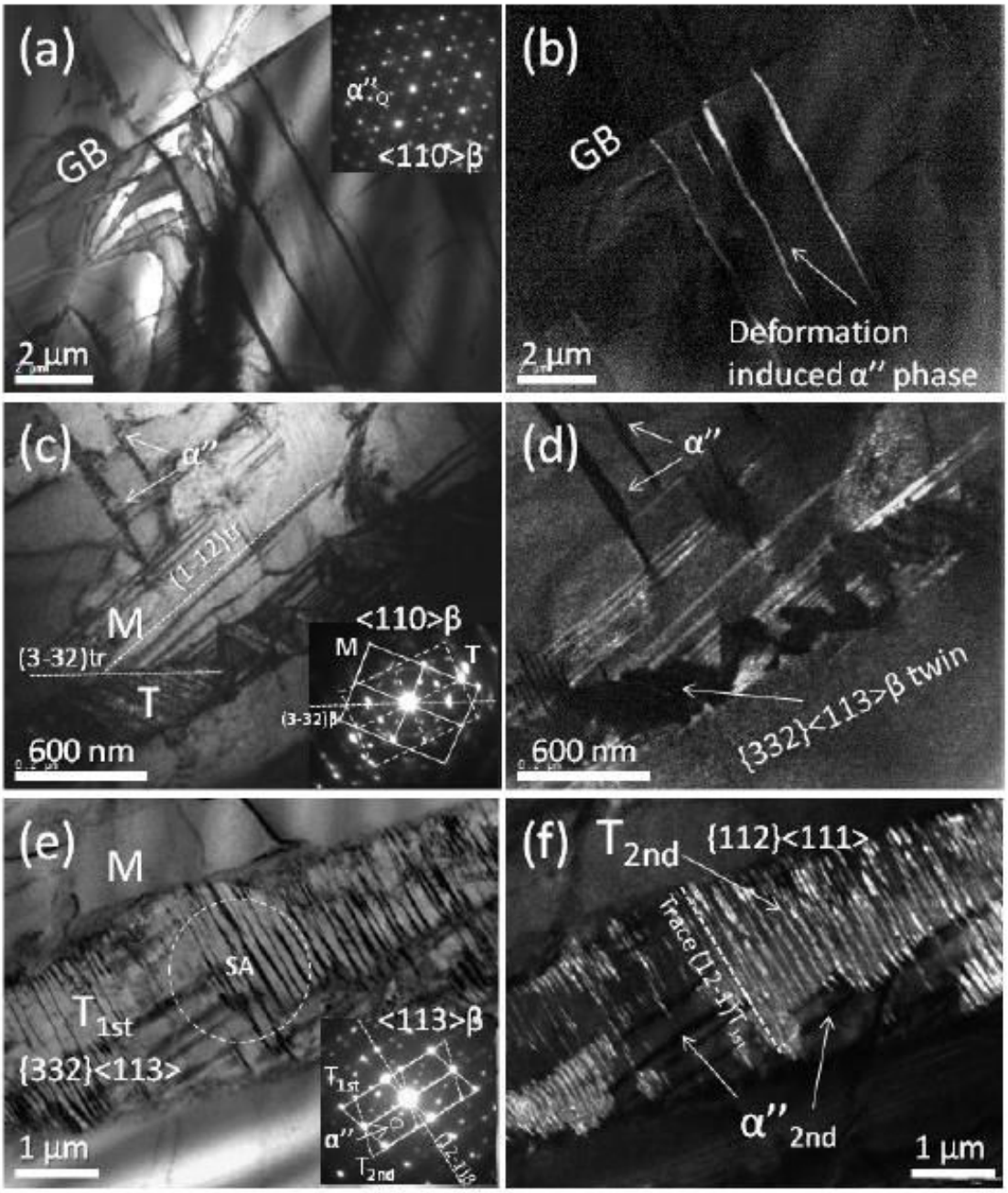

Figure 5.6 TEM observations of deformation mechanisms in LTA 160°C/60s specimen after strain. (a) Bright-field image of deformation induced α'' phase at a grain boundary (GB) with the corresponding SAED pattern (inset) at a zone axis of <110>β, (b) dark-field image of the SIM α'' plates. (c) Bright-field image of a β matrix (M) with stress-induced ω lamellas, SIM α'' plates and a {332}<113> β twin (T). The corresponding SAED pattern is shown with a schematic illustration of the twinning configuration, (d) the dark-field image of stress-induced ω lamellas. (e) Bright-field image of a primary {332}<113> β twin (T1st) with internal sub-structures. A diffraction pattern on the selected area (SA) at the twinned zone shows secondary twinning (T2nd) feature of {112}<111> configuration and SIM α'' signature, (f) the corresponding dark-field image of {112}<111> T2nd morphology.

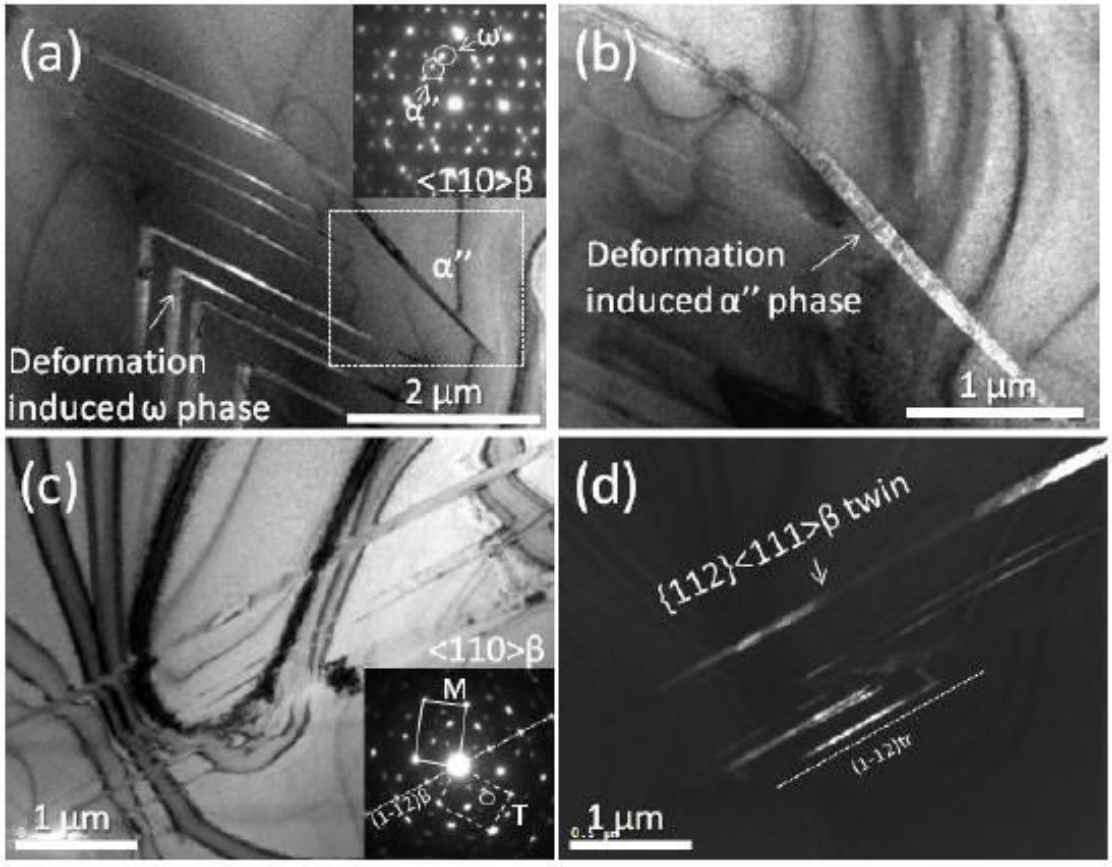

Figure 5.7 TEM observations of deformation mechanisms in LTA 160°C/600s specimen after strain. (a) SAED pattern (inset) at <110>β zone axis showing signatures of ω phase and α'' phase. The corresponding dark-field image of stress-induced ω lamellas, (b) the corresponding dark-field of SIM α'' plate. (c) Bright-field image of {112}<111> β twins. A SAED pattern at <110>β zone axis shows the schematic twinning configuration, (d) dark-field image of the {112}<111> β twins.

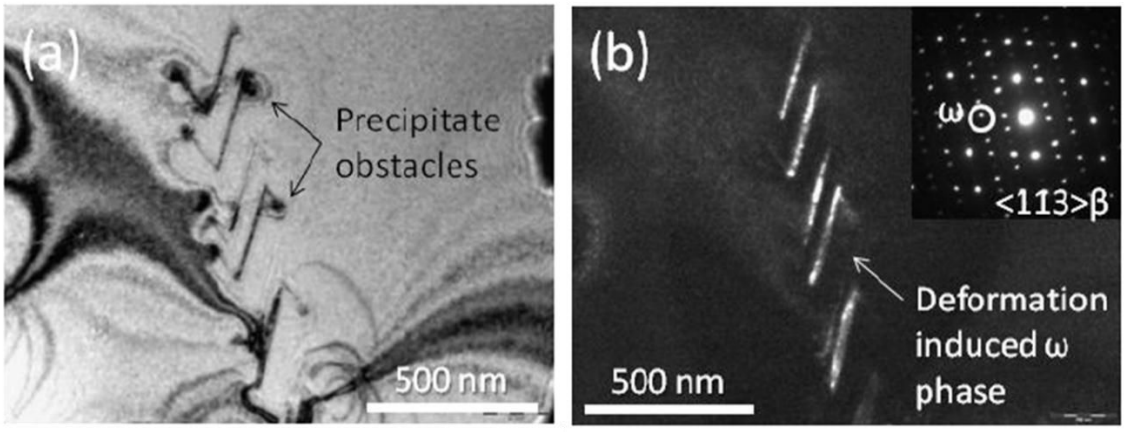

Figure 5.8 TEM observations of deformation mechanisms in LTA 260°C/60s specimen after strain. (a) Bright-field image shows stress-induced ω plates with precipitate obstacles on the edges, (b) the corresponding dark-field image of the stress-induced ω plates.

5.3 Discussion

An evolution of deformation modes was clearly shown from ST to LTA specimens. The chapter 4 showed that the deformation mechanisms are very complex in ST Ti-12Mo alloy. The mechanical behaviour is actually governed by combined TRIP and TWIP effects. The results showed that primary strain/stress induced phase transformations (β->ω and β->α'') and primary mechanical twinning ({332}<113> twinning) are simultaneously activated. Secondary martensitic phase transformation and secondary mechanical twinning are then triggered in the twinned β zones. When compared with the ST specimen, the deformation modes of LTA specimens display a tendency from collective stress-induced mechanisms + {332} twinning mode to stress-induced mechanisms + {112} twinning mode, and to deformation slip mode. The evolution route is a typical sequence widely reported in metastable β Ti alloys by changing the chemical stability towards β phase stabilization **[8, 13]**. However, the evolution mechanism involved in LTA treatments is different from the compositional modification according to the deformation microstructural features observed in this study except LTA 260°C/600s. In this specimen, there is clearly α precipitation (XRD result in Figure 5.5b), which may lead to an exo-diffusion of β stabilizers from the particles towards the β matrix. This results in a progressive chemical stabilization of β phase and a subsequent reduction of mechanical "instability" of the material. However, in the other LTA specimens, isothermal phase transformations are limited prior to the complete nucleation of ω_{iso} phase due to the low aging temperature and very short aging duration. Actually, the 600s aging treatment at 160°C for Ti-12Mo grade alloy is still in the incubation period of ω_{iso} precipitation **[21]**. Since the growth of such phase is controlled by diffusion of Mo, it requires an isothermal aging in the order of magnitude of 10^4 seconds at around 160°C to reach equilibrium state **[21]**. Therefore, the chemical composition of initial ω_{iso} nuclei induced by LTA is still far from chemical equilibrium with respect to the surrounding β matrix. In these cases, the modification of chemical instability is not the major influence induced by LTA

treatments. It should be considered that other structural factors, such as quenched-in ω_{ath} phase and LTA induced nano particle dispersions, may play a role in the activation of various deformation mechanisms. For example, the deformation mode is moderately changed by the nucleation of ω_{iso} phase in LTA 160°C/600s (2nd group). Actually, its deformation mode, i.e. the combined TRIP and TWIP effects, are still preserved in the specimen due to the low ω_{iso} phase volume fraction. Beyond the well-known embrittlement effect of such phase **[16, 22, 23]**, the possible inhibition of TRIP (related to stress induced α'' precipitation) and change of TWIP effect (from {332}<113> system to {112}<111> system) may be connected to a nano-structuration effect. While precipitating in the β matrix, the coherent ω_{iso} particles induce strong coherency strain fields contributing to inhibit both α'' precipitation and the precursor of mechanical twinning, the stress-induced ω phase.

Among all of the presented mechanisms, stress-induced ω phase occurred in every deformation processes at very early stage, regardless their LTA histories. Such stress-induced ω phase could play a key role in the selection of deformation modes. Actually, based on the TEM results, the size and density of the stress-induced ω lamellas are closely related to the formation of twin, both of {332} and {112} modes. Generally speaking, the proportion of twinning activation is the essential factor in work-hardening effect and subsequently affects the plastic stability. It has been reported that {112} twinning is assisted by formation of stress-induced ω precursor by sharing the shear strain on {112} planes **[10]**. A transitional model on atomic displacement has been proposed in details, based on the displacive mechanisms between thin ω layer and the twin in a BCC matrix **[24]**. Hypothesis is made that such effect actually occurred in LTA 160°C/600s specimen. Concerning {332} twinning system, several attempts on establishing transition models **[25-27]** have been made by assuming a reshuffling process (a zigzag displacement typical for hexagonal crystals) on the minimum displacement of atoms. However, according to these models, distortion of the symmetry between two twin boundaries is encountered

during occurrence of the atomic shuffles **[28]**. A dislocation model **[29]** has been proposed by introducing a slip of partial a/22<113> dislocation to form a twin. The movement of such partial dislocations also requires reshuffling of the atoms along ±a/22<332> directions. In this study, a new evidence is found that a {332} twin formed via a stress-induced ω colony with high density of lamellas (Figure 5.6c and d). It can be noticed that the twinning plane is not parallel to the habit plane of stress-induced ω lamellas (Figure 5.6c). As a consequence, a trans-ω layer nucleation phenomenon is probably involved in the twinning formation. It can be seen from this investigation that the volume fraction of the stress-induced ω phase seems to have a great influence on the volume fraction of mechanical twinning. Consequently, the density of stress-induced ω lamellas is critical for twin nucleation based on such mechanism.

On the aspects of quenched-in ω_{ath} phase, reversible transition between β/ω_{ath} and especially the relationship between such phase and the formation of stress-induced ω phase, a small amount of works have been done. A recent report **[30]** on ω_{ath} precipitation presented experimental evidences on β matrix instabilities in ST Ti-Mo alloys. It is suggested that the formation of ω-like embryos from competing compositional and structural instabilities arising in the bcc lattice during rapid cooling from the high-temperature single β phase field. The displacive partial collapse of the {111} planes of the parent BCC structure within compositionally phase-separated regions containing several at.% less of Mo, forming ω-like embryos as a "frozen" state. It has been well-known that the frozen ω embryos can be transformed back to β phase by LTA before the activation of Mo diffusion **[19, 31]**, resulting in a recovery process of the partial collapse of the {111} planes. It is speculated that the recovery process involves an emission of dislocations on {112} planes. The increasing of dislocation density strengthens the BCC matrix, and may favor the subsequent formation of stress-induced ω phase upon loading. This assumption could explain the relationship between a reversible β/ω_{ath} passage and

mechanical strength found in LTA 160°C/60s like specimens (1st group). As an interesting result, the LTA 160°C/60s specimen is strengthened by a reversible β/ω_{ath} passage on 80% of ω_{ath} phase (Figure 5.4b), resulting in an increase of the yielding stress about 50% without any loss in ductility (Figure 5.1a). The resulting deformation microstructure demonstrates the highest density of stress-induced ω among the LTA specimens and a subsequent formation of {332}<113> twinning conducted by multi stress-induced ω lamellas (Figure 5.6c and d). The detailed mechanisms are still not clear, and surely need intensive additional investigations. Nevertheless, the "activation" of the frozen ω_{ath} phase is of great effectiveness in the optimization of the TRIP/TWIP related deformation performances in a metastable Ti-Mo alloy.

5.4 Conclusion

The deformation mechanisms of various modes have been investigated by an approach based on a set of short-time LTA treatments at 110°C, 160°C and 260°C for 60 and 600s, respectively, on ST Ti-12Mo samples showing a combined TWIP/TRIP effect. According to the mechanical performances, the LTA specimens can be shared by three groups, 1st: LTA 110°C/60s, LTA 110°C/600s and LTA 160°C/60s; 2nd: LTA 160°C/600s; 3rd: LTA 260°C/60s and LTA 260°C/600s. The evolution of deformation modes is due to the low temperature phase transformations induced by LTA treatments, involving both ω_{ath} and ω_{iso} phases. The detailed features are summarized below.

(1) The deformation modes of the three groups exhibit an evolution as a function of LTA temperatures and durations. 1st group: primary stress-induced ω and α'' precipitations + primary {332}<113> twinning + secondary SIM α'' precipitations and intense {112}<111> twinning in the twinned β zone. 2nd group: stress-induced ω and α'' precipitations + {112}<111> twinning, no secondary mechanisms. 3rd group: few stress-induced ω + deformation slip.

(2) The best combination of mechanical properties was achieved at LTA 160°C/60s

(1st group), exhibiting a high strength (close to 1200MPa of true stress) and a stable plasticity of ε=0.4 (true strain) with a significant work-hardening effect.

(3) Short-time LTA treatments induce insignificant influences on chemical instability of β matrix. The microstructural transitions, i.e. reversible β/ω_{ath} passages and isothermal nano ω/α precipitations, are of great importance on controlling the appearance of deformation products, i.e. stress-induced ω, SIM α'' and mechanical twins. Among them, stress-induced ω precipitation plays a key role in the activation of different deformation modes.

References

[1] F. Sun, Y.L. Hao, S. Nowak, T. Gloriant, P. Laheurte, F. Prima, J. Mech. Behav. Biomed. 4 (2011) 1864-1872.
[2] I. Weiss, S. Semiatin, Mater. Sci. Eng. A 243 (1998) 46-65.
[3] S. Li, Y. Zhang, B. Sun, Y. Hao, R. Yang, Mater. Sci. Eng. A 480 (2008) 101-108.
[4] J.Y. Zhang, F. Sun, Y.L. Hao, N. Gozdecki, E. Lebrun, P. Vermaut, R. Portier, T. Gloriant, P. Laheurte, F. Prima, Mater. Sci. Eng. A 563 (2013) 78-85.
[5] M. Hida, E. Sukedai, C. Henmi, K. Sakaue, H. Terauchi, Acta Metall. 30 (1982) 1471-1479.
[6] G. He, J. Eckert, W. Löser, Acta Mater. 51 (2003) 1621-1631.
[7] F. Sun, S. Nowak, T. Gloriant, P. Laheurte, A. Eberhardt, F. Prima, Scripta Mater. 63 (2010) 1053-1056.
[8] A. Gysler, G. Lutjering, V. Gerold, Acta Metall. 22 (1974) 901-909.
[9] J. Williams, B. Hickman, H. Marcus, Metallurgical and Materials Transactions B 2 (1971) 1913-1919.
[10] P.J.S. Buenconsejo, H.Y. Kim, S. Miyazaki, Acta Mater. 57 (2009) 2509-2515.
[11] M.A. Meyers, A. Mishra, D.J. Benson, Prog. Mater. Sci. 51 (2006) 427-556.
[12] F. Sun, F. Prima, T. Gloriant, Mater. Sci. Eng. A 527 (2010) 4262-4269.
[13] H. Paris, B. LeFevre, E. Starke, Metallurgical and Materials Transactions A 7 (1976) 273-278.
[14] T. Gloriant, G. Texier, F. Sun, I. Thibon, F. Prima, J.L. Soubeyroux, Scripta Mater. 58 (2008) 271-274.
[15] D. Moffat, D. Larbalestier, Metallurgical Transactions A 19 (1988) 1687-1694.
[16] B. Hickman, J. Mater. Sci. 4 (1969) 554-563.
[17] F. Sun, J.Y. Zhang, M. Marteleur, T. Gloriant, P. Vermaut, D. Laillé, P. Castany, C. Curfs, P.J. Jacques, F. Prima, Acta Mater. 61 (2013) 6406-6417.

[18] F. Prima, P. Vermaut, G. Texier, D. Ansel, T. Gloriant, Scripta Mater. 54 (2006) 645-648.
[19] F. Prima, P. Vermaut, T. Gloriant, J. Debuigne, D. Ansel, J. Mater. Sci. Lett. 21 (2002) 1935-1937.
[20] M. Marteleur, F. Sun, T. Gloriant, P. Vermaut, P.J. Jacques, F. Prima, Scripta Mater. 66 (2012) 749-752.
[21] F. Sun, D. Laillé, T. Gloriant, J. Therm. Anal. Calorim. 101 (2010) 81-88.
[22] D. De Fontaine, Metallurgical and Materials Transactions A 19 (1988) 169-175.
[23] A. Bowen, Royal Aircraft Establishment, Farnborough, Eng., 1971.
[24] H. Xing, J. Sun, Appl. Phys. Lett. 93 (2008) 031908-031908-031903.
[25] A. Crocker, Acta Metall. 10 (1962) 113-122.
[26] Y. Takemoto, M. Hida, A. Sakakibara, J. Jpn. Inst. Met. 57 (1993) 1471-1472.
[27] J.W. Christian, S. Mahajan, Prog. Mater. Sci. 39 (1995) 1-157.
[28] G.M. Rusakov, A.V. Litvinov, V.S. Litvinov, Met. Sci. Heat Treat. 48 (2006) 244-251.
[29] V. Litvinov, A. Popov, Fizika Metallov i Metallovedenie(Russia) 83 (1997) 152-160.
[30] A. Devaraj, S. Nag, R. Srinivasan, R. Williams, S. Banerjee, R. Banerjee, H. Fraser, Acta Mater. 60 (2012) 596-609.
[31] F. Prima, J. Debuigne, M. Boliveau, D. Ansel, J. Mater. Sci. Lett. 19 (2000) 2219-2221.

Chapter 6

Development of ternary Ti-Mo based alloys showing combined TWIP/TRIP effects

6.1 Introduction

In order to enlarge the binary model Ti-12Mo to ternary metastable β Ti-alloys by using “d-electron design method”, the third alloying elements were added into the Ti-12Mo alloy. Two kinds of ternary alloys were designed, i.e. Ti-9Mo-6W material and Ti-12Mo-xZr (x=1, 3, 5) materials. The detailed alloy design procedure about these alloys has introduced in chapter 2. The $\overline{\mathrm{Bo}}$ and $\overline{\mathrm{Md}}$ of the so-designed ternary alloys were indicated in Figure 6.1. Two objectives are possible to be realized by adding third alloying elements: (1) to validate the possibility of the “d--electron design method” effects as a theoretical prediction tool applied on the ternary composition about practical alloying developments and performance optimization. (2) to investigate the relationships between stress-induced phase transformations and mechanical twinning in the new ternary system. As a consequence, the mechanical performances of these ternary alloys are investigated, and microstructural characterizations are profiled by using X-ray diffraction (XRD), Electron Backscattered Diffraction (EBSD), Automated Crystal Orientation Mapping on TEM (ACOM-TEM) and transmission electron microscopy (TEM). Finally, the deformation mechanisms underlying the mechanical behavior were discussed, based on the detailed microstructural investigations.

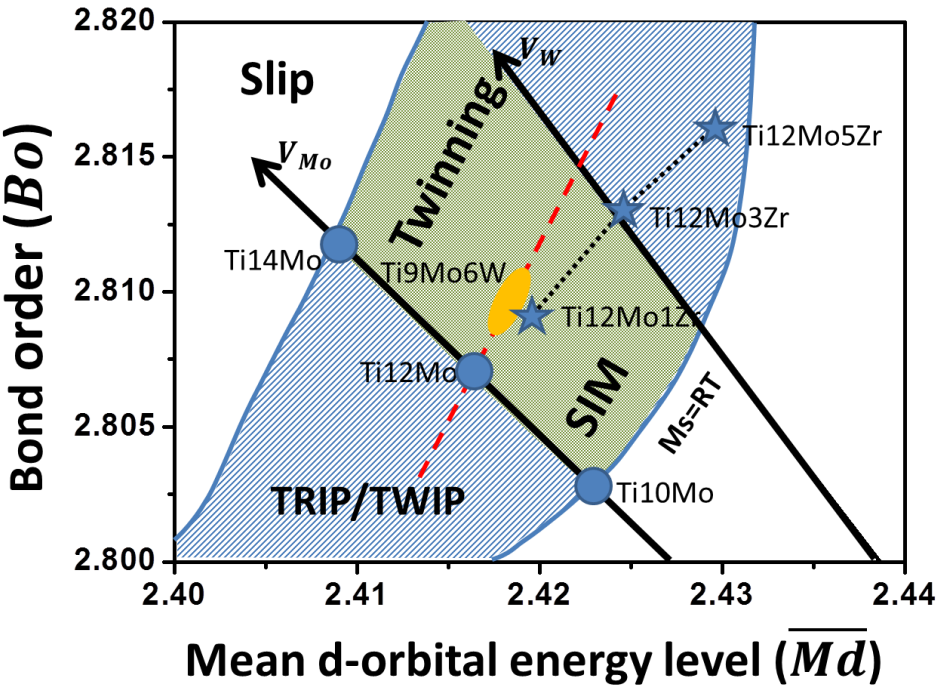

Figure 6.1 The "d-electron" design map with Ti-Mo/W vectors presents different zones of deformation mechanisms. And the formulated chemical compositions of so-designed ternary alloys are indicated in the map.

6.2 Results and discussions

6.2.1 Development of Ti-9Mo-6W ternary alloy

6.2.1.1 Tensile performances

The uniaxial tensile test was carried out on the as-quenched Ti-9Mo-6W sample at room temperature. The true stress-true strain curve of the sample, as well as the evolution of the work-hardening rate (θ=dσ/dε) as a function of the true stress, were shown in Figure 6.2. Meanwhile, the true stress-true strain and work-hardening rate curve of Ti-12Mo alloy was also shown in Figure 6.2 as a reference. It can be seen from Figure 6.2a that the Ti-Mo-W material showed excellent combination of high strength (ultimate tensile strength =1100MPa) and high ductility (uniform elongation ≈ 35%). The strength is improved of about 100 MPa higher than that of the Ti-12Mo

material. Moreover, the Ti-9Mo-6W material exhibits a large work-hardening behavior at the full uniform plastic deformation range. The evolution of work-hardening rate was very similar with the Ti-12Mo material and showed three different stages (Figure 6.2b). The first stage was the elastic-plastic transition, the work-hardening rate jumps. Subsequently, the work-hardening rate rapidly increased to reach a maximum. Then, the work-hardening rate smoothly decreased down to the end of uniform plastic deformation. The maximum value of the work-hardening rate of the Ti-9Mo-6Wmaterial was approximate 2000 MPa at ε=0.15. The ultimate tensile strength (UTS), yield strength (YS) and maximum work-hardening rate of Ti-9Mo-6W were all improved with comparing to these parameters of Ti-12Mo, although the uniform elongation of this material exhibited a little decrease. It has been proved in chapter 4 that Ti-12Mo alloy exhibits excellent mechanical behavior due to complex deformation mechanism including concurrent combination with the stress-induced phase transformation and mechanical {332}<113> twinning. Compared with Ti-12Mo alloy, the mechanical behavior has been further improved. Thus, it was necessary to investigate the deformation mechanism underlying the excellent performance. In order to clarify the deformation mechanisms, detailed microstructural investigations were performed on Ti-9Mo-6W alloy.

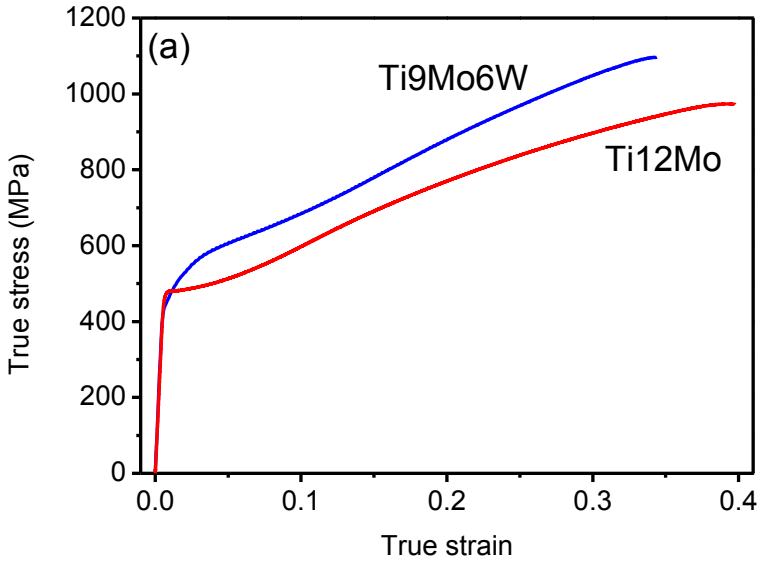

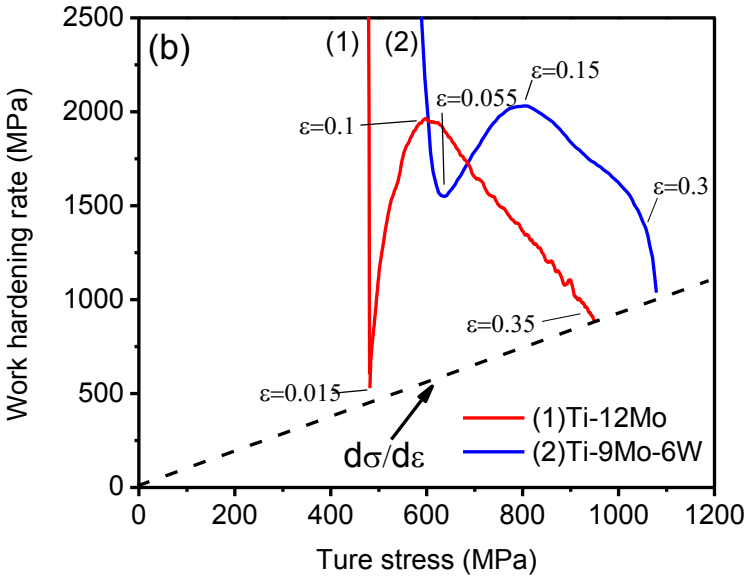

Figure 6.2 (a) True strain-stress curves of Ti-9Mo-6W and Ti-12Mo under uniform plastic deformation, (b) plots of work-hardening rate (dσ/dε) as a function of true stress of two alloys.

6.2.1.2 Microstructural evolution

The performance of the plastic deformation of Ti-9Mo-6W material demonstrates similar features as those of Ti-12Mo due to combined TRIP/TWIP effects, i.e. strong non-monotonous evolutions in a stress-strain curve and in the corresponding work-hardening curve. The similarity shown in the two alloys implies the same TWIP/TRIP effects activated in the ternary Ti-Mo-W alloy. The detailed information about TWIP/TRIP effects was proved by combination of XRD, EBSD and ACCOM TEM methods.

Figure 6.3 shows the XRD profiles of as-quenched sample at different deformed levels. After deformation, the stress-induced phase transformation starts to occur. At the onset of plastic deformation, the intensity of stress-induced phase is very weak. With increasing strain, the intensity of residual stress-induced phase gradually becomes stronger, indicating that the volume fraction of the stress-induced phase increases. It can be noticed that the intensity of the stress-induced martensite

gradually increases at the early plastic deformation. However, the intensity of strain induced ω phase seems to firstly increase, followed by reaching a maximum at ε=0.05, and then decrease according to the XRD patterns of deformed samples. In chapter 4, it has been proved by SXRD analysis that the intensity of strain induced ω phase reaches a maximum at ε≈0.08 for Ti-12Mo material. The tendency of strain induced ω phase of Ti-9Mo-6W material seems to be similar to the Ti-12Mo material. Moreover, the detailed information can be further confirmed by TEM observation.

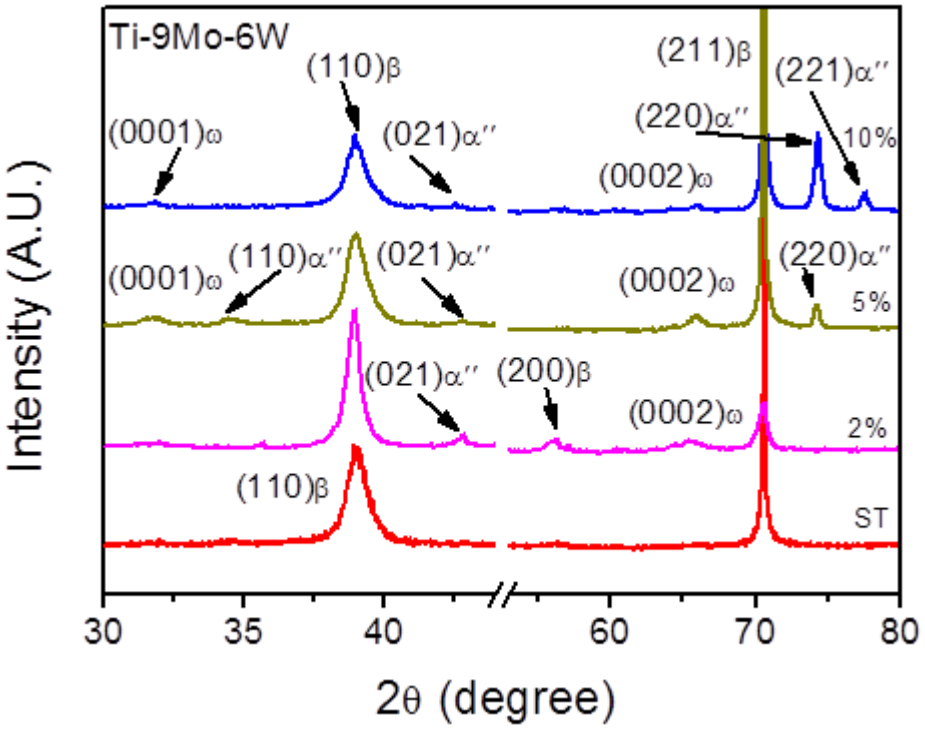

Figure 6.3 The XRD profiles of Ti-9Mo-6W deformed samples at different strain levels.

EBSD orientation mapping (Figure 6.4) displays a general view of the deformation microstructure after 0.05 of strain in tension. Intragranular deformation bands were shown in the deformed polycrystalline β matrix. Figure 6.4.b shows that most of the deformation bands can be indexed as α'' precipitation. Complex composites bands can additionally be observed in grains A and C (marked by black circles). As shown in Ti-12Mo, two kinds of configuration are actually possible: either α'' can be precipitated as a primary product or can fill completely a primary twin, as a secondary product. In grain C, the two situations are co-existing and the

deformation corresponding to black arrow is originally a primary twin. At this deformation level, the α'' precipitation seems to be the predominant mechanism whereas at 0.05 strain, the twinning volume fraction is already high in Ti-12Mo. This may be responsible for the increased plateau visible on the stress-strain curve and the resultant postponing of work-hardening in Ti-9Mo-6W.

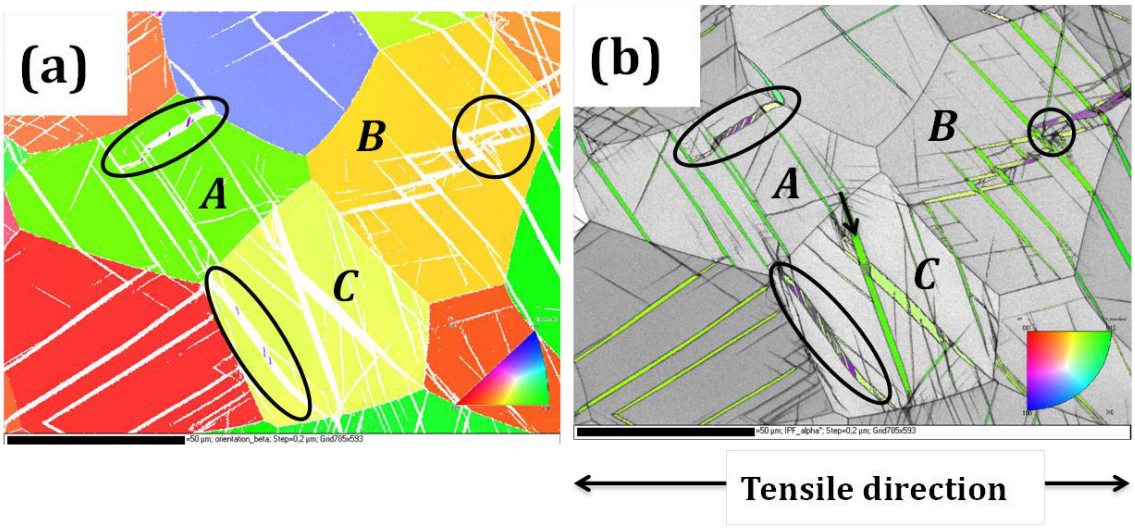

Figure 6.4 EBSD mapping of the Ti-9Mo-6W alloy after deformation, (a) orientation mapping of β phase, (b) orientation mapping of deformation induced α'' phase. Three grains of interest are labelled by A, B and C. The maximum resolved shearing directions on the mapping plane are shown by τ1 and τ2, respectively.

The most interesting feature in the deformed microstructure is the presence of complex, thick and distorted bands in grains A and C (marked by black cycles). Inside these bands, it can be identified that small segments of residual {332} type mechanical β twins and two variants of SIM α'' are currently coexisting, similarly to the mechanisms shown in Ti-12Mo, where the primary twinning bands are partially or even fully occupied by secondary SIM α''.

TEM investigations were performed to clarify these sub-micrometric features in the marked area. Figure 6.5 presented TEM investigations at a zone similar to Grain B (Figure 6.4) in a sample strained at 0.10. A colony of very fine SIM α'' (region Figure 6.5d) is accompanied by mechanical twinning (region Figure 6.5b). The twinning type can be identified as a {332}<113>twinning by conventional selected area diffraction

pattern (Figure 6.5c) along [011]beta zone axis. This means that TRIP and TWIP effects can occur locally, at the same time, in an independent way (as primary mechanisms). A more accurate investigation shows that the situation is somehow more complex. Automated Crystal Orientation Mapping on TEM (ACOM TEM) was used, out of zone axis, to retrieve the complete information on phases, orientation and morphologies. As illustrated in Figure 6.5d, three different crystallographic orientations for stress induced α'' can be observed. Calculation of the respective misorientations shows that they correspond to two variants of a primary stress induced transformation (i.e. from the initial beta matrix) and a single variant coming from a secondary stress induced transformation (i.e. from a beta twinned zone). Figure 6.5.e shows that the misorientation between 1st α" and 2nd α'' is close to 51o, which implies their β parents were twinned based on the {332}<113>twinning system, since the corresponding theoretical misorientation is 50.57o. These observations show that, as in Ti-12Mo, the material possess different ways to accommodate the stress, and all these ways can be activated at the same time.A more peculiar example of synergetic effect between TRIP and TWIP can be given with the investigation of complex deformation bands already shown in grain A and C (Figure 6.4)

Figure 6.6 presented the details of the microstructure (TEM bright field image in Figure 6.6a) and phases (ACOM mapping in Figure 6.6b) in one of these bands along <110>β zone axis. At this region, several different microstructural elements can be observed: β matrix, SIM α'' phase, athermal ω phase (ω_{ath}), lamellar-like stress induced ω phase (ωD), primary twinning and secondary twinning. It can be observed that the microstructure is extremely complex in such a deformation band. In order to simplify the algorithm for computer-assisted nano beam diffraction (NBD) matching, phase distribution mapping was performed on α'' phase. The SIM α'' phase distribution is displayed in orange (Figure 6.6b) and β matrix with ω is shown in blue colour (Figure 6.6b). The phase distribution map (Figure 6.6b) demonstrates that the

bulk deformation band is actually “constructed” by adjacent α” regions and β regions. The local nano-beam diffraction analysis shows that α” regions are composed of two different α” variants. One of these variants (marked by white dash-line in Figure 6.6b) is analyzed (NBD2) to be formed from a twinned β zone, as a secondary α” phase, whereas NBD1 shows that primary α” plates correspond to the white zones on the TEM bright field image (Figure 6.6a). Investigating the whole deformation band, the dash-line regions on Figure 6.6b can be identified as 2ndary α”phase transformed from primary beta twins with lenticular morphologies. On beta region, thick stress induced ω plates (ωD) are observed (NBD3 zone) and identified as a single variant. These ωD plates are parallel to {112}β planes. Figure 6.6c illustrates a simplified scheme of this band by reconstructing its structural unit using components of ωD plates, twinning and SIM, following their crystallographic relationships. The occurrence of such twisted deformation bands in a deformed titanium alloy is unusual and has never been observed before, from the best of our knowledge. The main point of interest relates to the propagation mode of such a band that appears to proceed from a collective activation of the available deformation mechanisms, in a confined zone. ωD has been previously shown to be an early stress induced product as thin lamellas (at ε= 0.007 in Ti-12Mo). Therefore, thickening of these lamellas towards plates, upon deformation, may be taken as a reasonable hypothesis in Ti-9Mo-6W.A large volume fraction of α” phase is observed inside the band, originating from a direct (one step) mechanism βmatrix→α”, on one hand, and from a two steps mechanism βmatrix→βtwinned→α”, on the other hand. Chronology and detailed mechanism of the deformation band propagation are still unclear. However, is can be observed through the occurrence of such composites bands in Ti-9Mo-6W that, in this family of Ti-alloys, TRIP and TWIP effects are far to be independent mechanisms but work in a collective and synergetic way, with both primary and secondary mechanisms being activated in confined regions. It is thought that this interconnected network of deformation mechanisms may create extra transgranular interfaces, significantly decreasing mean free path for dislocation slip as a dynamical

Hall-Petch effect. Consequently, a very high work-hardening rate close to 2100 MPa and a uniform plasticity of larger than 35% can be recorded in Ti-9Mo-6W, thanks to this collective TRIP and TWIP effects.

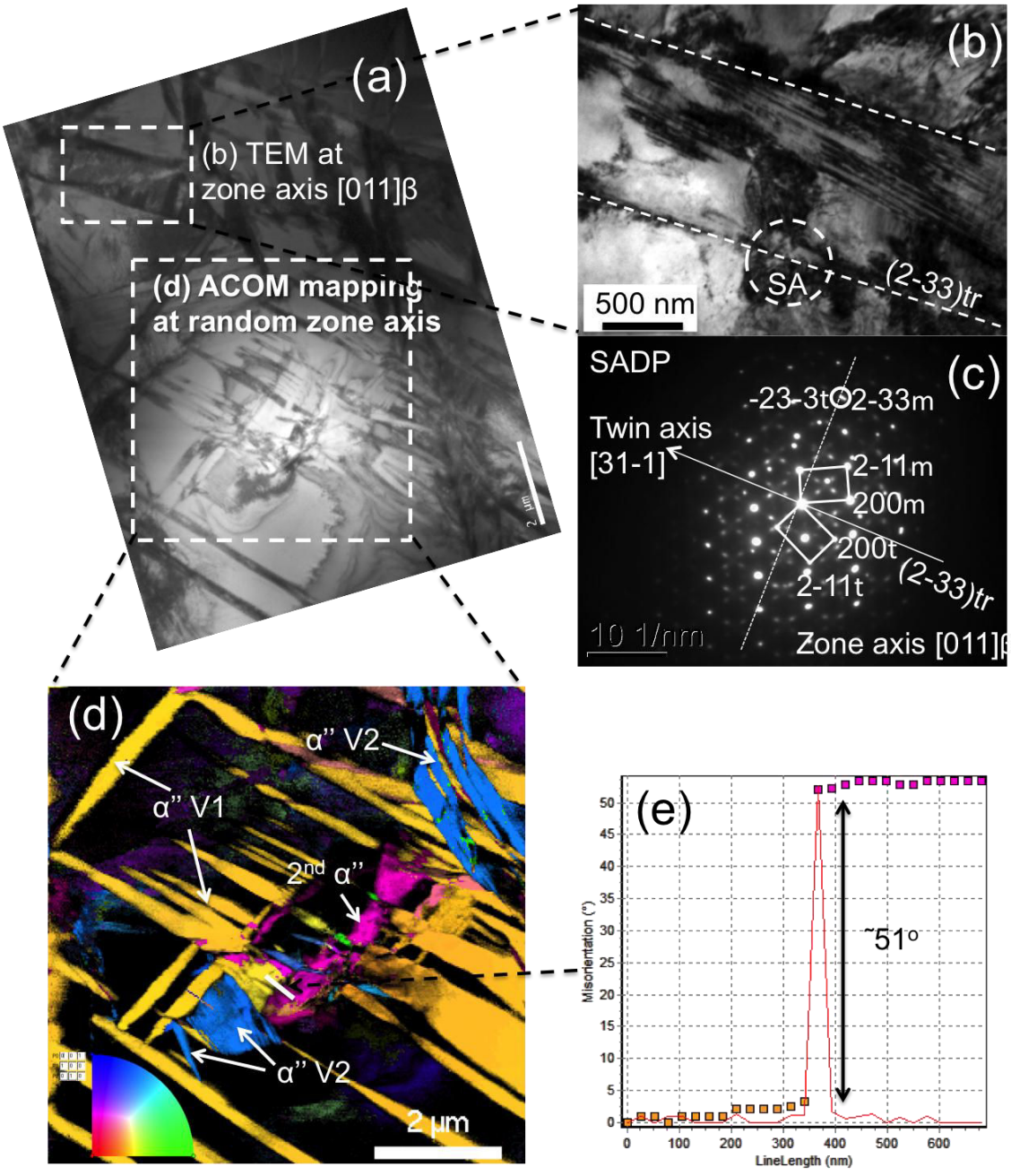

Figure 6.5 TEM investigations on a zone similar to the marked area in Grain B (Fig. 2). (a) TEM bright field image; (b) a {332}<113> twinning interface with (c) identification on selected area diffraction pattern (SADP); (d) ACOM TEM mapping on α'' phase distribution and orientation; (d) misorientation measured between 1st α'' and 2nd α''.

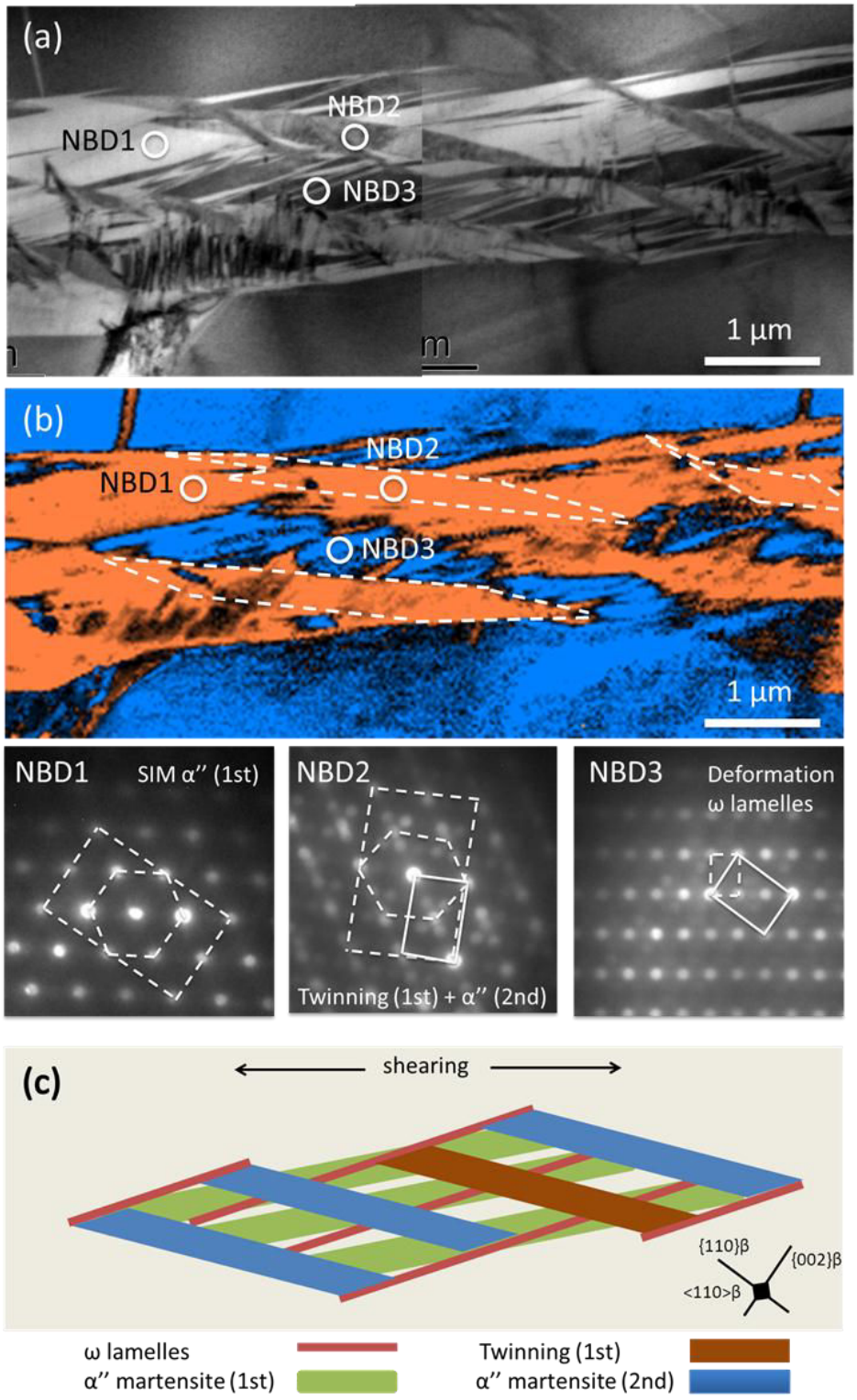

Figure 6.6 TEM investigations on a band similar to the marked area in Grain A and C (Fig. 2). (a) TEM bright field image of the band; (b) ACOM TEM mapping on α'' phase distribution; (c) a schematic drawing of the deformation bands, formed in collective method among ω lamellas, twinning and α'' martensites. Three nano-beam diffraction patterns (NBD1, NBD2 and NBD3) are presented correspond to the locations marked in (a) and (b).

6.2.2 Ternary Ti-Mo-Zr alloys

6.2.2.1 Mechanical behavior

After solution-treatment, the uniaxial tensile tests of the Ti-12Mo-xZr (x=1, 3, 5) specimens were carried out at room temperature. The results determined from the stress-strain curves were listed in Table 6.1. Figure 6.7 displays the true stress-true strain curves and the work-hardening rate ($\theta=d\sigma/d\varepsilon$) of the Ti-12Mo-xZr materials at as-quenched state. Meanwhile, the true stress-true strain and work-hardening rate curve of Ti-12Mo alloy was also shown in Figure 6.7. According to the Table 6.1 and Figure 6.7a, comparing with Ti-12Mo material, the yield strength and tensile strength can be obviously improved via adding Zr elements, but their ductility and elastic modulus somewhat decrease. Especially, the Ti-12Mo-1Zr material exhibits excellent mechanical behavior that high strength (yield strength =690MPa and ultimate tensile strength =1143MPa) and good ductility (uniform elongation ≈ 30%). The yield strength and ultimate tensile strength of Ti-12Mo-1Zr material are improved of about 42%, 17% higher than these of the Ti-12Mo material, respectively. Moreover, the Ti-12Mo-xZr materials also exhibit a noticeable work-hardening behavior at the whole uniform plastic deformation range. As shown in Figure 6.7b, the features of work-hardening rate of these alloys are very similar with the Ti-12Mo and Ti-9Mo-6W materials, and shows strongly non-monotonous evolution. After the elastic–plastic transition, the work-hardening rate exhibits a rapidly increase up to the maximum and then decrease during the uniform plastic deformation. The phase constitutions and microstructural characterization have been used to prove that the TRIP and TWIP effects contribute to the mechanical behavior in Ti-12Mo and Ti-9Mo-6W materials. Similarly, it is necessary to classify the detailed phase constitutions and microstructural evidences of combined TRIP and TWIP effects in the Ti-12Mo-xZr materials.

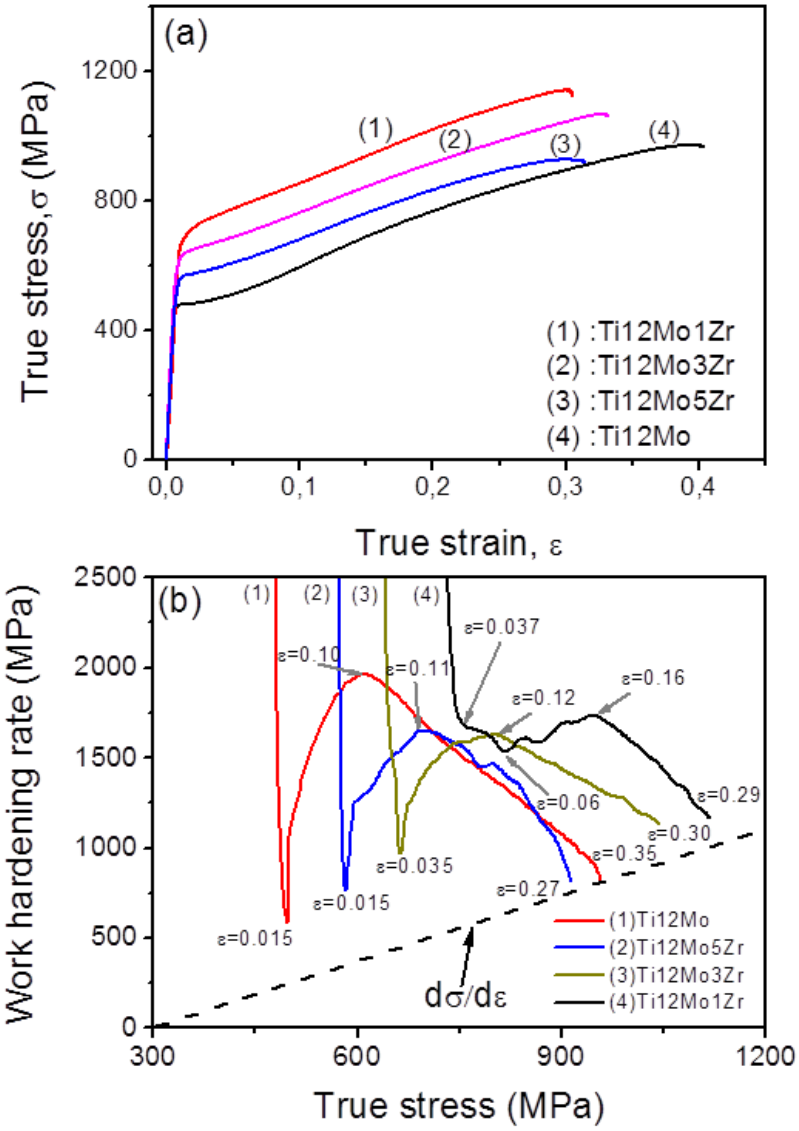

Figure 6.7 (a) True strain-stress curves of Ti-12MoXZr (X=1, 3, 5) and Ti-12Mo under uniform elongation, (b) plots of work-hardening rate (dσ/dε) as a function of true stress.

Table 6.1 Tensile properties and Vickers hardness of the Ti-Mo-Zr alloys

Alloys	YS (Mpa)	UTS (Mpa)	ER (%)	Elastic modulus (GPa)	Lattice parameter of β phase
Ti-12Mo	487	980	53.48	85	3.266
Ti-12Mo-1Zr	691	1143	35.76	81	3.269
Ti-12Mo-3Zr	632	1070	39.21	80	3.275
Ti-12Mo-5Zr	568	930	39.91	77	3.291

6.2.2.2 Phase constitutions and microstructure feature

Figure 6.8 shows the XRD profiles of the ST Ti-12Mo-xZr (x=1, 3, 5) materials. The phases of the Ti-12Mo-xZr samples consist of main β phase and weak athermal ω phase. By measuring the lattice parameters of β phase (also listed in table 6.1), the lattice slightly increase with Zr content increasing. It may be because the addition of the larger atom radius of Zr elements (0.16 nm) compared with Mo elements (0.14 nm) results in the slight distortion of lattice parameter in β phase. It has been reported that alloying elements such as O, Al, Zr and Sn retard the formation of athermal ω phase in metastable β titanium **[1]**. From the XRD profile, very weak ω_{ath} phase was detected in all the ST Ti-12Mo-xZr alloys. However, the conventional XRD measurement used in laboratory can't provide accurate qualitative analysis on the ω_{ath} volume fraction

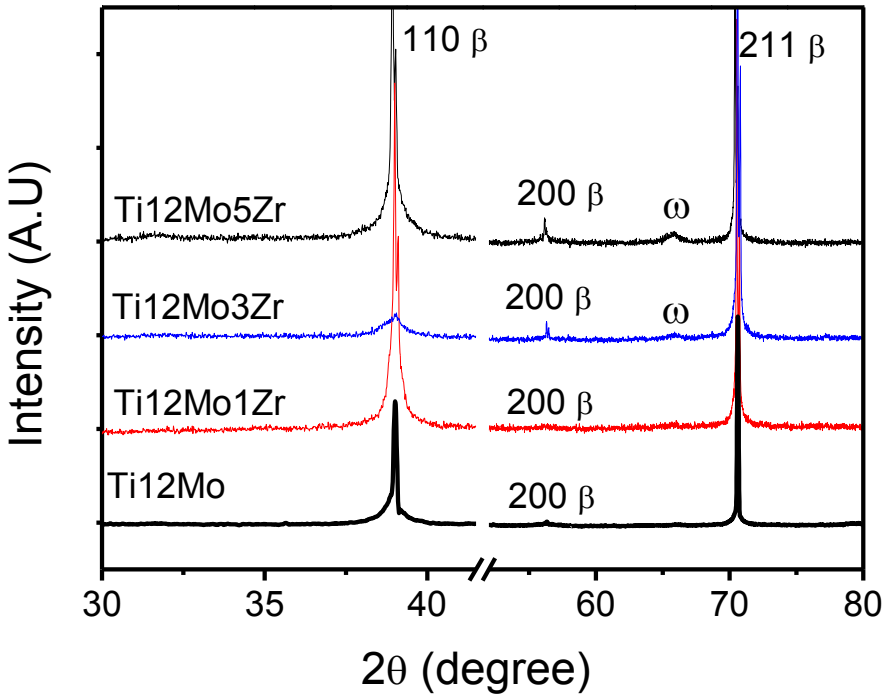

Figure 6.8 The XRD profiles of the Ti-12Mo-xZr materials at as-quenched state.

The Ti-12Mo-xZr materials exhibit good ductility, which are close related to the deformation mechanism. Similar to Ti-12Mo material, the stress-induced phase

transformation and mechanical twinning also occurred in Ti-12Mo-xZr materials. The detailed information about the deformation mechanism can be analyzed via the XRD and TEM methods. The results show that the stress-induced phase transformation consisted of stress-induced martensitic phase as well as stress-induced ω phase. Figure 6.9 shows the TEM images of stress-induced ω phase at the onset of plastic deformation. The stress-induced ω lamellar in thickness of 10 to 20 nm appeared in the β matrix. Meanwhile, the stress-induced martensitic transformation also occurred. It can be seen from Figure 6.10a that the intensity of (111) α″ and (113) α″ are very strong, revealing the facts that the stress-induced martensitic transformation occurred upon strain. Aiming to analyze the effect of Zr content on the residual SIM α″, the integrated XRD intensity of residual SIM α″ as a function of Zr content was plotted in Figure 6.10b. The integrated XRD intensities of residual SIM (111) α″ and (113) α″ phase exhibit an increasing tendency, indicating that the residual SIM α″ increase with the Zr content increasing when strained at ε=0.1.

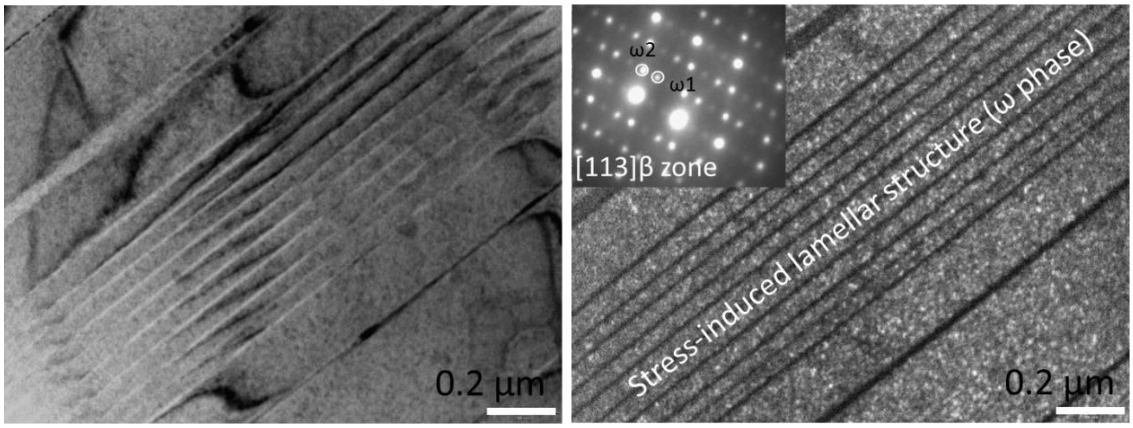

Figure 6.9 The TEM images of the deformation-induced ω phase at the onset of plastic deformation. (a) Bright-field image and (b) Dark-field image of the ω phase in matrix, respectively. The corresponding diffraction patterns are presented in the insets of dark-field image.

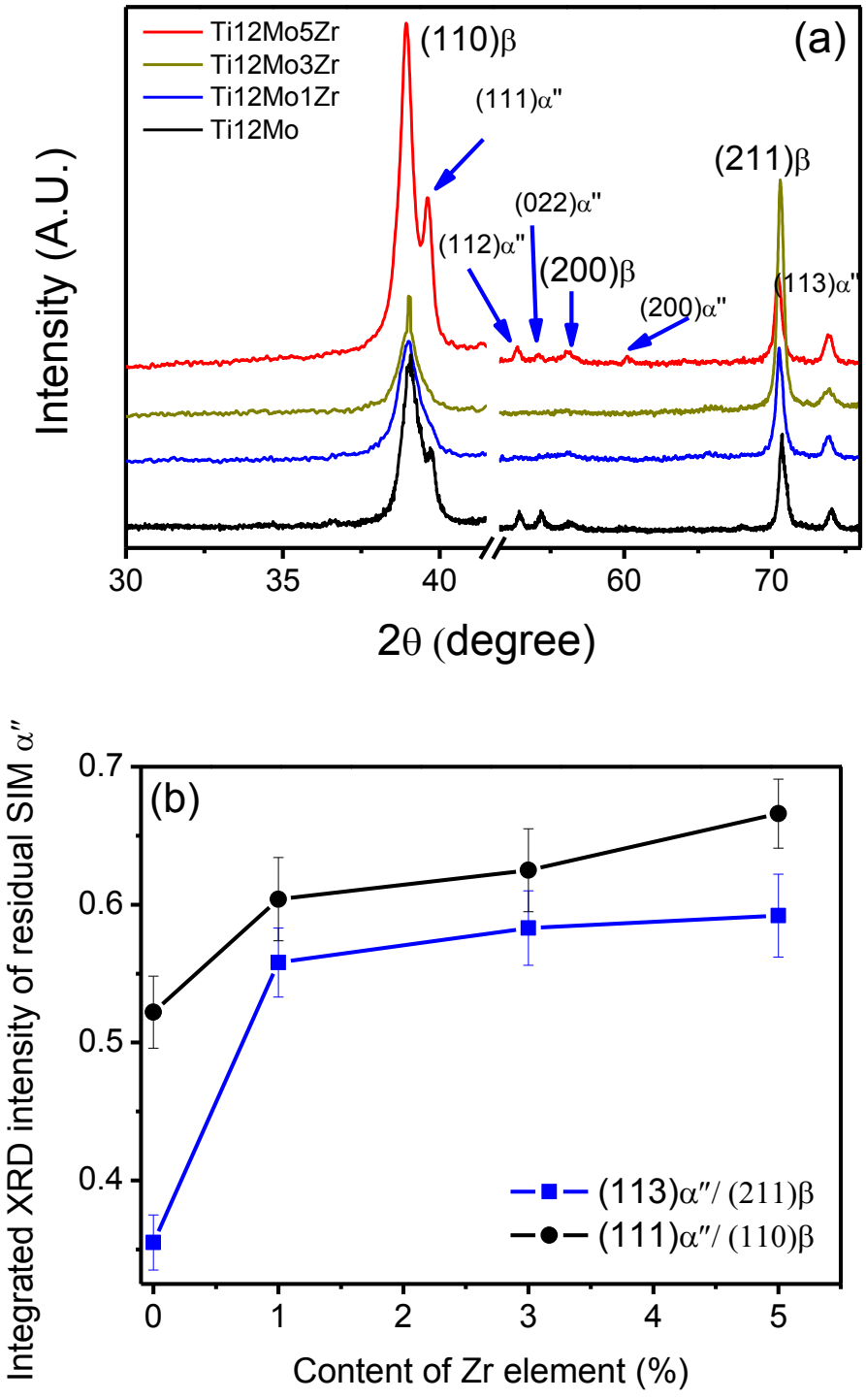

Figure 6.10 (a) The X-ray diffraction profiles of the deformed samples of Ti-12Mo-xZr alloy at ε=0.1. The X-ray diffraction profile of the deformed sample of Ti-12Mo material is also plotted as a reference; (b) The integrated XRD intensity of residual SIM α˝ as a function of content of Zr element, the blue line is the XRD intensity ratio between (113) α˝ and (211)β, the black line is the XRD intensity ratio between (111) α˝ and (110)β.

In metastable β alloys, the twin, {332}<113> type and {112}<111> type, is an important deformation mechanism, which type will dominate the plastic deformation completely depends on the stability of β phase **[2-4]**. In the metastable Ti-12Mo-xZr alloys, the twin mode was determined to be mainly {332}<113> type twin by TEM technique. An example indicating {332}<113> twinning in Ti-12Mo-1Zr sample strained ε=0.5 is shown in Figure 6.11. Figure 6.11a shows the bright field TEM image of two different direction of deformation plate indicated by dash line. Aiming to identify the structure of the stress-induced plates, the electron diffraction of different selected areas (SA) is carried out. The diffraction patterns of the selected area (SAD) taken from the boundary region of two kinds of deformation plates (SA1 and SA3) and the matrix (SA2), are shown in Figure 6.11 (b-d). It is identified to be two variants of {332}<113> twinning, and the traces of $\overline{32}3$ and $3\overline{3}2$ twin plane are also labeled on the bright field image. By measuring the angle between two planes, the angle about 81° is very close to the angle between $\overline{32}3$ and $3\overline{3}2$ plane (about 82°), which indicates the occurrence of the {332}<113> twinning obeying the crystal orientation relation. In order to further investigate the substructure during plastic deformation, the twinned domain of SA1 (Figure 6.11a) has been observed with a magnified observation. Figure 6.12 shows the TEM image of the substructure. The fine substructure (Figure 6.12b) is identified to be secondary {332}<113> twinning plates (~50nm) according to the corresponding diffraction pattern of selected area (Figure 6.12a) shown in Figure 6.12c. It has been found that the alloys, Ti-12Mo-3Zr and Ti-12Mo-5Zr, having the same deformation mode of {332}<113> twinning, contribute to the similar work-hardening behavior.

The SIM α″ transformation was triggered during plastic deformation. Actually, the stress-induced martensitic transformation appeared not only in the matrix, but also in twinned bands. Figure 6.13 shows the TEM images of the secondary SIM α″ inside {332}<113> twinning of Ti-12Mo-5Zr specimen strained at ε=0.1. Figure 6.13a shows the bright field of the matrix and substructure, and two kinds of SAD taken

from the matrix (SA1) and the substructure (SA2) are carried out. It is identified that the substructure is the secondary SIM α″ phase appeared inside the primary {332}<113> twinning (Figure 6.13b) based on the corresponding SAD (Figure 6.13d)).

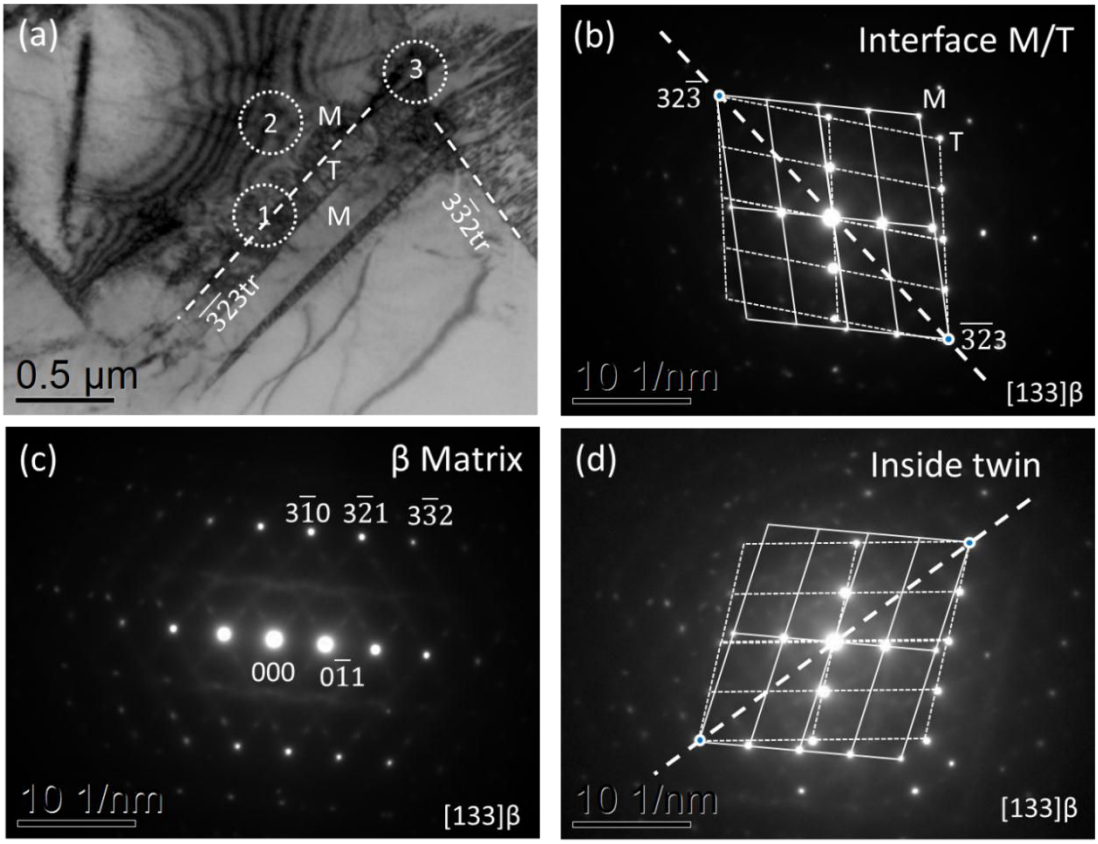

Figure 6.11 The TEM images of primary {332}<113> twinning of the Ti-12Mo-1Zr sample strained at ε=0.05. (a) the bright field of the {332}<113> twinning and matrix, three selected areas were plotted by dash solid which taken from the boundary region of the deformation plates and the matrix. The trace of two variants of {332}<113> twinning were also indicated; (b-d) the diffraction patterns of SA1, SA2 and SA3, respectively. The zone axis of the SAD is [133]β.

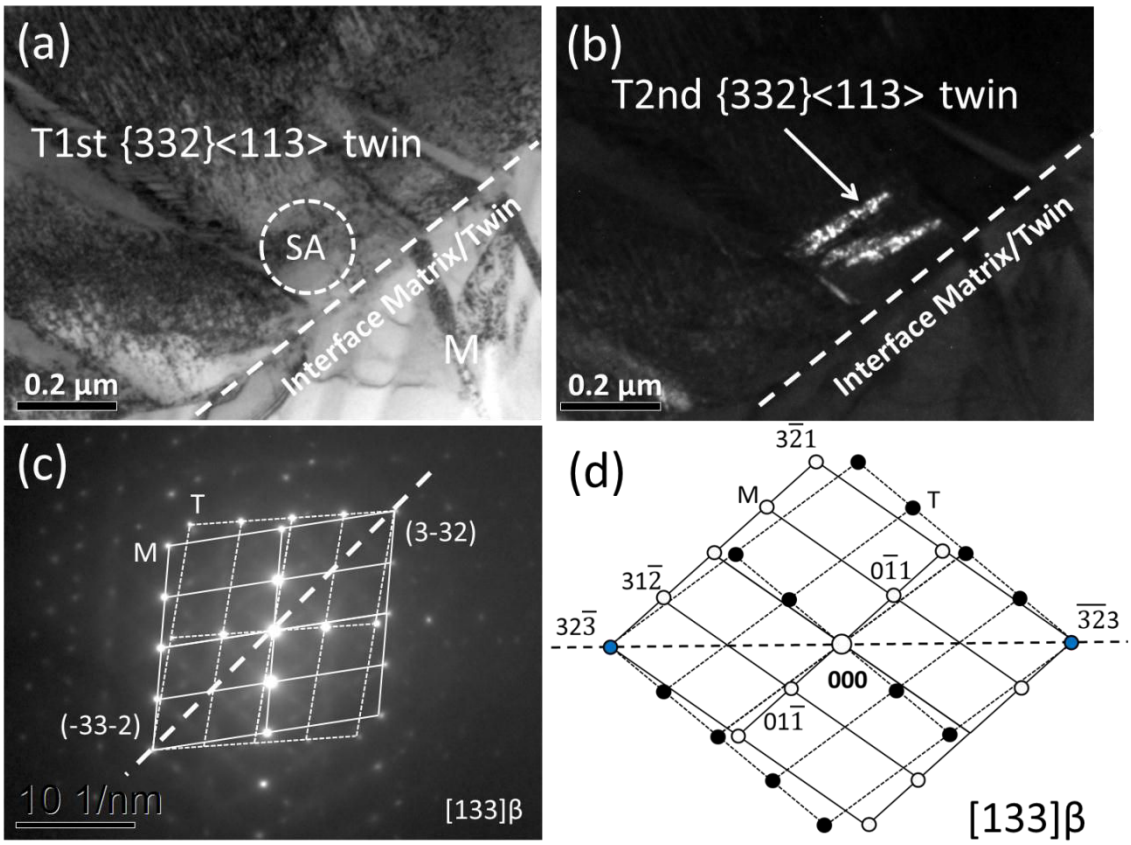

Figure 6.12 The TEM images of secondary {332}<113> twinning of the Ti-12Mo-1Zr sample strained at ε=0.05, where is taken from one of deformation plates at site SA1 in Figure 6.11. (a) and (b) the bright and dark field image of the secondary {332}<113> twinning, respectively; (c) the corresponding diffraction pattern of the selected area in (a), the zone axis is [133]β; (d) the schematic diagram of (c).

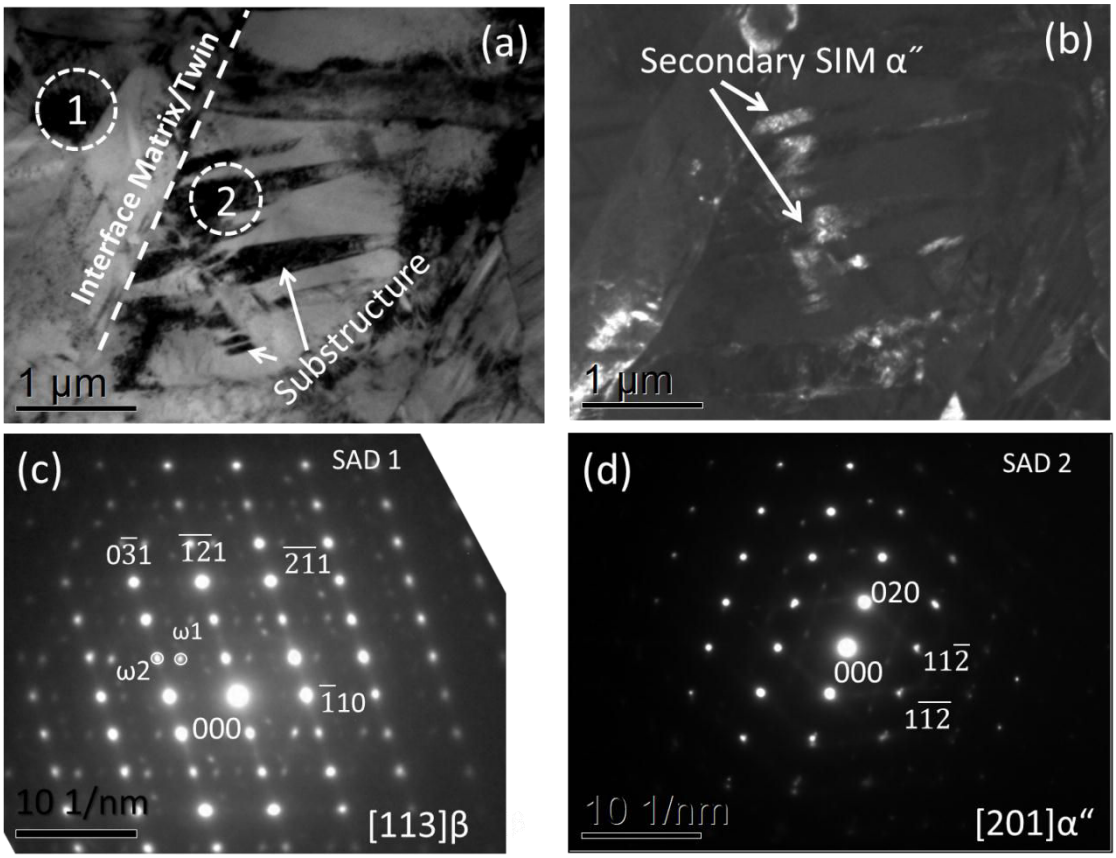

Figure 6.13 The TEM images of substructure of the Ti-12Mo-5Zr sample strained at ε=0.1. (a) and (b) the bright and dark field images of substructure, respectively. Two selected areas (SA) were also indicated on the bright field image; (c) the corresponding diffraction pattern of SA1; (d) the corresponding diffraction pattern of SA2.

According to the Figure 6.1, the designed procedure of ternary Ti-Mo based alloys shows that the $\overline{\mathrm{Bo}}$ and $\overline{\mathrm{Md}}$ values of Ti-12Mo-xZr slightly shifted the “iso-stability” line. The composition of Ti-12Mo-xZr shifted to the boundary of stress-induced martensitic phase transformation with increasing Zr content. It means that the SIM transformation seems be preferred to occur, which can be proved by loading-unloading tensile tests. The volume fraction of SIM α" (Vα") was determined by the volume fraction of residual martensite ($V^{r}_{\alpha"}$) and the volume fraction of reversible SIM α" transformation α"→β ($V^{R}_{\alpha"}$). The tendency of the residual martensite can be detected by XRD technique. As for adding Zr into the Ti-12Mo alloy, the corresponding intensity of the residual SIM α" increases with Zr content

increasing when the samples strained at ε=0.1 (Figure 6.10). The reversible SIM α" transformation is close related with the pseudo-elastic behavior upon unloading. Thus, the evolution of the reversible SIM α" transformation can be indirectly evaluated by loading-unloading tests. The cyclic loading-unloading tensile tests were carried out on the ST Ti-12Mo-xZr samples by 5% increment. The recovery strains through reversible SIM α" transformation were determined from the curves of cyclic loading-unloading tests. Here, the four cyclic recovery strains as function of the strain were plotted in Figure 6.14. It can be seen that the recovery strains increase with Zr content increasing, which indicates that the volume fraction of reversible stress-induced transformation increases with increasing Zr content for the same strain level. Combined with the analysis of the residual SIM α" and reversible SIM α", it reveals that the volume fraction of the stress-induced martensitic transformation during plastic deformation increases with Zr content increasing.

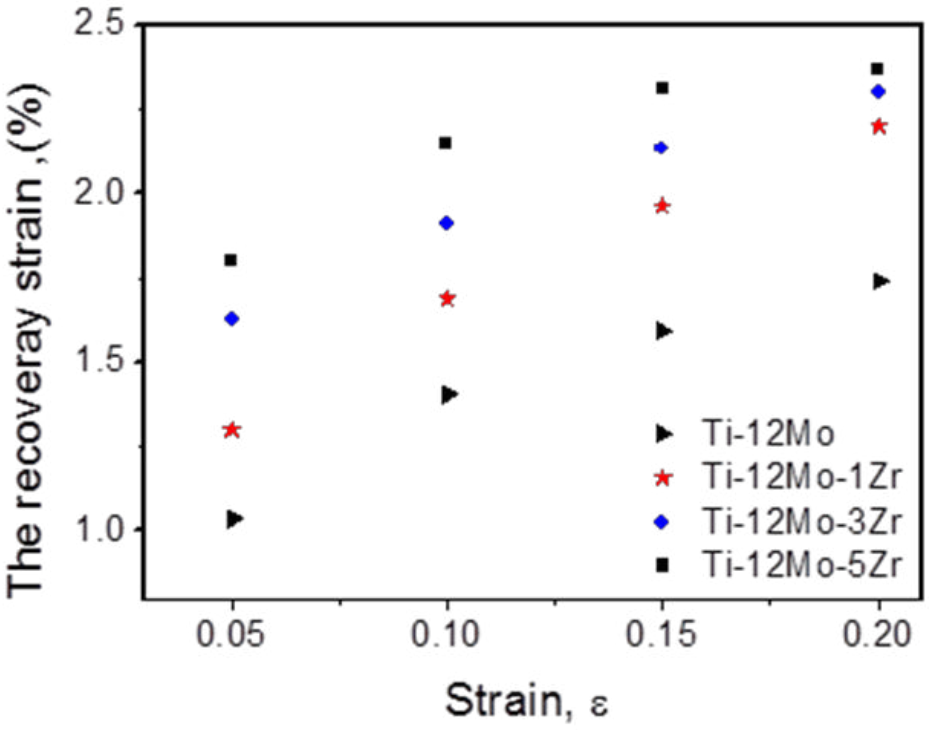

Figure 6.14 The recovery strain determined from the reversible SIM α" as function of strain are plotted for the Ti-Mo based alloys.

The phenomenon concerning the increasing of Ms temperature with increasing

of Zr content is unusual as reported in many other alloying systems, e.g. Ti-V-xZr **[5, 6]** or Ti-Nb-xZr **[7]**. In order to study this phenomenon, a series of low temperature resistivity measurements were performed in the athermal ω range (-160°C – 300°C). The results from each alloy (1Zr, 3Zr and 5Zr) are shown in Figure 6.15. The measured ωs temperatures of the Ti-Mo-Zr alloys exhibit little influence as a function of Zr content. The ωs temperature is stable at around 170°C (similar to that of Ti-12Mo). However, the ωf temperature decreases rapidly with increasing Zr content (1Zr~-95°C, 3Zr~-160 °C, 5Zr < -160 °C). The enlarged ω temperature range implies an increased stability of β matrix in the β/athermal ω transition. As a consequence, the volume fraction of ωath precipitation may be largely suppressed by Zr addition. But unfortunately, no direct measurement on the quenched-in ωath volume fraction was performed due to the experimental limitation under conventional laboratory condition (e.g. XRD and TEM). Quantitative synchrotron radiation XRD measurement would be effective in the measurement of ω_{ath} volume fraction. On the other hand, many experimental evidences can be found in literatures showing that the suppression effect of neutral elements (Zr and Sn) on ωath phase in Ti-Nb system **[1, 8]**. In some of the compositions (e.g. Ti-24Nb-4Zr-8Sn), the ω_{ath} phase can be totally inhibited in as-quenched state, but still showing stress induced martensitic phase transformation in elastic range. The suppression of ω_{ath} phase leads to the reduction of mechanical properties (i.e. young's modulus and elastic limit). Such reduction on mechanical strength was also shown in our Ti-Mo-xZr alloys (Figure 6.7a). However, it is thought that the reduction mechanism may not be identical to the Ti-Nb system. As reported by our early work (on Ti-Nb-Zr alloy **[7]**) and other related reports, the alloying nature and influence on phase stabilities of Zr addition highly depend on the type of β-stabilizer and its content. Large differences can be observed between Ti-V and Ti-Nb based alloys concerning the influence of Zr content on ωs temperatures. In our case, the Zr addition seems acting as an α'' stabilizer due to the increase of stress induced martensite. Experimental evidences, i.e. recovered SIM rate (Figure 6.14), residual SIM intensity (Figure 6.8) and tensile response (plateau after yielding Figure

6.7), suggest a significant decreasing of CRSS of SIM. Besides chemical phase stability variation as a function of Zr content, it would be of greater significance in accounting the "structural phase stability" here, since the ω_{ath} precipitates are more close to the diffusionless structural defects (linear by partial collapse of adjacent {111}beta planes) than a conventional phase transformation. The physical background of the defect formation is related to the local alloy atoms arrangement (compositional fluctuation in several lattice range), and the corresponding lattice instability. It is agreed that the ωath phase (such linear defects) affects greatly the martensitic phase transformation in an inversed proportionality. Here, mechanisms of Zr influence on Ti-Mo based alloys can be proposed: 1. Zr suppresses ω_{ath} volume fraction by decreasing the ωf temperature; 2. The suppression of quenched-in ω_{ath} (reduction of structural defects) favorites martensitic transformation (reduction in CRSS SIM); 3. Reduction of structural defects may limit the nucleation and growth of mechanical twinning. As a consequence, the evolution of tensile behaviors of Ti-Mo-xZr from x=1% to x=5% can be explained by Zr influence on "structural stability" of beta matrix: 1. The reduction of yielding stress is due to the reduction of quenched-in ω_{ath}, and its effects on twinning and SIM; 2. The presence of plateau on the elastic limit and increase of martensite volume fraction is due to the reduction of CRSS SIM; 3. The reduction of elongation may due to the reduction in mechanical twinning.

Nevertheless, the situation between Ti-12Mo and Ti-12Mo-1Zr is still not clear. The large increase of tensile strength and significant change of deformation behavior (shape of the plastic curve) imply a sudden modification in the nature of the material. Further investigations are being carried out on the comparison of their deformation mechanisms in a narrower range (<1% Zr or replacement in Mo) to fulfill the obvious gap on the mechanical behavior discontinuity, and also in larger content (10% and 15%) to measure the Zr effects in the full alloying range.

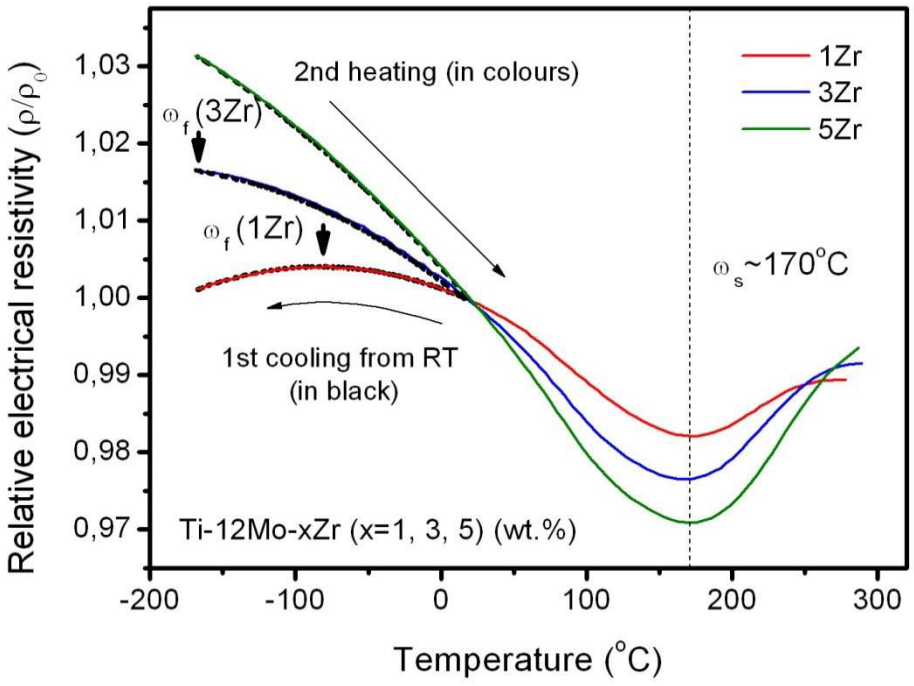

Figure 6.15 The evolution of relative electrical resistivity of Ti-12Mo-xZr materials as a function of temperature. The cooling process (black dash curve) and heating process (color curve) were also presented.

6.3 Conclusion

In this work, the new ternary Ti-Mo based alloys were designed to enlarge the titanium TRIP/TWIP family of alloys to ternary metastable β Ti-alloys by using "d-electron design method". The mechanical behaviors of the investigated alloys were detected and the evolutions of detailed microstructural characterization were analyzed. The following results were obtained.

(1) The evolutions of microstructure during uniform plastic deformation for the investigated alloys are similar. At the onset of plastic deformation, Stress induced β->ω phase transformation was observed. Upon straining, {332}<113> twinning and stress induced martensitic (SIM) β->α" transformation were both identified locally in the deformed β matrix as primary mechanisms. Secondary mechanisms such as 2nd twinning and 2nd SIM α", were then observed in the primary β twins. At the end of the uniform plastic deformation, a complex deformation microstructure was

observed, showing highly disturbed matrix induced by a high volume fraction of twins and occurrence of multiples secondary mechanisms.

(2) The mechanical properties can be improved through adding the third alloying elements into the model Ti-12Mo alloy. The so-designed ternary metastable Ti-Mo based Ti alloys showing combined TRIP and TWIP effects exhibit superior mechanical performances, which indicate the “d-electron design method” can be validated successfully in a ternary metastable β system. Various deformation mechanisms, combining mechanical twinning and phase transformations, lead to the formation of complex deformation microstructure.

References

[1] Abdel-Hady M, Hinoshita K, Morinaga M. Scripta Mater 2006;55:477.
[2] Banerjee D, Williams JC. Acta Mater 2013;61:844.
[3] Hanada S, Izumi O. Metallurgical and Materials Transactions A 1986;17:1409.
[4] Tobe H, Kim HY, Inamura T, Hosoda H, Miyazaki S. Acta Mater 2014;64:345.
[5] Ishiyama S, Hanada S, Izumi O. Isij Int 1991;31:807.
[6] Ohyama H, Nishimura T. Isij Int 1995;35:927.
[7] Zhang JY, Sun F, Hao YL, Gozdecki N, Lebrun E, Vermaut P, Portier R, Gloriant T, Laheurte P, Prima F. Mater Sci Eng A-struct 2013;563:78.
[8] Hao YL, Li SJ, Sun SY, Zheng CY, Yang R. Acta Biomaterialia 2007;3:277.

Conclusions

Based on a combination of “d-electron design method” and an approach aiming at controlling of the electron/atom ratio (e/a)，a binary Ti-12Mo (wt. %) model alloy was designed, induced combined TRIP and TWIP effects. The TEM microstructural analysis shows that the stress-induced phase transformation and mechanical twining occur in the deformed Ti-12Mo alloy samples. In order to further investigate the relation between the β stability and TRIP/TWIP effects, two strategies were applied on the binary model Ti-12Mo alloy. **One is thermal-treatment**, i.e. Low temperature aging with short time (LTA), which is carried out on the binary model Ti-12Mo alloy to control the isothermal ω phase transformation. The objective of this strategy is to manipulate the isothermal ω phase transformation without excessive modification of β matrix chemical composition, keeping the possibility for combined TRIP and TWIP effects to occur. **The other is chemical modification**, i.e. alloying development of ternary compositions by adding third element into the binary model Ti-12Mo alloy, which is proposed to shift the alloying position along the model alloy design route. The objective is to enlarge the titanium TRIP/TWIP family of alloys to ternary metastable β Ti-alloys by using “d-electron design method”. Two sets of ternary alloys were designed. The first one is Ti-9Mo-6W (wt. %) alloy, in which the $\overline{\mathrm{Bo}}$ and $\overline{\mathrm{Md}}$ of this alloy located in the “iso-stability” line. The second one is Ti-12Mo-XZr (X=1, 3, 5) (wt. %) alloys to investigate the influence of the neutral element Zr on mechanical and microstructural behavior.

The so-designed Ti-Mo based alloys display high strength, large plasticity and high work-hardening rate when their as-quenched samples were carried out by tensile tests at room temperature. The deformation mechanisms underlying the

peculiar mechanical behaviors, phase transformation and microstructure evolution were investigated by using several characterized methods, such as conventional X-ray diffraction (XRD), In-situ Synchrotron X-ray diffraction (SXRD), electron backscatter diffraction (EBSD), electrical resistivity measurements (ERM), transmission electron microscopy (TEM) and Automatic crystal orientation measurements (ACOM) TEM. As a consequence, the mechanical performance and microstructure evolution of the binary model Ti-12Mo were in detail presented in chapter 4; the development of ternary Ti-Mo based alloys and the influence of third alloying elements on the mechanical behavior and microstructure were described in chapter 6. Furthermore, a set of short-time LTA treatments were applied at 110°C, 160°C, 260°C and 310 °C for 60 and 600s on the as-quenched Ti-12Mo specimens , respectively. The mechanical and microstructural character subjected to LTA treatments was studied in chapter 5.

Therefore, conclusions can be summarized based on the experimental results and discussions in this thesis.

(1) The so-designed Ti-Mo based alloys at as-quenched state display high strength, large ductility and improved work-hardening rate, and the evolutions of microstructure during plastic deformation are strongly similar. The procedure of uniform plastic deformation can be separated into three stages according to the evolution of the work-hardening rate. At the very beginning of the tensile strain, deformation induced β->ω phase transformation was observed prior to SIM phase transformation and mechanical twinning. Upon straining, primary mechanical twinning and primary SIM α'' precipitation were activated simultaneously in the β matrix as primary mechanisms. Secondary mechanisms such as secondary mechanical twinning and secondary SIM α'' precipitation were then triggered in the twinned β zones. The multiple deformation mechanism combined with {332}<113> twinning and stress induced martensitic (SIM) β->α" transformation simultaneously dominates the whole plastic deformation.

(2) The deformation mechanisms of various modes have been investigated by

applying a set of short-time LTA treatments at 110°C, 160°C, 260°C and 310°C for 60 and 600s, respectively, on a ductile ST Ti-12Mo precursor showing a combined TWIP/TRIP effect. According to the mechanical performances, the LTA specimens are assorted by three groups, 1st: LTA 110°C/60s, LTA 110°C/600s and LTA 160°C/60s; 2nd: LTA 160°C/600s; 3rd: LTA 260°C/60s and LTA 260°C/600s. The deformation modes of the three groups exhibit an evolution as a function of LTA temperatures and durations. 1st group: primary stress-induced ω and α'' precipitations + primary {332}<113> twinning + secondary SIM α'' precipitations and intense {112}<111> twinning in the twinned β zone. 2nd group: stress-induced ω and α'' precipitations + {112}<111> twinning, no secondary mechanisms. 3rd group: few stress-induced ω + deformation slip. The best combination of mechanical properties was achieved at LTA 160°C/60s (1st group), exhibiting a high strength (close to 1200MPa of true stress) and a stable plasticity of ε=0.4 (true strain) with a significant work-hardening effect. Short-time LTA treatments induce insignificant influences on chemical instability of β matrix. The microstructural transitions, i.e. reversible β/ω_{ath} passages and isothermal nano ω/α precipitations, are of great importance on controlling the appearance of deformation products, i.e. stress-induced ω, SIM α'' and mechanical twins. Among them, stress-induced ω precipitation plays a key role in the activation of different deformation modes.

(3) The mechanical properties can be improved through adding the third alloying elements into the model Ti-12Mo alloy. The so-designed ternary metastable Ti-Mo based Ti alloys showing combined TRIP and TWIP effects exhibit superior mechanical performances, which indicate the "d-electron" design method can be validated successfully in a ternary metastable βsystem. Various deformation mechanisms, combining mechanical twinning and phase transformations, lead to the formation of complex deformation microstructure.

Résumé: Dans ce travail, basé sur une approche semi empirique de conception d'alliages de titane à propriétés mécaniques contrôlées, un alliage modèle binaire Ti-12Mo (% massique) et des alliages ternaires sur la base du système Ti-Mo ont été élaborés, combinant des effets TRIP et TWIP lors de la déformation. (TRIP–Transformation Induced Plasticity : plasticité induite par transformation ; TWIP–Twinning Induced Plasticity : plasticité induite par maclage).Les résultats des essais mécaniques montrent que ces alliages présentent une haute résistance mécanique (1000-1200 MPa), une grande plasticité (entre 0,3 et 0,4) et un écrouissage amélioré grâce aux effets simultanés TRIP/TWIP. Différentes techniques de caractérisation telles que la diffraction de rayons X conventionnelle (XRD), la diffraction in-situ sur Synchrotron (SXRD), la diffraction d'électrons rétro-diffusés (EBSD), les mesures de résistivité électrique (ERM), la microscopie électronique en transmission (TEM) et les mesures et traitements automatiques des orientations cristallographiques associées (ACOM/TEM), ont été mis en œuvre pour étudier les mécanismes de déformation, les transformations de phases et l'évolution microstructurale.

Différents mécanismes de déformation, tels que le maclage mécanique {332}<113> et la transformation martensitique induite sous contrainte α″ ont été identifiés à l'issue des essais mécaniques, permettant d'expliquer l'excellente combinaison de propriétés mécaniques obtenue. L'optimisation microstructurale de ces alliages a été conduite à partir de recuits basses températures dans le domaine de précipitation de la phase ω avec pour objectif d'améliorer les propriétés mécaniques afin de contrôler la formation de la phase ω sans modifier de manière excessive la composition chimique de la matrice β, et conserver les effets combinés TRIP/TWIP.

Mots-clés: Métastable β Ti-alliages, les propriétés mécaniques, évolution de la microstructure, les effets TRIP / TWIP

Abstract: In this work, based on combination of the 'd-electron alloy design method' and controlling of electron/atom ratio (e/a), a model of binary Ti-12Mo (wt. %) and ternary Ti-Mo based alloys were designed, induced combined TRIP and TWIP effects (TRIP for Transformation Induced Plasticity and TWIP for Twinning Induced Plasticity). The tensile results show that so-designed alloys exhibit true stress-strain values at uniform plastic deformation, of about 1000-1200MPa and between 0.3 and 0.4 of strain, with a large strain-hardening rate. Several characterization techniques, such as conventional X-ray diffraction (XRD), In-situ Synchrotron X-ray diffraction (SXRD), electron backscatter diffraction (EBSD), electrical resistivity measurements (ERM), transmission electron microscopy (TEM) and automatic crystal orientation measurements (ACOM) TEM, were carried out to to investigate the deformation mechanisms and microstructure evolution sequence. Various deformation mechanisms, i.e. {332}<113> mechanical twinning, deformation induced ω phase and stress-induced α'' martensite, were identified after mechanical testing, resulting in a combination of high strength, large ductility and improved strain-hardening rate. Furthermore, low temperature aging (LTA) treatments were performed on the Ti-12Mo alloy to improve the mechanical property through controlling the ω phase transformation without excessive modification of β matrix chemical composition, keeping the possibility for combined TRIP and TWIP effects to occur. The influence of LTA treatment on the mechanical behavior and microstructural evolution of Ti-12Mo alloy was discussed in detail.

Keywords: Metastable β Ti-alloys, mechanical behavior, microstructural evolution, TRIP/TWIP effects